Aeroacoustic noise prediction of horizontal axis wind turbines

Thomas Schlömicher

Master Thesis

Graz, December 2013

Supervisors:

Andreas Marn
Senior Scientist at the Institute for Thermal Turbomachinery and Machine Dynamics
Graz University of Technology (Austria)

John Cater
Senior Lecturer at the Department of Engineering Science
University of Auckland (New Zealand)

Deutsche Fassung:
Beschluss der Curricula-Kommission für Bachelor-, Master- und Diplomstudien vom 10.11.2008
Genehmigung des Senates am 1.12.2008

EIDESSTATTLICHE ERKLÄRUNG

Ich erkläre an Eides statt, dass ich die vorliegende Arbeit selbstständig verfasst, andere als die angegebenen Quellen/Hilfsmittel nicht benutzt, und die den benutzten Quellen wörtlich und inhaltlich entnommenen Stellen als solche kenntlich gemacht habe.

Graz, am ....
(Unterschrift)

Englische Fassung:

STATUTORY DECLARATION

I declare that I have authored this thesis independently, that I have not used other than the declared sources/resources, and that I have explicitly marked all material which has been quoted either literally or by content from the used sources.

....
date (signature)

Preface This master thesis was written in order to fulfill the requirements of obtaining the degree MSc. at Graz University of Technology. Part of the work was carried out at the department of engineering science at the University of Auckland in New Zealand.

I would like to thank John Cater at the University of Auckland for the invitation to New Zealand and the great supervision during the project. I also would like to thank Rupert Storey and Sahan Wasala from the University of Auckland for their great support during my time in Auckland.

Furthermore I am deeply grateful for the help and the supervision of the present master thesis by my supervisor Andreas Marn from Graz University of Technology. Without his courage and expertise it would not have been possible to write about something as complex as aeroacoustics.

Last but not least I would like to thank my parents for their enormous support during my studies and all my life. It is only because of their unlimited and unconditional love that I made it as far.

Abstract The present thesis deals with the inconvenient side effect of modern energy production out of renewable wind energy. Modern large horizontal axis wind turbines emit broadband aerodynamically caused noise at pronounced levels. This is one of the major hindrances of a widespread employment of wind energy on land today. As a consequence potential geographic sites with okay annual average wind speeds may remain untapped because of their proximity to neighboring houses.

This master thesis deals with the prediction of noise emissions from wind turbines for far field observer positions. Main focus hereby lies on the aeroacoustic noise emissions. Mechanical noise from the gearbox, bearings or the generator are already well understood and have been adequately treated in the past and are not part of this thesis. Two independent noise predicting methods are compared to each other. One method is based on well known semi-empirical aeroacoustic equations. The other method rests upon the Ffowcs-Williams and Hawkings aeroacoustic analogy, which is an exact reformulations of the Navier-Stokes equations in the form of an acoustic wave equation. The results of both methods are plotted against reference measurement data in one-third-octave spectra. The dipole loading terms of this wave equation are approximated by an integral value of the chordwise distributed loading, namely the resulting aerodynamic force. It turned out that this is a valid approximation for highly loaded rotors of large multi-Megawatt wind turbines.

Zusammenfassung Die vorliegende Arbeit beschäftigt sich mit den unbequemen Nebeneffekten moderner Methoden zur erneuerbaren Energiegewinnung mittels Wind Turbinen. Moderne große Windkraftanlagen im Multi-Megawatt Bereich emittieren aerodynamisch verursachten breitbandigen Lärm mit teils beträchtlichen Schalldruckpegeln. Dies ist eines der größten Hindernisse eines weit verbreiteten Einsatzes von Windenergie an Land heutzutage. Als Folge bleiben mögliche Standorte, mit akzeptablen jährlichen durchschnittlichen Windgeschwindigkeiten, aufgrund ihrer Nähe zu Nachbarhäusern, ungenutzt.

Diese Masterarbeit beschäftigt sich mit der Berechnung der Schallemissionen von Windenergieanlagen. Im Focus stehen dabei die aeroakustischen Geräuschemissionen einer Wind Turbine. Mechanische Geräuschemissionen des Getriebes, der Lager oder des Generators sind nicht Teil dieser Masterarbeit. Zwei unterschiedliche Berechnungsmethoden zur Berechnung der aeroakustischen Geräuschemissionen wurden verwendet und miteinander verglichen. Eine Methode basiert auf bekannten semi- empirischen Aeroakustik- Gleichungen. Die andere Methode beruht auf der Ffowcs-Williams and Hawkings aeroakustischen Analogie, welchen ein Umformulierungen der exakten Navier-Stokes Gleichungen in Form einer akustischen Wellengleichung darstellt. Die Ergebnisse beider Methoden inklusive Referenz-Meßdaten sind in Terzspektren aufgetragen. Als Quellterme dieser Wellengleichung dienen Dipol-Kraftterme. Monopol- und Quadrupolterme wurden vernachlässigt. Es stellte sich heraus, dass damit in guter Näherung die Geräuschemissionen von hochbelasteten Rotoren großer Multi-Megawatt Windkraftanlagen abgeschätzten werden können.

Contents

Nomenclature

Roman Symbols

a axial induction factor

a' tangential induction factor

a_{skew} axial induction factor with skew wake

b plate depth

c_0 speed of sound

c_f local frictional coefficient

c chord length

c_p specific isobar heat capacity

c_v specific isochoric heat capacity

d_{TE} trailing edge thickness

e specific internal energy

e_t specific total energy

f frequency

$f_H = 0$ source surface

f_{St} Strouhal vortex shedding frequency

h enthalpy

l_i loading noise terms

$\dot{m}$ mass flow rate

p pressure

p' acoustic pressure

p_0 atmospheric pressure

p_D pressure at rotor disc

p'_L loading acoustic pressure

p'_T thickness acoustic pressure

$\overline{p}$ root mean square pressure

q_∞ dynamic pressure

q_ρ thickness noise terms

r rotor radius

dr element length

r_{in} hub radius

r_{out} tip radius

s specific entropy

t time

τ retarded time

$\boldsymbol{f}$ volumetric force vector

$\boldsymbol{n}$ normal vector

$\boldsymbol{n}_H$ surface normal vector

$\boldsymbol{q}$ heat flux vector

$\boldsymbol{r}_S$ radiation vector

$\boldsymbol{v}$ fluid velocity vector

$\boldsymbol{v}_H$ surface velocity vector

$\boldsymbol{x}$ spatial coordinate

$\boldsymbol{y}$ spatial coordinate (source location)

A_D rotor disc area

A_∞ upwind area

A_W downwind area

B number of blades

C_D drag coefficient

C_{D_i} indicated drag coefficient

C_L lift coefficient

C_P power coefficient

C_T thrust coefficient

C_{D_W} viscous drag coefficient

C_n normal coefficient

C_t tangential coefficient

D drag force

D_W viscous drag force

E human sensation

F_{ADn} normal force component

F_{ADt} tangential force component

F_{loss} tip- and hub loss coefficient

F_T thrust force

H Heaviside function

I_P moment of inertia

I turbulence intensity

L lift force

L_c characteristic length

L_I sound intensity level

L_P angular momentum

L_W sound power level

M Mach number

M_r Mach number in radiation direction

P power

P_W sound power

Q torque

Q_P sound sources

R specific gas constant

Re Reynolds number

dS element surface

S stimulus

S_0 initial stimulus

St Strouhal number

T temperature

U_D axial induced velocity

U_∞ free stream velocity

U_{St} Strouhal characteristic velocity

U_W wake velocity

V_S sound source region

W apparent wind

$\boldsymbol{I}$ sound intensity

$\boldsymbol{M}_S$ Mach number vector of source

$\underline{\boldsymbol{T}}_L$ Lighthill stress tensor

Abbreviations

BEM blade element momentum theory

GDW generalized dynamic wake model

BPF blade passing frequency

$ELLC$ equal loudness level contours

SPL sound pressure level

$TOTAL$ total sound pressure level

$TBLTEp/s$ pressure/suction side turbulent boundary layer trailing edge noise

$TBLTE\alpha$ separation stall noise

$LBLVS$ Laminar boundary layer vortex shedding noise

$TEBVS$ trailing edge bluntness vortex shedding noise

$TIPVF$ tip vortex formation noise

Greek Symbols

α angle of attack

β twist angle

χ rotor wake angle

δ boundary layer thickness

δ^* boundary layer displacement thickness

ε lift to drag ratio

γ rotor yaw angle

κ isentropic coefficient

λ_r local tip speed ratio

μ dynamic viscosity

ν kinematic viscosity

ϕ inflow angle

ψ azimuth angle

ρ fluid density

σ invers specific isobar heat capacity

σ_B blade solidity factor

$\underline{\boldsymbol{\tau}}$ viscous stress tensor

τ_W wall shear stress

$\dot{\vartheta}$ heat source

Γ vortex strength

Λ turbulent length scales

Ω angular velocity of the rotor

Φ velocity potential

Φ_μ vicious dissipation function

Θ directivity angle

Mathematical Symbols

ϵ small value

$\boldsymbol{\nabla}\cdot$ divergence

$\boldsymbol{\nabla}$ gradient

$\triangle$ Laplace operator

$\boldsymbol{\nabla}\times$ rotation

$\underline{\boldsymbol{I}}$ unit matrix

1. Introduction

1.1. General

Exponentially growing energy consumption and increasing skepticism amongst the population concerning nuclear originated power is one driving force for the transition towards other renewable concepts of producing electric energy. The increase of the CO_2 fraction in the Earth's atmosphere over the past decades, and as a consequence a changing climate, is another even more important factor, although the exponential growth of worlds energy demand is challenging enough. Consequently, main energy sources at present are of the character of nuclear fissioning or oxidizing organic material, true alternatives of producing energy are at great need.

In principle wind turbines embody a smart and clean way to generate electricity because no other energy source than the kinetic energy of the wind is needed. The advantages of such a "zero emission power plant" are obvious. There are no green house gas emissions, neither air pollution nor nuclear decay products. No radioactive contaminated material needs to be stored for ten, thirty or thousands of years. Furthermore, life cycle analysis showed that the amount of energy that went into producing a wind turbine is amortized by the turbine within a year of operation. In fact a study of a VESTAS 3MW wind turbine concludes 6.8 months in an off-shore operational environment [5]. Another study showed, that around 120,000 tons of CO_2 are net-avoided by a turbine with a rated electrical power of 3MW during twenty years of operation [10].

The basic operating principal of a wind turbine is to transform kinetic energy of the wind into rotational energy of the wind turbine rotor to be further transformed into electrical energy by a generator. Actually basic concepts of using wind power to drive a machine were used even long before Edison switched on the first light bulb (1.1a) or Volta and Galvani were observing a single spasm of a frogs leg (1.1b).

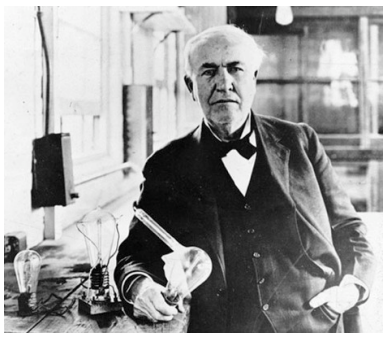

(a)

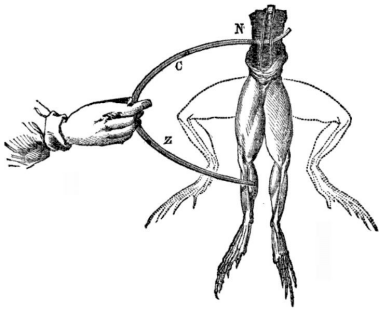

(b)

Figure 1.1.: (a) Thomas A. Edison (1847-1931) and (b) Twitching frog's leg (about 1790)

In fact, the first designs of wind-driven wheels were used in antique times. A wind-powered

organ described by the Greek mathematician and engineer Hero of Alexandria in his *Pneumatica* in the first century AD is believed to be the first recorded wind-driven machine in history [33, 31]. Figure 1.2 shows a sketch of the Hero's wind powered organ.

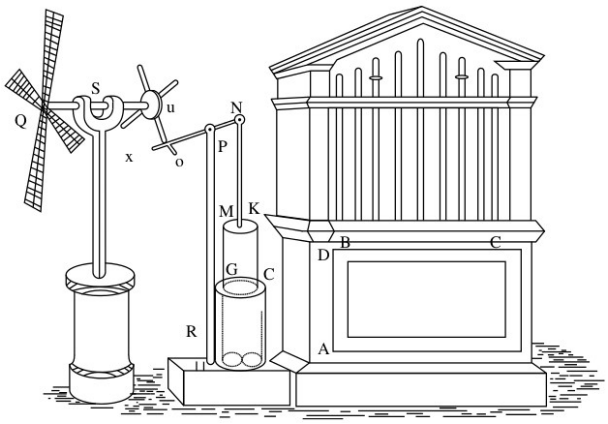

Figure 1.2.: Hero's wind-powered organ [31]

However, it was not until the late 19th and the early 20th century that the Danish engineer Poul la Cour made first attempts to transform wind power into electrical energy in order to store energy in form of pure hydrogen and oxygen by electrolysis. Figure 1.3[1] shows a portrait of Poul la Cour and a picture of his pioneering wind turbine concept.

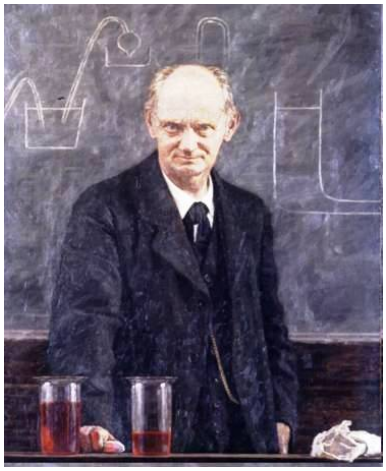

(a) Poul la Cour (1846-1908)

(b) la Cour wind turbine

Figure 1.3.: Poul la Cour. Wind turbine pioneer.

1.2. Motivation

In recent designs a progressive upscaling trend in wind turbine size is evident. A larger wind turbine means a larger swept area of the wind turbine blades, consequently more energy can be extracted from the wind and transformed into electric energy by the rotor. Hence, production costs of electric energy decrease. One drawback is enhanced noise emissions from big multi-Megawatt wind turbines especially in the lower frequency bands.

Figure 1.4[2] depicts the grow in turbine size over the past decades and plans for even larger

[1] Poul la Cour museum, http://www.poullacour.dk/
[2] EWEA (European Wind Energy Association). http://www.ewea.org/

wind turbines are evident as efficiency also increases.

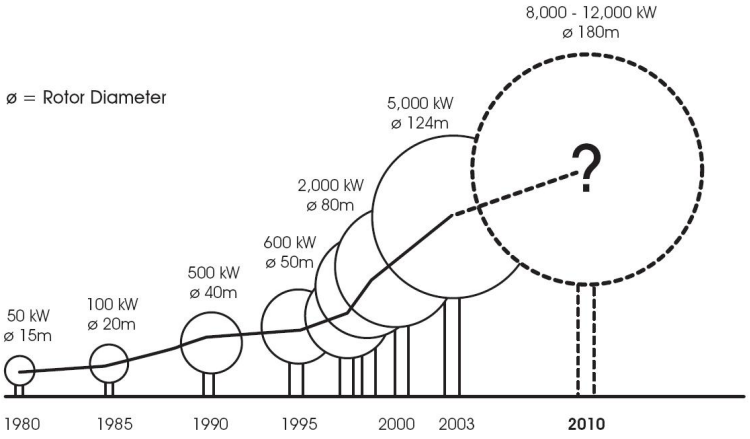

Figure 1.4.: Grow in turbine size over the last decades

The ecological advantages of wind turbines over conventional means of energy production led to a vast growth in the wind energy sector in recent years. As a consequence more and more problems concerning public acceptance of wind turbines arise since wind power plants are not only operated off-shore.

One key factor of an increasing skepticism amongst the population are interfering noise emissions from wind turbines with neighboring houses [39, 38]. In many European countries, therefore, there is a legislative limit of 35dB(A) during night [30].

In addition, it should be mentioned that there are also concerns related to the visual impact on the countryside or negative effects on the local natural wildlife such as bird strike. Further concerns are possible dangers because of detaching ice from the turbine blades.

1.3. Scope

In this thesis the aeroacoustic noise emissions from two different sized wind turbines are analyzed. Two different approaches of aeroacoustic noise prediction are compared to each other.

In the forerun of this project a thorough literature study was done in order to learn more about aeroacoustic noise emissions from wind turbines. Then various available rotor noise prediction tools, based on the Ffowcs-Williams and Hawkings equation, were reviewed. Several candidates could be singled out and a source code from the OpenFOAM project was finally chosen. As a next step the source code of FAST, for semi-empirical noise prediction, and the FWH-code were adopted to each other. Various modifications to both source codes were done by the author. Several data handling subroutines and additional programming loops to account for multiple observer positions (FAST) and for multiple blades (FWH) were implemented. The FAST source code is written in FORTRAN and is compiled and executed in the terminal whereas the original C++ FWH-code was translated into MATLAB. All source codes, used in this thesis, are freely available. The computed acoustic pressure curves of the FWH-code are analyzed with MATLAB. The resulting one-third octave band spectra are compared to the noise output spectra of FAST and measured reference data. All

post processing audio analysis scripts in MATLAB were written by the author.

Section 1.4 gives an overview over the different noise source mechanisms of a wind turbine. Then aerodynamic and acoustic theory is reviewed in Chapter 2. Chapter 3 describes the computer models used. The results of the acoustical analysis are plotted against reference measurement data in one-third octave band plots in Chapter 4. Furthermore, a detailed discussion of the results obtained is given in this Chapter. The final Chapter 5 then sums the most important facts and lists further improvements.

1.4. Wind Turbine Noise

After some ecological reflections on renewable wind energy production and pointing out some historical landmarks in the development towards modern utility sized wind turbines, a brief introduction to the characteristics of wind turbine noise is given in this Section.

Mechanical noise emissions caused by the gearbox, the generator and other auxiliaries play a minor role for modern wind turbines. These noise sources have been reduced to a large extend over the past decades due to improved engineering practices and are not considered in this thesis [27].

The dominant noise source of large modern horizontal axis wind turbines are the rotating blades. The interaction of incoming turbulent wind with the solid blades causes broadband aeroacoustic noise with pronounced low frequency sound pressure levels and gradually decreasing sound pressure levels towards higher frequencies with respect to a non-weighted audio spectrum.

A distinction concerning the noise source mechanisms in relation to the emitted frequencies can be made. Large scale incoming atmospheric eddies that impinge on the turbine blades cause a fluctuating force on the complete blade resulting in low frequency noise. Smaller incoming eddies, in relation to the turbine blade chord length, do not affect the global aerodynamic force and cause higher frequencies.

Another noise source is the interaction of the wind turbine blade's trailing edges with the turbulence that is produced in the blade's own boundary layer. Small turbulent eddies scatter at the trailing edge causing mid to high frequency noise. Small chord lengths or distinct trailing edge bluntness can cause trailing edge vortex shedding at discrete frequencies resulting in tonal noise in the mid to high frequency range. The turbine blades also frequently face high angles of attack causing sizable vortex formation over the complete chord length during high stall conditions resulting in low to mid frequency noise emissions. Furthermore, noise due to tip vortex formation can occur with pronounced frequencies in the mid to higher frequency range but generally low levels.

In addition noise can be caused due to an interaction of the tower with the blade. This is generally of little importance for wind turbines with an upwind configuration, when the rotor is facing against the wind direction, but can add significant sound levels to the frequency spectrum for downwind rotors.

Figure 1.5.: Wind turbine noise source distribution in the rotor plane of a GE 2.3MW prototype test turbine. Rotor diameter 94m, tower height 100m. [27, 28]

Noise source localization measurements on a 2.3MW and a 850kW horizontal axis wind turbine with an 148-microphone acoustic array done by Oerlemans [27] revealed, that the main noise source of a modern large wind turbine is the highly loaded outer part of the blade, but not the very tip. Figure 1.5 shows the noise source distribution in the rotor plane for a 2.3MW prototype wind turbine averaged over several revolutions. It can be seen that most noise originates from the outer part of the turbine blades. Furthermore, these array assessments unveiled that the noise sources in the rotor plane are asymmetrically distributed although the blades emit a constant sound pressure level throughout a complete revolution. The descending blade is perceived louder by an observer on the ground than the ascending blade. This is referred to as *swishing noise*. During one revolution of a three bladed wind turbine three distinct swish events can be sensed. The total asymmetry in Figure 1.5 between high levels, indicated as read areas, and low levels is 12dB. The highest swish emission levels occur around the 3 o'clock position of the blade for an observer directly in front of the wind turbine.

The swish feature of wind turbine noise can be explained with the directivity characteristic of aerodynamically caused noise of an airfoil (maximum radiation occurs in direction of the leading edge) and convective amplification effects (the amplitude of the perceived sound increases when a noise source moves towards an observer). Thus, for an observer on the ground the blade moving downward is perceived louder than the one moving upward (maximum radiation into the sky) [27, 28].

Additional noise measurements by Oerlemans [27] with eight single microphones, equally

distributed on a 240m circle around the wind turbine showed, that the average noise levels for observer positions close to, or in, the rotor plane are lower than the average levels for upwind or downwind observer positions. This feature is referred to as the *directivity characteristic of wind turbine noise*. Figure 1.6 shows the averaged measured noise levels of every microphone position against predicted levels.[3] The migration of the data dots in Figure 1.6 is due to misalignment angles because of turbine yaw maneuvers during the measurement recording period.

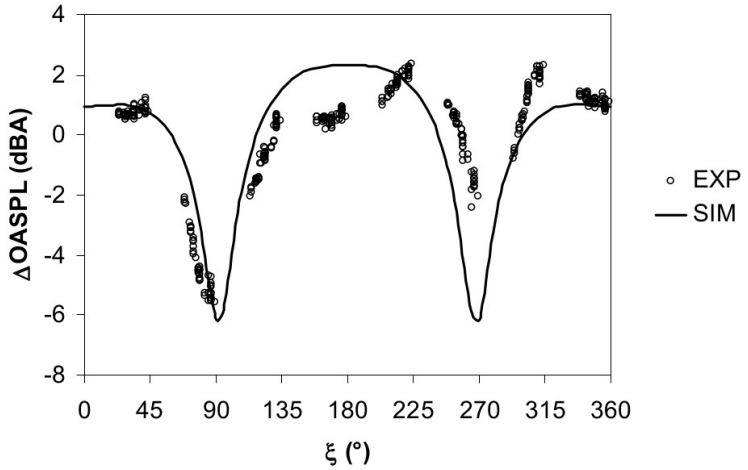

Figure 1.6.: Measured and predicted wind turbine noise directivity [27]

Furthermore the assessments of Oerlemans [27] showed that around the wind turbine the swish amplitude is not constant. Interestingly, the highest swish amplitudes occur in the rotor plane at reduced average levels (compare with Figure 1.6). Figure 1.7 shows the experimental swish amplitudes together with predicted values.

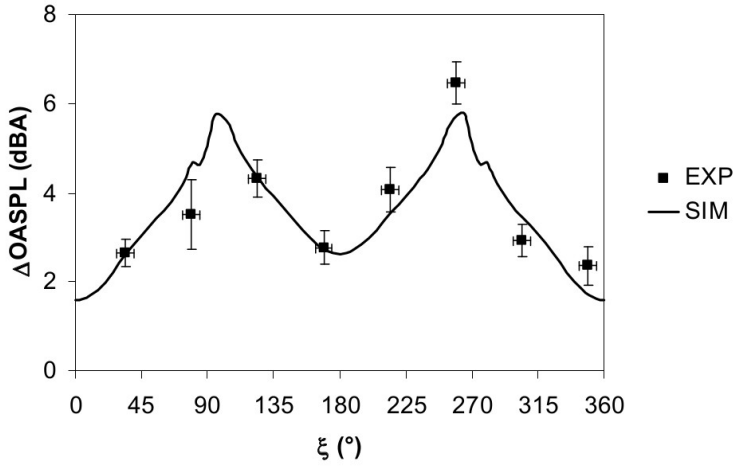

Figure 1.7.: Measured and predicted swish amplitude [27]

[3]The differential overall sound pressure level (△OASPL) in Figure 1.6 is the integrated A-weighted audio spectrum between 250 and 800Hz normalized by the average level of the eight microphones [27].

2. Theory

This Chapter provides an overview of the underlaying physical processes of aeroacoustic noise from wind turbines. The theory part of this master thesis comprises fluid dynamic and acoustic fundamentals in Sections 2.1 and 2.3.

2.1. Fluid Dynamic Essentials

As mentioned in the introduction wind turbines emit broadband aerodynamically caused noise. The interaction of the solid blades with the fluid is the driving force of aeroacoustic noise emissions from a wind turbine. The development of a turbulent boundary layer as well as the impingement of incoming atmospheric turbulence lead to pressure fluctuations on the blade surface which are propagated as acoustic waves into the field. These acoustic pressure waves are sensed by an observer on the ground. This Section gives a brief overview of the governing aerodynamic principles of a solid body in a flow field.

2.1.1. Governing equations

The governing equations of fluid motion are the *Navier- Stokes equations* for conservation of mass (2.1), momentum (2.2) and energy (2.3).

$$\frac{\partial \rho}{\partial t} + \boldsymbol{\nabla} \cdot (\rho \boldsymbol{v}) = 0 \tag{2.1}$$

$$\frac{\partial \rho \boldsymbol{v}}{\partial t} + \boldsymbol{\nabla} \cdot (\rho \boldsymbol{v}\boldsymbol{v}) = -\boldsymbol{\nabla} p + \boldsymbol{\nabla} \cdot \underline{\boldsymbol{\tau}} + \boldsymbol{f} \tag{2.2}$$

$$\frac{\partial \rho}{\partial t} + \boldsymbol{\nabla} \cdot (\rho e_t \boldsymbol{v}) = -\boldsymbol{\nabla} \cdot (p\boldsymbol{v}) - \boldsymbol{\nabla} \cdot \boldsymbol{q} + \boldsymbol{\nabla} \cdot (\underline{\boldsymbol{\tau}} \cdot \boldsymbol{v}) + \dot{\vartheta} + \boldsymbol{f} \cdot \boldsymbol{v} \tag{2.3}$$

ρ is the fluid density, $\boldsymbol{v}$ the velocity vector and p the pressure. $\underline{\boldsymbol{\tau}}$ is the stress tensor due to viscous friction in the fluid, see A.1. $\boldsymbol{f}$ is a volumetric force term. e_t is the specific total energy composed of the specific internal energy and the specific kinetic energy , $e_t = e + 1/2\,|\boldsymbol{v}|^2$. $\boldsymbol{q}$ is the heat flux vector. $\dot{\vartheta}$ denotes the heat sources.

2.1.2. Flow at high Reynolds numbers

Euler flow The flow around a wind turbine blade can be treated as inviscid ($Re \gg 1$) and incompressible ($M \leq 0.2$).[1] Both assumptions lead to more simplified formulations of the conservation of mass and momentum.

[1] $Re = \frac{uc}{\nu}$ is the Reynolds number and is large for considered flows around a turbine blade. $M = \frac{u}{c_0}$ is the Mach number and is rather low.

$$\boldsymbol{\nabla} \cdot \boldsymbol{v} = 0 \tag{2.4}$$

$$\frac{\partial \boldsymbol{v}}{\partial t} + \boldsymbol{v} \cdot \boldsymbol{\nabla} \boldsymbol{v} = -\frac{1}{\rho} \boldsymbol{\nabla} p + \boldsymbol{f} \tag{2.5}$$

Potential flow Rotation of a fluid is first an foremost a purely kinematic notion, but has pronounced physical energetic importance [36]. Discontinuous velocity changes or viscous forces exerted within a fluid affect the rotation of a fluid.

In a *potential flow* the fluid is free of rotation. A solution to the Euler flow equation can be found by dealing with the velocity potential Φ. The velocity field is the gradient of the velocity potential.

$$\boldsymbol{v} = \boldsymbol{\nabla} \Phi \tag{2.6}$$

Inserting equation 2.6 into the definition of rotation $\boldsymbol{\omega} = \frac{1}{2} \boldsymbol{\nabla} \times \boldsymbol{v}$ gives

$$\boldsymbol{\omega} = \frac{1}{2} \boldsymbol{\nabla} \times (\boldsymbol{\nabla} \Phi) \equiv 0 \tag{2.7}$$

Demanding that the fluid should be incompressible

$$\boldsymbol{\nabla} \cdot \boldsymbol{v} = 0 \tag{2.8}$$

yields the Laplacian equation for the velocity potential

$$\boldsymbol{\nabla} \cdot \boldsymbol{\nabla} \Phi = 0$$

$$\triangle \Phi = 0 \tag{2.9}$$

If the potential Φ is know then one can find the velocity field $\boldsymbol{v}$ according to 2.6.

2.1.3. Boundary layer theory

For flows at high Reynolds numbers the inertial forces outnumber the viscous forces by a large degree. This is because of very little velocity gradients within the fluid so the stress tensor , w.r.t Newton's viscous law, plays a minor role. Looking at the conditions near a wall however puts the spotlight back on the viscous stresses. A very thin layer develops between the wall and the free stream with a velocity gradient from the free stream velocity to zero. This transitional layer is called the *velocity boundary layer*. The thickness of this layer is assumed to be very small against the characteristic length one is looking at $\delta(x) \ll L_c$. In aerodynamic investigations often the chord length c is chosen as the the characteristic length.

Therefore, a detached analysis of the the outer region, with dominant inertial effects, where the laws of potential flow apply, on the one hand, and the boundary layer region, with enhanced viscous stresses, is desired.

Prandtl first made a clear distinction between these two flow regions near a wall. By dimensional analysis of the momentum equation he singled out the major contributer to

viscous stresses in the boundary layer and identified the velocity gradient in the y-direction of the momentum equation in the x-direction. The momentum equation in the y-direction does not play any role in the boundary layer and one can conclude that the pressure gradient in the the y-direction is almost zero, hence the pressure in the boundary layer is imposed by the external flow. Equations 2.10, 2.11 and 2.12 are the results of this dimensional analysis, the *boundary layer equations* [34].

Prandtl boundary layer equations

$$\frac{\partial u}{\partial x} + \frac{\partial v}{\partial y} = 0 \tag{2.10}$$

$$\frac{\partial u}{\partial t} + u\frac{\partial u}{\partial x} + v\frac{\partial u}{\partial y} = -\frac{1}{\rho}\frac{dp}{dx} + \nu\frac{\partial^2 u}{\partial y^2} \tag{2.11}$$

$$\frac{dp}{dy} = 0 \tag{2.12}$$

Laminar boundary layer Blasius 1908 developed a solution to this equations, describing a growing laminar boundary layer along a flat plate with a sharp leading edge, see Figure 2.1. This case should demonstrate a generic concept of similarity boundary layer solutions for arbitrary curved solid bodies in a flow field, such as the *Falkner-Skan-equation* [34].[2] The characteristic length of a flat plate is assumed to be L_c.

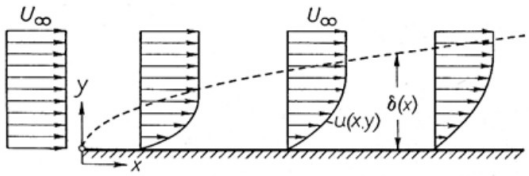

Figure 2.1.: Velocity boundary layer [14]

Blasius found that the laminar boundary layer grows indirect proportional to the square root of the local Reynolds number $Re_x = \frac{U_\infty x}{\nu}$. For convenience the boundary layer thickness is defined as the distance from the wall where the velocity inside the boundary layer reaches 99% of the free stream velocity U_∞.

$$\frac{\delta_{99}(x)}{x} \cong \frac{5}{\sqrt{Re_x}} \tag{2.13}$$

Because of the imprecise term "99%-boundary layer" another important property of a boundary layer is the displacement thickness δ^*. It describes to what extend the streamlines in the exterior (potential) flow field are being displaced.[3]

$$\delta^*(x) = \int_{y=0}^{\infty} \left(1 - \frac{u}{U_\infty}\right) dy \tag{2.14}$$

$$\frac{\delta^*(x)}{x} = \frac{1.721}{\sqrt{Re_x}} \tag{2.15}$$

[2] The flat plate solution of Blasius is just a special case of the Falkner-Skan-equation [34].
[3] The displacement thickness is typically $1/8$ to $1/5$ of δ_{99}.

The solution of Blasius also allows for some statements on the viscous drag. The local frictional coefficient is

$$c_f = \frac{\tau_W(x)}{\frac{\rho}{2}U_\infty^2} = \frac{0.664}{\sqrt{Re_x}} \tag{2.16}$$

with the viscous stress distribution along the wall

$$\tau_W(x) = \mu \left(\frac{\partial u}{\partial y}\right)_W \tag{2.17}$$

The overall viscous drag force D_W for a flat plate (top and bottom side) with the length L_c and the depth b therefore is

$$D_W = 2\int_0^{L_c} \tau_W(x)\, b dx \tag{2.18}$$

According to that the viscous drag coefficient is

$$C_{D_W} = \frac{D_W}{\frac{\rho}{2}U_\infty^2 \cdot 2bL_c} = \frac{1.328}{\sqrt{Re_{L_c}}} \tag{2.19}$$

This result is of some importance because potential flow theory is not capable of describing a drag force on a solid body in a flow. In fact for a planar flow around an airfoil potential flow theory can only deliver a lift force perpendicular to the relative incident velocity but no drag component (*d'Alembert's paradox*) although drag is sufficiently ascertained from experiments [36]. To mathematically account for drag of a solid body in a flow one has to take viscous effects near the wall into account.

Boundary layer separation A decelerated external flow causes a positive pressure gradient within the boundary layer $\frac{dp}{dx} > 0$. This pressure increase makes the fluid particles close to the wall, with decreased kinetic energy, to diverge from the wall. Reverse flow occurs and the boundary layer separates. The velocity profile of a separating boundary layer in Figure 2.2 shows an inflection point and the velocity gradient at the wall becomes zero or changes sign.

$$\left(\frac{du}{dy}\right)_W \leq 0 \tag{2.20}$$

Consequently, the separation point is indicated by zero wall shear stresses.

$$\tau_W = \mu \left(\frac{\partial u}{\partial y}\right)_W = 0 \tag{2.21}$$

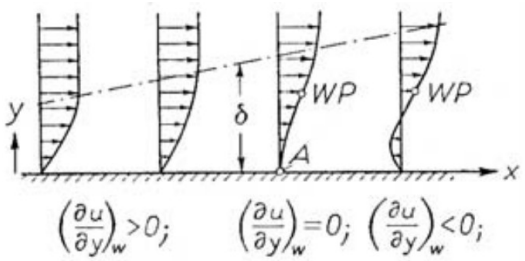

Figure 2.2.: Boundary layer separation [14]

Turbulent boundary layer For sufficient high Reynolds numbers the laminar boundary layer transition towards a more turbulent stochastic flow characteristic. The location where the boundary layer transitions from laminar to turbulent is indicated by a critical Reynolds number $Re_{krit}(x) = \left(\frac{ux}{\nu}\right)_{x_{krit}}$. However, for Reynolds numbers $Re > 50 \cdot 10^6$ the boundary layer is fully turbulent from the beginning [36, 14]. The thickness of the turbulent boundary layer is larger than the one of the laminar boundary layer, as sketched in Figure 2.3.

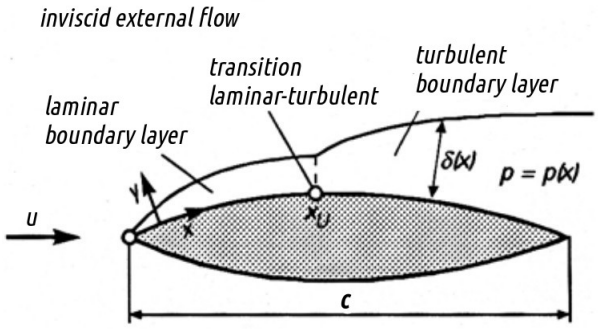

Figure 2.3.: Laminar-turbulent boundary layer along an airfoil [14]

2.1.4. Airfoil theory

Placing an object in a flow demands some force to hold it in place. Section 2.1.3 describes what causes a force component (*drag force*) in the direction of the incident flow. This Section describes what causes a force component perpendicular to it. This force is called the *lift force*.

Infinite wing The presence of a solid body in the flow forces the oncoming fluid particles to divert. The curvature of the particle trajectories results in a pressure difference on either side of the airfoil. The low pressure side is called *suction side* and the side with increased pressure is called *pressure side*.

The difference in flow speed between the suction side, where the fluid particles move faster, and the pressure side, with a decelerated flow, causes a circulation around the body. The line integral of curve K, which section after section runs along and perpendicular to the streamlines, over the velocity in the flow field is nonzero, see Figure 2.4.

$$\Gamma = \oint_K \boldsymbol{v} ds_K > 0 \tag{2.22}$$

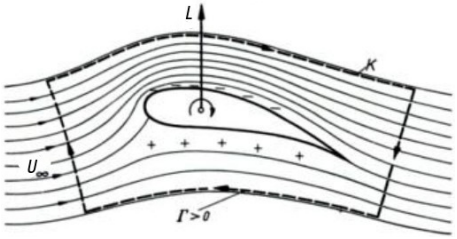

Figure 2.4.: Clockwise circulation round an airfoil [37]

This circulation is responsible for the lift (*Kutta-Joukowsky theorem*).

$$L = \rho \cdot \Gamma \cdot U_\infty \tag{2.23}$$

As a reaction to a circulation in box A-B-C-F in Figure 2.5 a co-rotating circulation has to constitute in box F-C-D-E. The circulation in box A-B-C-F is called the *bound vortex* and the co-rotating circulation in box F-C-D-E is called the *starting vortex*.

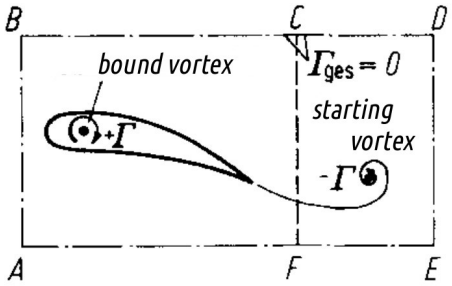

Figure 2.5.: Bound vortex and starting vortex of an airfoil [36]

The Lift and drag force represent an integral value of the total pressure and shear stress distribution around the airfoil. They sum up to a resultant force acting on the airfoil. An exemplary pressure distribution and the resulting lift and drag forces are illustrated in Figure 2.6. The lift and drag can be written as

$$L = C_L q_\infty A \tag{2.24}$$

$$D = C_D q_\infty A \tag{2.25}$$

$q_\infty = \frac{\rho}{2} U_\infty^2$ is the *dynamic pressure* and A a reference area. C_L and C_D are the lift and drag coefficients, respectively. For a long body, such as an aircraft wing or a wind turbine blade, the lift and drag per unit span is used and the reference plane is replaced by the chord length c.

$$L = C_L \frac{\rho}{2} U_\infty^2 c \tag{2.26}$$

$$D = C_D \frac{\rho}{2} U_\infty^2 c \tag{2.27}$$

The *lift to drag ratio* defines the overall performance of an airfoil profile. Obviously this function can be optimized.

$$\varepsilon = \frac{C_D}{C_L} \tag{2.28}$$

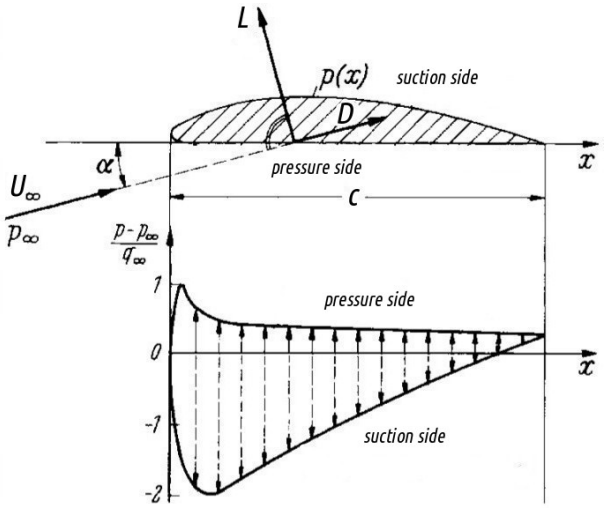

Figure 2.6.: Aerodynamic forces and pressure distribution on an airfoil under incident angle [36]

The lift and drag coefficients are dependent on the angle of attack α. This is the angle between a reference line of the airfoil (chord line) and the velocity vector of the oncoming flow. If the body is moving relative to the oncoming flow (or vice versa) then the relative or the apparent wind vector has to be considered. Figure 2.7a shows the dependency of C_L and C_D on α. For mild angle of attack the dependency of the lift is almost linear and nonlinear for the drag. For higher angle of attack the lift drops radically due to flow separation on the suction side of the airfoil. The airfoil *stall*s. Additionally the drag increases rapidly in the stalled region.

C_L and C_D are measured in wind tunnels or computed and plotted in so called *polars* or *polar plots*. Figure 2.7b shows such a polar plot which combines lift, drag and angle of attack in one curve. C_{D_i} is called the *indicated drag coefficient*.

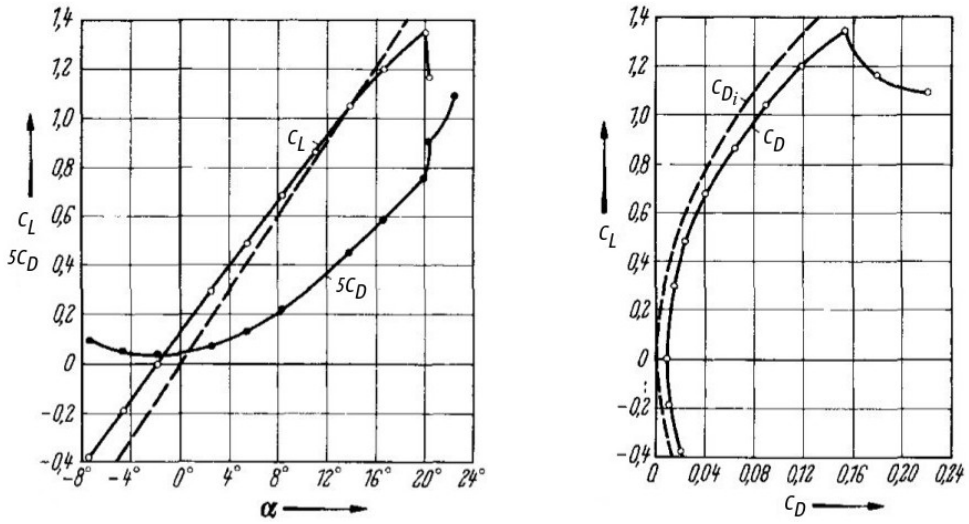

(a) Dependency of the lift and drag coefficient on the angle of attack

(b) Polar plot C_L (C_D)

Figure 2.7.: Lift and drag coefficient of a NACA 2412 airfoil [36]

Wing of finite length The lift distribution per unit span decreases to zero towards the ends and can be represented as a distribution of bound vortices $\Gamma(y)$, see Figure 2.9a. Furthermore, the pressure difference on either side of the wing causes a flow around the blade tips. The ends can be treated as a leakage in the span area. This induces a spanwise flow (*secondary flow*) on the wing surface, as demonstrated in Figure 2.8.

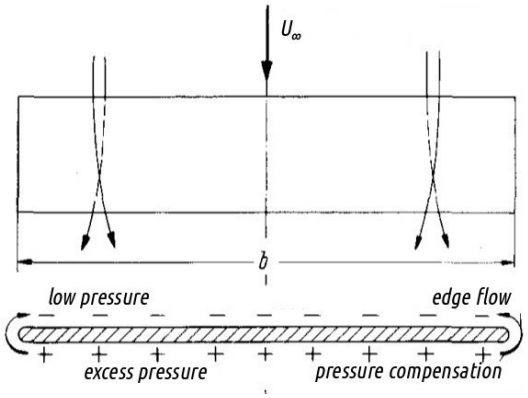

Figure 2.8.: Mechanism of vortex sheet formation [36]

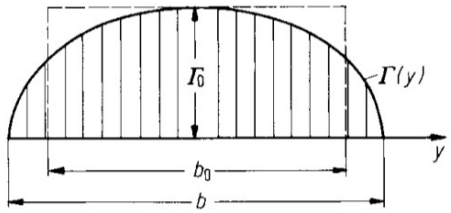

(a) Spanwise distribution of circulation

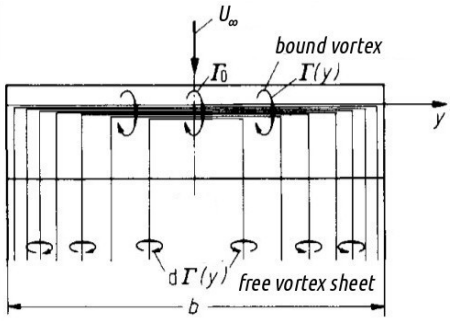

(b) Free vortex sheet

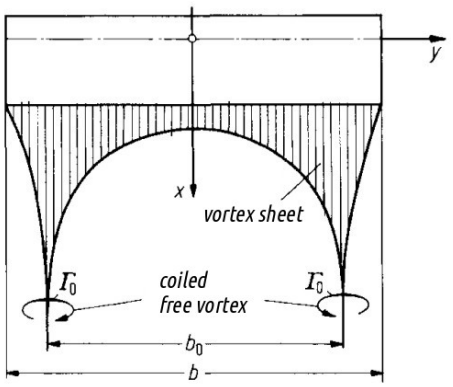

(c) Coiled free vortex

Figure 2.9.: Free vortex formation [36]

The flow on the pressure side of the wing is deflected outwards and the flow on the suction side is deflected inwards. As a consequence, the flow at every blade section curls up forming a free trailing vortex sheet behind the wing, as in Figure 2.9b. This vortex sheet, consisting of vortices of the strength $d\Gamma(y)$, rolls up to two co-rotating coiled free vortices Γ_0 in some distance from the trailing edge, as shown in Figure 2.9c.

After a finite time span the bound, free and starting vortices form a closed vortex system as in Figure 2.10. This vortex system then extends to infinity after infinite time.

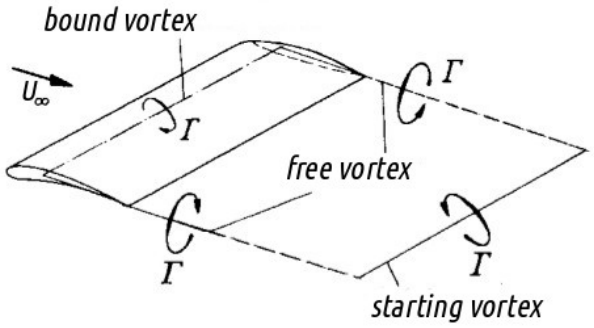

Figure 2.10.: Vortex system behind a wing of finite length [36]

2.2. Wind Turbine Aerodynamics

After having quickly reviewed basic fluid dynamics this Section continues with aerodynamic aspects of a wind turbine. First the concept of an actuated disc is introduced in Section 2.2.1. Based on that, expressions for the extraction of thrust and torque in the rotor disc are derived in Sections 2.2.2 and 2.2.3.

2.2.1. Actuator disc model

In the rotor plane of a wind turbine kinetic energy gets extracted from the wind. A *streamtube* that passes through a turbine model can be defined with a smaller upwind cross Section and a wider downwind one, w.r.t. mass continuity. Figure 2.11 shows the streamtube of a wind turbine. It is assumed that there is no flow across the boundary surface of this streamtube and the mass flow rate within the streamtube remains constant.

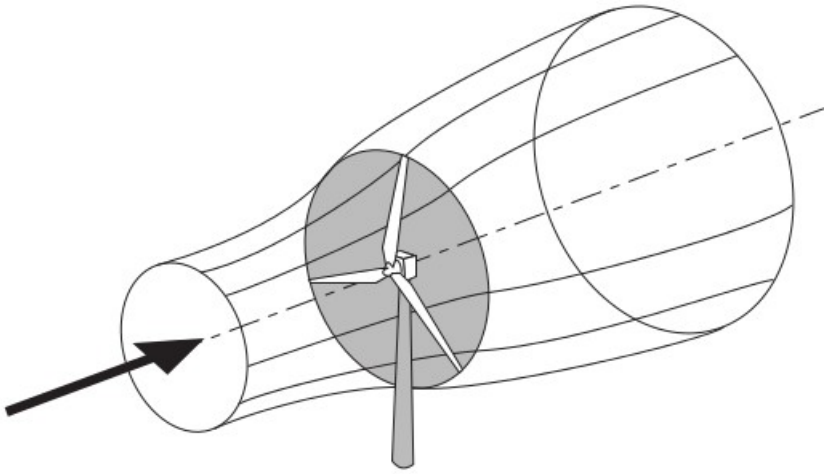

Figure 2.11.: Streamtube of a wind turbine [8]

The turbine blades sweep out a circular area in the rotor plane which is referred to as an *actuator disc*. It acts as a simple permeable drag device which slows down the wind from a far upwind free stream velocity U_∞ to an induced velocity U_D in the rotor plane with a corresponding pressure increase towards the actuator disc. The pressure drops in a step like manner in the rotor plane from p_D^+ just upstream to p_D^- just downstream of the actuator disc. Afterwards the velocity further decreases to U_W, as the pressure has to reach the atmospheric level again. Figure 2.12 depicts this situation.

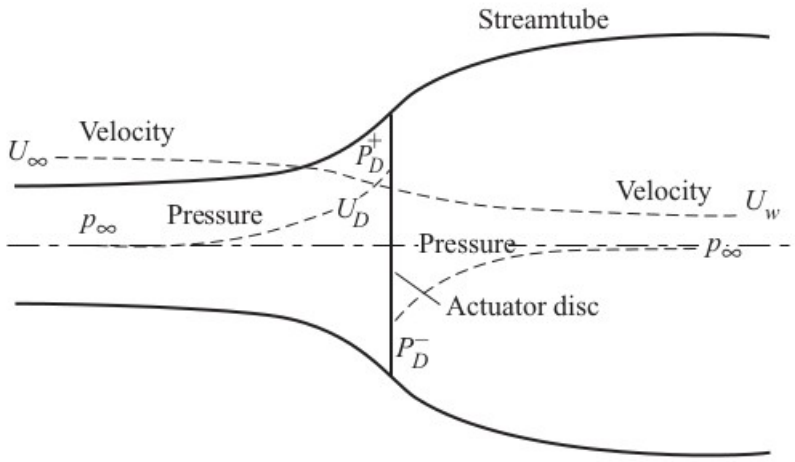

Figure 2.12.: An energy extracting actuator disc [8]

2.2.2. Momentum theory

The forcing responsible for the loss of momentum is the *thrust force*. It can be represented by the pressure difference just upstream and downstream of the actuator disc or by the decelerated mass flow along the streamtube.

$$F_T = \left(p_D^+ - p_D^-\right) A_D = \underbrace{\left(U_\infty - U_W\right) \dot{m}}_{\substack{Rate\,of\,change \\ of\,momentum}} \tag{2.29}$$

The mass flow rate in the streamtube is of course

$$\dot{m} = \rho A_\infty U_\infty = \rho A_D U_D = \rho A_W U_W = const \tag{2.30}$$

Applying Bernoulli's equation, both to the upwind and the downwind side of the actuated disc, the pressure drop then reads

$$\left(p_D^+ - p_D^-\right) = \frac{1}{2}\rho \left(U_\infty^2 - U_W^2\right) \tag{2.31}$$

The velocity in the rotor plane diminishes by $-aU_\infty$ where a is called the *axial induction factor* which can be understood as a percentage of how much the free stream velocity is reduced when approaching the actuator disc location. U_D therefore reads as

$$U_D = U_\infty \left(1 - a\right) \tag{2.32}$$

Inserting equation 2.31 in equation 2.29 w.r.t 2.30 and 2.32 yields

$$U_W = U_\infty \left(1 - 2a\right) \tag{2.33}$$

and consequently

$$F_T = 2\rho A_D U_\infty^2 a \left(1 - a\right) \tag{2.34}$$

The power that gets extracted from the wind in the rotor plane of a wind turbine follows as

$$P = F_T U_D = 2\rho A_D U_\infty^3 a\,(1-a)^2 \tag{2.35}$$

Power coefficient and *Lanchester-Betz limit* The *power coefficient* compares P in equation 2.36 with the situation as if there is no energy extracting disc present. The denominator in equation 2.36 thus is the total amount of kinetic energy in an A_D cross sectional flow.

$$C_P = \frac{P}{\frac{1}{2}\rho A_D U_\infty^3} = 4a\,(1-a)^2 \tag{2.36}$$

A maximum of this value ($^{dC_P}/_{da} = 0$) occurs for an induction factor of $a = {}^1/_3$ which gives an power coefficient of $C_P = \frac{16}{27} = 0.593$. That means maximal 60% of the kinetic energy of a mass flow entering the streamtube can be extracted by the actuator disc. Consequently, in order to (theoretically) achieve a maximum power output of a wind turbine, its aerodynamic design needs to yield induced velocities of $U_D = {}^2/_3 U_\infty$ in the rotor plane and $U_W = {}^1/_3 U_\infty$ in the far wake field. This relation is know as the *Lanchester-Betz limit* [8].

In fact modern large wind turbines can reach values of about $C_P \approx 0.5$.

Thrust coefficient and the *turbulent wake state* In the same way a *thrust coefficient* can be defined

$$C_T = \frac{F_T}{\frac{1}{2}\rho A_D U_\infty^2} \tag{2.37}$$

$$C_T = 4a\,(1-a) \tag{2.38}$$

For $C_T \geq 1$, which means $a \geq \frac{1}{2}$, $U_W = U_\infty\,(1-2a)$ becomes zero or even negative which is physically not the case. There is no flow backwards in the wake field, as the classic one dimensional momentum formulation would indicate. The flow indeed is highly decelerated but still positive. This condition is called the *turbulent wake state* and it occurs for turbines operating at high tip speed ratios[4] (e.g. constant (rotational) speed wind turbines at low wind speeds). Figure 2.13 illustrates the transition into the turbulent wake state of a wind turbine by means of an increased rotational speed of the turbine since the free stream velocity is drawn constant.

According to equations 2.29 and 2.37, the thrust coefficient increases with an increased difference of the free stream velocity U_∞ to the wake velocity U_W. With a big enough velocity jump from the wake velocity U_W to the free stream velocity U_∞ the shear layer, which separates the wake field form the outer flow, becomes unstable and eddies form at the boundary surface of the streamtube. These eddies swirl across the boundary surface and more flow is entrained from outside the wake and the turbulence in the wake field increases as outlined in Figure 2.14. Actually the transition to the turbulent wake state happens for values of $a > 0.4$.

[4] The *tip speed ratio* λ is the ratio between the blade tip's rotational speed and the free stream velocity U_∞, hence $\lambda = \frac{r\Omega}{U_\infty}$.

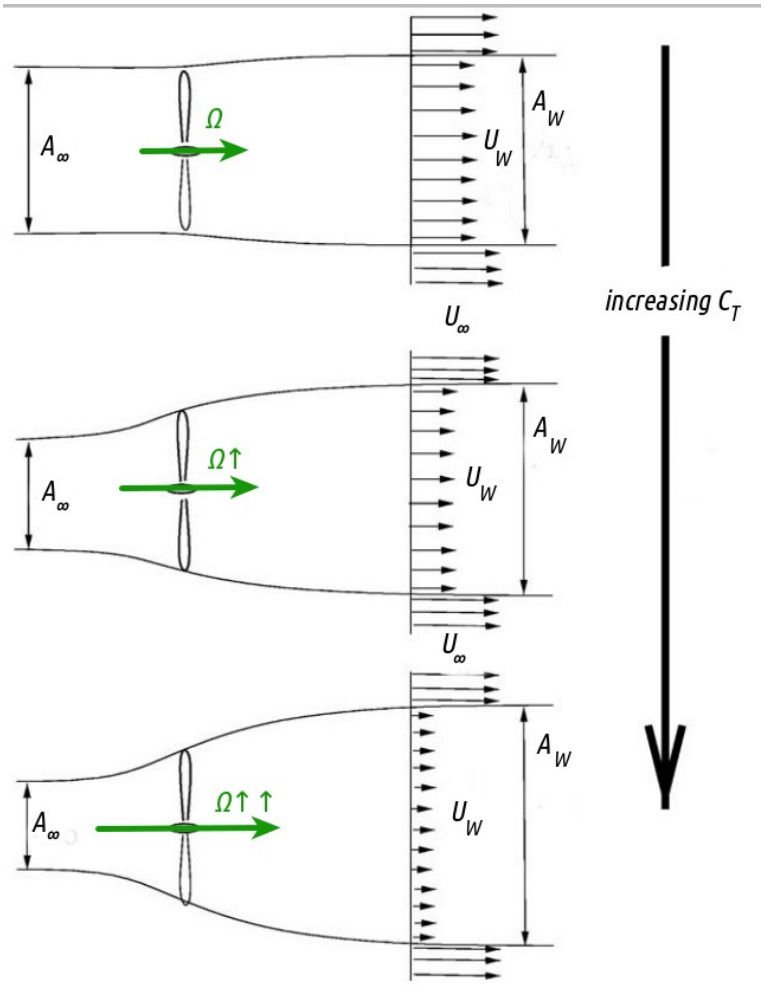

Figure 2.13.: Wake for increasing C_T [16]

Highly decelerated flow in the wake field for values of $a \geq 0.5$ is not represented by the classic one dimensional momentum theory. Therefore empirical relations can be used to adjust for induction factors under turbulent wake state conditions as will be seen in Section 3.3.1.

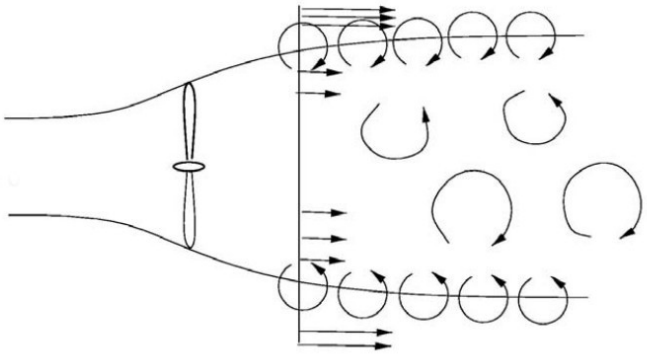

Figure 2.14.: Turbulent wake state [16]

The concept of extracting energy in equation 2.35 is not sufficient. Not only because it demands translational displacement over impractically large distances of the actuated disk, but also because the thrust force diminishes when the disk is moving with the flow. Therefore one let the actuator disk rotate.

That is what happens with wind turbines. By virtue of their aerodynamic design the flow

over the turbine blades induces tangential forcing and the resulting rotational power can, for instance, propel an electrical generator in the rotor hub.

The tangential forcing exerted on the rotor disc, however, requires an equal and opposite forcing on the fluid. This causes the air after the rotor disc to rotate in the opposite direction than the rotor. Before entering the actuator disc the flow has no rotational motion at all, see Figure 2.16b.

There is no sudden but gradual gain in tangential motion of the fluid. The tangential velocities in the middle and immediately downstream of the disc are $r\Omega a'$ and $2r\Omega a'$ respectively [8]. a' is the *tangential induction factor* and it expresses the change in tangential velocity across the actuator disc. Ω is the angular velocity of the rotor. Figure 2.15 shows how the flow accelerates in the tangential direction.

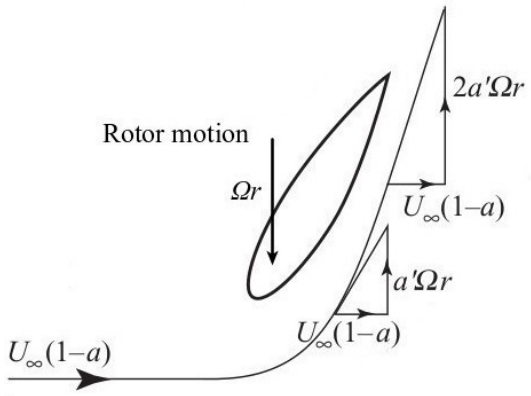

Figure 2.15.: Tangential velocity grows across the disc thickness [8]

The tangential as well as the axial induced velocity are not constant for all radial positions. Therefore, to allow for variations of both induced velocity components, the rotor disc is divided into annular rings with an annular area $dA_D = 2\pi r dr$, see Figure 2.16a. Hence, the streamtube from Figure 2.11 is also divided into annular streamtubes, distributed in the radial direction r with an radial width dr. Figure 2.16b shows an annular streamtube with an annulus cross section of the rotor disc in the rotor plane as in Figure 2.16a.

The torque that gets extracted from the fluid in the rotor plane from every annular ring can be calculated as follows [19]. Assume that the mass of an annular section, which experiences annular acceleration, is dm. Thus, the moment of inertia I_P and the angular momentum L_P of this mass element rotating with $\omega = const$ is

$$dI_P = dmr^2 \tag{2.39}$$

$$dL_P = dI_P\omega \tag{2.40}$$

The torque follows with

$$dQ = d\dot{L_P} = d\dot{m}\omega r^2 + \underbrace{dmr^2\dot{\omega}}_{=0} \tag{2.41}$$

With $d\dot{m} = \rho U_D dA_D$ and the tangential velocity after the actuator disc ($r\omega = 2r\Omega a'$) plus the axial induced velocity from equation 2.32 the torque that gets extracted from the fluid for each annular ring is

$$dQ = 2r^2 \rho U_\infty \Omega (1-a) a' dA_D \tag{2.42}$$

Accordingly, each annular ring extracts an incremental thrust force such that equation 2.34 becomes

$$dF_T = 2\rho U_\infty^2 (1-a)\, a dA_D \tag{2.43}$$

Equations 2.42 and 2.43 constitute the momentum part of the blade element momentum method from Section 3.3.1, which is implemented in the software FAST to calculate the aerodynamic loading on the blades. This loading or rather the fluctuating components of it is a source of sound.

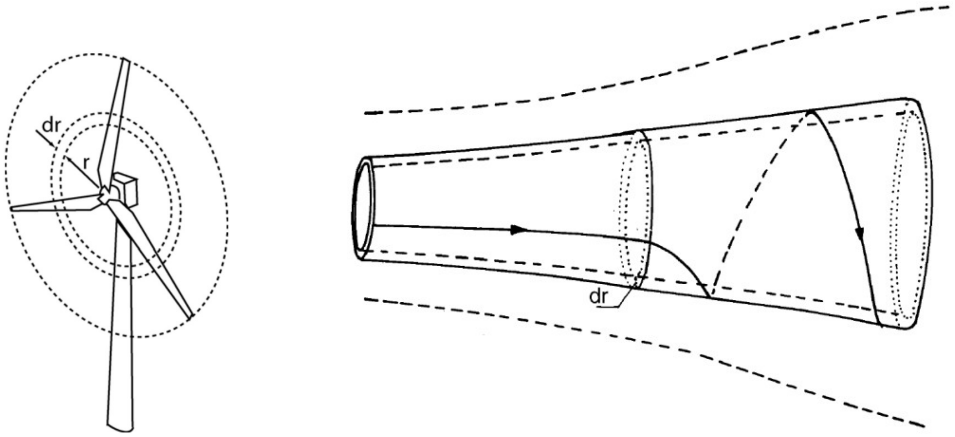

(a) Annular ring [17]

(b) Annular streamtube [31]

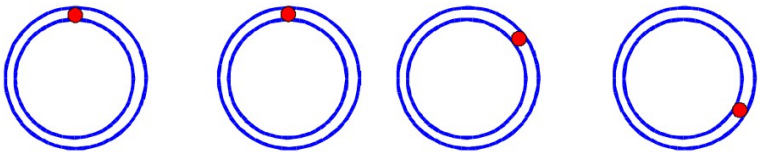

(c) Annular motion in the wake field [19]

Figure 2.16.: Wind turbine wake rotation

2.2.3. Blade element theory

The responsible for the rate of change of momentum of the air that passes through a rotor annulus in the rotor plane is the aerodynamic lift (and drag) on a spanwise blade element [8].

The lift and drag force acting on a airfoil according to Section 2.1.4 are

$$L = C_L \frac{\rho}{2} W^2 c \tag{2.44}$$

$$D = C_D \frac{\rho}{2} W^2 c \tag{2.45}$$

The apparent wind W is composed of the induced velocities in axial and tangential direction,

see Figure 2.17. The tangential velocity component is the sum of the tangential velocity of the blade ($r\Omega$) and the tangential velocity of the wake in the middle of the rotor disc ($r\Omega a'$) [8].

$$W = \sqrt{\left(U_\infty \left(1-a\right)\right)^2 + \left(r\Omega \left(1+a'\right)\right)^2} \tag{2.46}$$

$$\sin\phi = \frac{U_\infty \left(1-a\right)}{W} \qquad \cos\phi = \frac{r\Omega \left(1+a'\right)}{W} \tag{2.47}$$

$$\tan\phi = \frac{U_\infty \left(1-a\right)}{r\Omega \left(1+a'\right)} \tag{2.48}$$

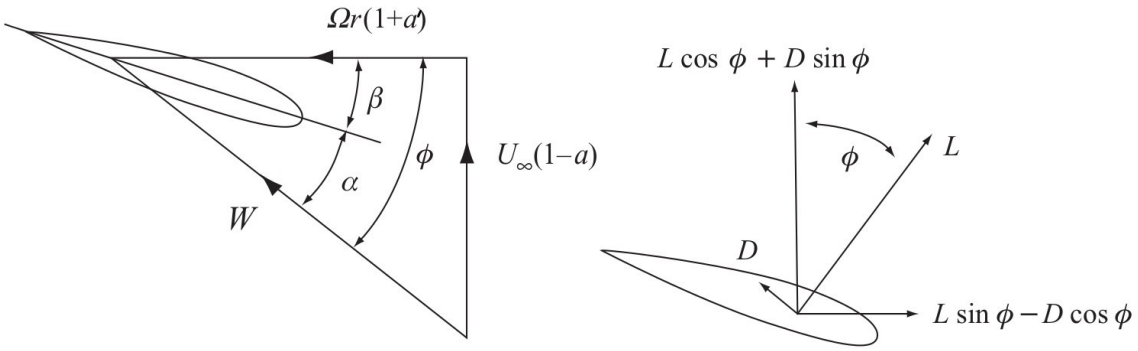

Figure 2.17.: Local blade element velocities, flow angles and aerodynamic forces [8]

The resulting aerodynamic forces can be split into a component perpendicular to the rotor plane and a tangential component in the rotor plane.

$$F_T = F_{ADn} = L\cos\phi + D\sin\phi \tag{2.49}$$

$$F_{ADt} = L\sin\phi - D\cos\phi \tag{2.50}$$

Considering a blade element with a span-wise length of dr and B blades the local thrust force and the local torque acting on an annular ring are as follows

$$dF_T = dL\cos\phi + dD\sin\phi = \frac{1}{2}\rho W^2 Bc \underbrace{\left(C_L\cos\phi + C_D\sin\phi\right)}_{C_n} dr \tag{2.51}$$

$$dQ = \left(dL\sin\phi - dD\cos\phi\right) r = \frac{1}{2}\rho W^2 Bcr \underbrace{\left(C_L\sin\phi - C_D\cos\phi\right)}_{C_t} dr \tag{2.52}$$

The inflow angle ϕ is composed of a local twist angle β plus the local angle of attack α.

$$\phi = \alpha + \beta \tag{2.53}$$

The apparent wind direction changes with the radial position because the tangential component becomes larger while the axial component keeps constant, when neglecting the wind shear due to the atmospheric boundary layer. This results in very large inflow angles near the blade root. In order to keep the angle of attack nearly constant the inflow angle has to be

adjusted by a blade twist angle β over the blade span. The blade at the blade root is twisted more than in the tip region. Figure 2.18 shows the varying velocity triangles along the span because of an increasing induced tangential velocity component.

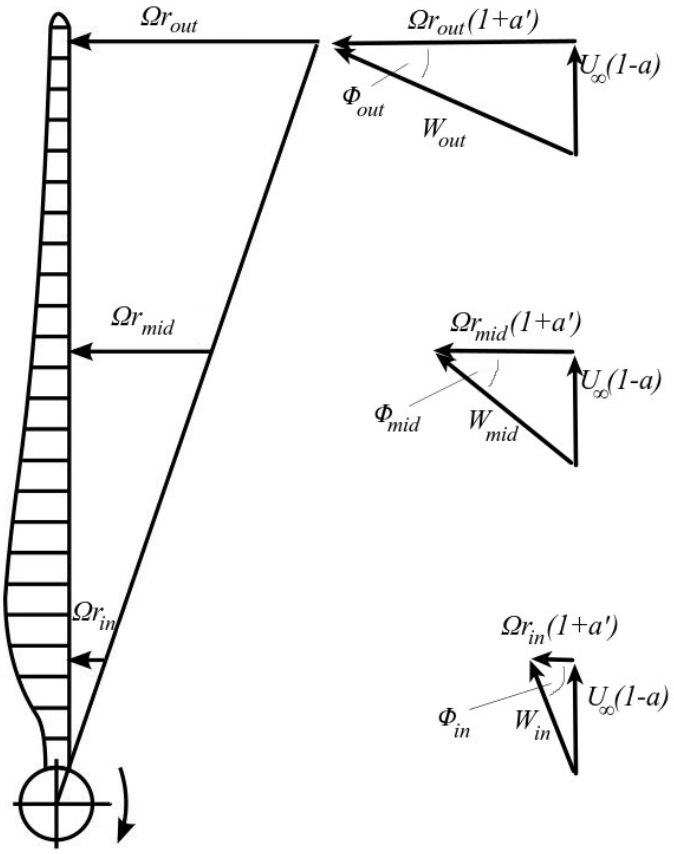

Figure 2.18.: Wind triangular for different radial positions

2.2.4. Vortex system behind a wind turbine

As discussed in Section 2.1.4 a sheet vortex forms behind a wing with a non constant lift distribution. As a consequence the vortex sheets of a rotating wing convects in an helicoidal pattern with the wake velocity in flow direction. Figure 2.19 sketches the vortex system behind a wind turbine rotor.

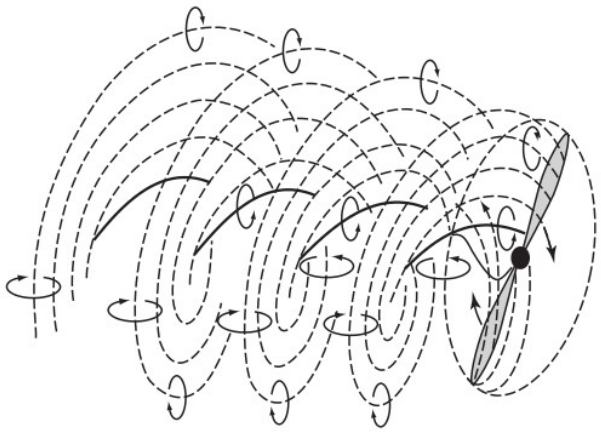

Figure 2.19.: Vortex system behind a wind turbine [8]

2.3. Acoustic Theory

This Section covers acoustic fundamentals. Section 2.3.1 describes the human ear. Important acoustical quantities, that characterize and quantify human sound perception, are introduced in Section 2.3.2. After that the basic acoustic wave equation for sound propagation is derived in Section 2.3.3. The sound source region is assumed to be stagnant. Later in this Section more general formulations of the acoustic wave equation for arbitrary sound source regions (aeroacoustic analogies) are described in 2.3.7.

2.3.1. The human ear

The human ear normally covers an audible range of about 16Hz to 20kHz. Due to its anatomy it is not equally sensitive to all the frequencies. For instance humans are most sensitive to frequencies in the range of about 1 - 4 kHz.[5]

The 20kHz upper limit of hearing refers to young people in their twenties. After that, hearing decreases 1kHz for every decade of life. The ear is the human organ responsible for audible perception. Figure 2.20 shows a schematic of the human acoustic sensory organ. It is divided in three sections, the outer ear (pinna and ear canal), the middle ear (hammer, anvil, stirrup and the eustachian tube[6]) and inner ear where the cochlea sits. Arriving pressure waves cause the eardrum to oscillate. The three small bones in the middle ear act as mechanical transducers, adapting the impedance of the air with the considerably higher impedance of the lymphatic fluid inside the cochlea [11]. They transmit the incoming vibrations of the eardrum to the oval window of the cochlea in the inner ear. The hammer is connected to the ear drum and the stirrup is connected to the oval window.

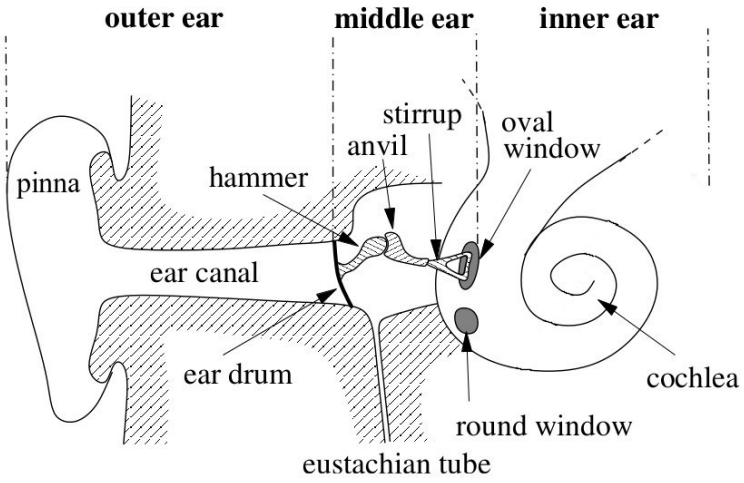

Figure 2.20.: Schematic of human ear [11]

The cochlea is a canal filled with lymphatic fluid with a shortcut at the *helicotrema*. The canal is divided by the *basilar membrane* into a upper and a lower side. Figure 2.21 shows the unwound cochlea.[7] The excitations of the oval window make the fluid in the cochlea to oscillate. Depending on the excited frequency of the lymphatic fluid in the cochlea the basilar

[5] The ear canal forms a one-sided open tube. Therefore for an ear canal with an estimated length of 2 - 2.5 cm resonance occurs at frequencies around 3 - 4 kHz. Police whistles for instance make use of this effect.
[6] The eustachian tube connects the inner ear with the throat because of pressure compensation reasons.
[7] The unwound cochlea is about 3cm long [30].

membrane deforms accordingly. The rigidity of the basilar membrane is not constant along its length. It is most rigid on the side of the oval window with decreasing stiffness towards the helicotrema [30]. Therefore, the basilar membrane shows a frequency dependent deformation pattern, as sketched in Figure 2.21. The locally uneven distributed deflections of the basilar membrane are sensed by the *Cortian organ* which sits on the membrane (not shown in Figure 2.21). This determines whether an incoming acoustic signal is perceived as high (deformation near oval window = perception of high frequencies) or low (deformation near helicotrema = perception of low frequencies) pitch. Thus, the ear performs a complete frequency analysis of the incoming acoustic signal [30].

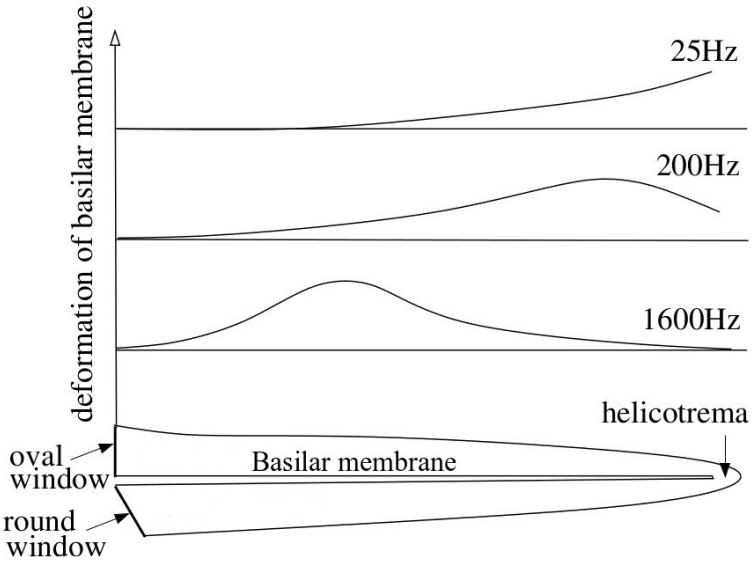

Figure 2.21.: Deformation of the Basilar membrane [11]

Due to a broad variety of sources of sound in every day life, the human ear is constantly exposed to these pressure perturbations and the human brain is trying to interpret these input signals.

Different sensations can be clearly distinguished.

- **tone** (pure sine wave, is characterized by its frequency and the number of cycles per second)
- **complex tone** (superposition of tones)
- **noise** (superposition of a stochastic frequency content and complex tones)
- **impulse** (short duration sound event)

2.3.2. Sound quantities

2.3.2.1. Acoustic pressure

Acoustic pressure waves propagate from an acoustic source to the receiver. This causes small changes of the local pressure in a compressible media, such as air. These unsteady pressure fluctuation p', which are superimposed over a steady temporal averaged pressure p_0, mostly the ambient atmospheric pressure, is called the acoustic or sound pressure.

$$p(t) = p_0 + p' \tag{2.54}$$

A more appropriate measure of the strength of a signal is the *root mean square* pressure, which is the effective value of the acoustic pressure.

$$\overline{p} = \sqrt{\overline{(p')^2}} \tag{2.55}$$

2.3.2.2. Logarithmic scale

The *Weber-Fechner-law* The sensory perception of humans roughly follows a logarithmic scale. This is presumably evolutionary related. Small changes in sensation at a lower level are more easy perceptible than big changes at a higher level.

The *Weber-Fechner-law* of '*relative change*' says that a change in sensation ΔE is proportional to the quotient of an absolute increase in stimulus ΔS, to the initial value of the stimulus S [25].

$$\Delta E = k\,\frac{\Delta S}{S} \tag{2.56}$$

The integration for infinitesimally small changes yields[8]

$$E = k \ln\left(\left|\frac{S}{S_0}\right|\right) = 2.3k\log_{10}\left(\frac{S}{S_0}\right) \tag{2.57}$$

Sound pressure level This characteristic can be translated into how sound is perceived. The sound pressure level SPL quantifies human sensation of sound. The stimulus is the sound pressure as discussed before. Humans can perceive acoustic pressure amplitudes as low as $\overline{p}_{min} = 2 \cdot 10^{-5} Pa$ (*threshold of hearing*) and as high as $\overline{p}_{max} = 2 \cdot 10^{2} Pa$ (*threshold of pain*). The lower level in perceivable sound pressure represents the reference pressure p_{ref}. This is an international standard and the sound pressure level, as a quantity of human sound perception, follows as

$$SPL := 10\log_{10}\left(\frac{\overline{p}^2}{p_{ref}^2}\right) = 20\log_{10}\left(\frac{\overline{p}}{p_{ref}}\right) \qquad [dB] \tag{2.58}$$

$$p_{ref} := 2 \cdot 10^{-5} Pa \tag{2.59}$$

Table B.2 gives a short overview of general sound pressure levels in everyday life.

Sound intensity Furthermore the *sound intensity* $\boldsymbol{I}$ with the corresponding *sound intensity level* L_I is defined as following.

The sound intensity is derived from the acoustic pressure and the *acoustic particle velocity* $\boldsymbol{v}'$. It is to be noted that the acoustic particle velocity is entirely different from the "speed of sound".

[8] $\ln(x) = \log_e(x) = \frac{\log_{10}(x)}{\log_{10}(e)} = \frac{1}{0.434}\log_{10}(x)$

$$\boldsymbol{I}(x) := \overline{p'\boldsymbol{v}'} \tag{2.60}$$

$$L_I := 10\log_{10}\left(\frac{|\boldsymbol{I}|}{I_{ref}}\right) \qquad [dB] \tag{2.61}$$

$$I_{ref} := 10^{-12}\mathrm{W/m^2} \tag{2.62}$$

Sound power The sound power P_W is the integration of the sound intensity I over a closed surface A

$$P_W := \oint_A \boldsymbol{I} \cdot \boldsymbol{n}\, dA \tag{2.63}$$

The *sound power level* L_W is

$$L_W := 10\log_{10}\left(\frac{P}{P_{ref}}\right) \qquad [dB] \tag{2.64}$$

$$P_{W_{ref}} := 10^{-12}W \tag{2.65}$$

Logarithmic level addition A total sound pressure level from various levels can be added up with the level addition method.

$$TOTAL = 10\log_{10}\sum 10^{SPL_i/10} \tag{2.66}$$

For example two sound sources of equal same sound pressure level add $3\,dB$ to total sound pressure level.

$$TOTAL = 10\log_{10}\left(2\cdot 10^{SPL_i/10}\right) = 10\log_{10}10^{SPL_i/10} + 10\log_{10}2 = SPL_i + 3\,dB$$

2.3.2.3. Frequency weighting

Besides the logarithmic type of perception of sensation of humans the human ear has its own characteristic in being differently sensitive to various frequency bands in the audible range. In the early to mid 20th century field tests with a large group of test persons where carried out to investigate this issue. Each person had to adjust the level of the actual tone at a certain frequency to a reference tone at 1kHz at a certain level until the perceived levels of both signals where believed to be equal. These tests resulted in the following plot (Figure 2.22) of ($ELLC$) and became later internationally standardized in the ISO226.

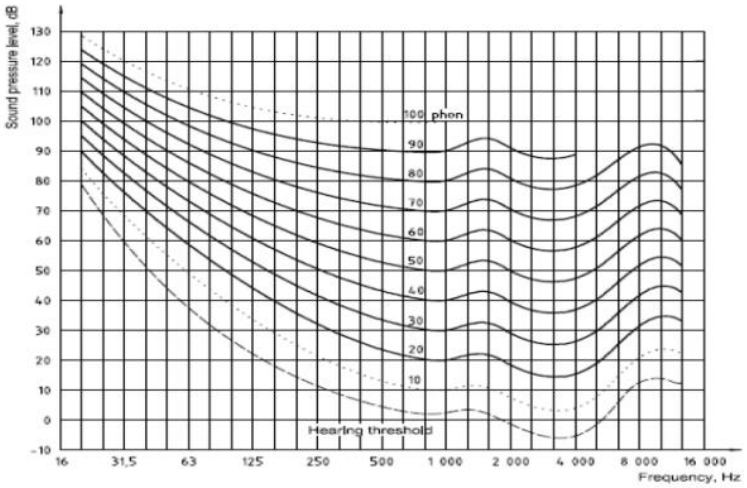

Figure 2.22.: Equal-loudness-level contours [4]

Based on the *ELLC* noise weighting comes into play, where the A-weighted curve approximately follows the negative moderately intense $30\,phon$ curve [25].[9] Furthermore B- and C-weighting curves are defined as Figure 2.23 illustrates. The D-weighting curve plays only a minor role. The A-weighting is the most widely used weighting. Sound levels with a specific weighting applied are indexed with the weighting filter character ($SPL \longrightarrow SPL_A$).

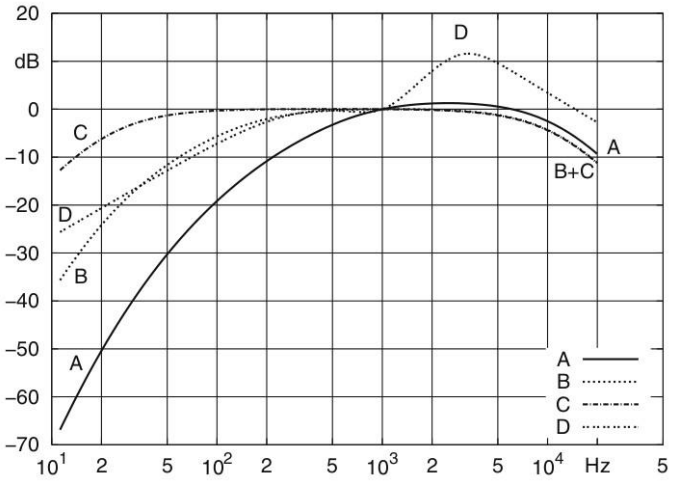

Figure 2.23.: A-, B- and C-weighting curves [25]

2.3.2.4. Frequency bands

For the sake of comparability in acoustic analysis *octave band spectra*, spectra of relative constant bandwidth, are used. Neighboring frequencies in a specific frequency band are lumped together in one labeling frequency domain. The width of the band is proportional to the center frequency so that with a growing center frequency the bandwidth also increases. Mostly *octave band spectra* and *one-third octave band spectra* are used.

Table B.1 lists the center frequencies of the one-third octave band spectrum and the related lower and upper cut-off frequencies. Furthermore, this Table includes the A-weighting values at every center frequency.

[9] $30\,phon$ corresponds to $30\,dB$ at 1kHz.

2.3.3. Governing equations

Sound is caused by small pressure perturbations of the ambient pressure level. If there is no medium which can support pressure fluctuations there is no sound, hence the presence of a fluid is crucial for the propagation of sound. Since sound waves also indicate a sort of fluid motion one can apply the basic governing equations of fluid dynamics to describe the "movement" of sound waves.

The objective is to derive an equation which describes the sound pressure field. This can be done by rearranging the basic governing equations of conservation of mass, momentum and energy (*Navier-Stokes equations*) into an acoustic wave equation.

Certain assumptions have to be made, i.e. constant density, stagnant or homogeneous mean flow. Viscous friction is also neglected as well as heat conduction. The derivation of the acoustic wave equation, to describe the acoustical behavior of a fluid, in this Section and following Sections 2.3.4, 2.3.5 and 2.3.7 follow the remarks of Delfs [11].

It might be convenient for some applications in engineering to use simpler formulations of the NS-equations. In terms of acoustics it is more suitable to use the so called *primitive formulation* of the NS-equations.

$$\frac{D\rho}{Dt} = -\rho\boldsymbol{\nabla}\cdot\boldsymbol{v} + \overbrace{\dot{m}}^{!} \tag{2.67}$$

$$\rho\frac{D\boldsymbol{v}}{Dt} = -\boldsymbol{\nabla}p + \boldsymbol{\nabla}\cdot\underline{\boldsymbol{\tau}} + \boldsymbol{f} \tag{2.68}$$

$$\rho\frac{De}{Dt} = -p\boldsymbol{\nabla}\cdot\boldsymbol{v} + \underline{\boldsymbol{\tau}} : \boldsymbol{\nabla}\boldsymbol{v} - \boldsymbol{\nabla}\cdot\boldsymbol{q} + \dot{\vartheta} \tag{2.69}$$

The path to derive equations 2.67, 2.68 and 2.69 is described in Section A.3. Note, that a hypothetical independent mass flow term $\dot{m}$ is introduced in equation 2.67 (see also equation A.9) to account for a mass injection process which might not be covered by an actual computing regime, e.g. one dimensional studies of a long pipe with radial mass injection. But, of course, mass cannot be created in a setup of classical mechanics ($\dot{m} = 0$) [11]. Accordingly, equations A.10 and A.11 are adjusted for transported momentum and energy as well but these terms drop out in the derivation process of equations 2.67, 2.68 and 2.69 in Section A.3.

Furthermore, the first law of thermodynamics is introduced $\left(Tds = dh - \frac{1}{\rho}dp = de + pd\left(\frac{1}{\rho}\right)\right)$[10] in order to involve the entropy as a variable. For d, $dt \cdot \frac{D}{Dt}$ is used, which can be understood as the material change of a particle along its pathline. This yields

$$T\frac{Ds}{Dt} = \frac{De}{Dt} - \left(\frac{p}{\rho^2}\right)\frac{D\rho}{Dt} \tag{2.70}$$

Multiplied with ρ/T gives

[10] $pd\left(\frac{1}{\rho}\right) = pd\left(\rho^{-1}\right)$, hence, $\frac{d\left(\rho^{-1}\right)}{d\rho} = -\frac{1}{\rho^2}$. Therefore $pd\left(\frac{1}{\rho}\right) = -\frac{p}{\rho^2}d\rho$.

$$\rho \frac{Ds}{Dt} = \frac{1}{T}\left[\rho \frac{De}{Dt} - \left(\frac{p}{\rho}\right)\frac{D\rho}{Dt}\right] \tag{2.71}$$

Inserting equation 2.67 and 2.69 in 2.71 yields

$$\rho \frac{Ds}{Dt} = \frac{1}{T}\left[\underline{\boldsymbol{\tau}} : \boldsymbol{\nabla}\boldsymbol{v} - \boldsymbol{\nabla}\cdot\boldsymbol{q} + \dot{\vartheta} - \left(\frac{p}{\rho}\right)\dot{m}\right] \tag{2.72}$$

Equation 2.72 is the entropy equation and is derived by combining the laws of conservation of mass and energy with the first law of thermodynamics. This equation states that the entropy change in a system is dependent on the dissipative energy, heat conduction across the boundaries as well as a possible heat source within the boundaries. Also the injection or abstraction of mass can change the entropy.

Since the last three terms from the right hand side can be zero, or at least change their algebraic sign, things are different for the first term. This term is the vicious dissipation function ($\Phi_\mu := \underline{\boldsymbol{\tau}} : \boldsymbol{\nabla}\boldsymbol{v} \geq 0$). In a system energy always gets dissipated because of viscous friction within the boundaries.

For a confined system it might be true that the change of entropy can become negative because i.e. the heat conduction out of the system is much bigger than viscous friction in the system, but when the control volume is defined just wide enough the change of entropy will never be negative. Only for the ideal case of a reversible process it can reach zero. This is the *second law of thermodynamics*.

One more equation is needed to close the system of equations. Therefore, a thermodynamic relation between two variables of state is introduced. The density is appointed as a function of pressure and specific entropy, hence $\rho = \rho(p, s)$.

$$d\rho = \underbrace{\left(\frac{\partial\rho}{\partial p}\right)_s}_{=:\frac{1}{c_0^2}} dp + \underbrace{\left(\frac{\partial\rho}{\partial s}\right)_\rho}_{=:-\rho\sigma} ds \tag{2.73}$$

Again a change of a particle along its pathline $\left(d = dt \cdot \frac{D}{Dt}\right)$ is considered. This gives

$$\frac{1}{c_0^2}\frac{Dp}{Dt} = \frac{D\rho}{Dt} + \sigma\rho\frac{Ds}{Dt} \tag{2.74}$$

Inserting equations 2.67 and 2.72 in 2.74 yields an expression for the pressure

$$\frac{1}{c_0^2}\frac{Dp}{Dt} = -\rho\boldsymbol{\nabla}\cdot\boldsymbol{v} + \frac{\sigma}{T}\left(\underline{\boldsymbol{\tau}} : \boldsymbol{\nabla} - \boldsymbol{\nabla}\cdot q + \dot{\vartheta}\right) + \dot{m}\left(1 - \frac{\sigma}{T}\frac{p}{\rho}\right) \tag{2.75}$$

Equations 2.67, 2.68 and 2.75 are a set of governing equations for density, velocity and pressure of an acoustic field. Next expressions for the yet unknown terms $\left(\frac{\partial\rho}{\partial p}\right)_s =: \frac{1}{c_0^2}$ and $\left(\frac{\partial\rho}{\partial s}\right)_\rho =: -\rho\sigma$ are derived in case of a perfect gas.

$$pv = RT \tag{2.76}$$

$$de = c_v dT \tag{2.77}$$

$$dh = c_p dT \tag{2.78}$$

First the derivative of equation 2.76 is formed.

$$pd\left(\frac{1}{\rho}\right) + \frac{1}{\rho}dp = -\frac{p}{\rho^2}d\rho + \frac{1}{\rho}dp = RdT \tag{2.79}$$

Then first law of thermodynamics

$$Tds = de + pd\left(\frac{1}{\rho}\right) = c_v dT - \frac{p}{\rho^2}d\rho$$

is transformed into

$$d\rho = \frac{\rho^2}{p}c_v dT - \frac{\rho^2}{p}ds \tag{2.80}$$

Next equation 2.79 is inserted into equation 2.80 and after rearranging this yields

$$d\rho = \left(\frac{\frac{c_v}{R}\frac{\rho}{p}}{1+\frac{c_v}{R}}\right)dp + \left(-\frac{T\frac{\rho^2}{p}}{1+\frac{c_v}{R}}\right)ds$$

Further rearrangement with respect to $R = c_p - c_v$ and $\kappa = \frac{c_p}{c_v}$ finally leads to

$$d\rho = \left(\frac{1}{\kappa RT}\right)dp + \left(-\frac{\rho}{c_p}\right)ds$$

Comparing with equation 2.73 indicates that $c_0 = \sqrt{\kappa RT}$[11] and that $\sigma = \frac{1}{c_p}$. c_0 is the *speed of sound*.

The final governing system of equations for the acoustic behavior of a perfect gas reads as follows (where viscous friction and heat conduction are neglected)

$$\frac{D\rho}{Dt} + \rho\boldsymbol{\nabla}\cdot\boldsymbol{v} = \dot{m} \tag{2.81}$$

$$\rho\frac{D\boldsymbol{v}}{Dt} + \boldsymbol{\nabla}p = \boldsymbol{f} \tag{2.82}$$

$$\frac{1}{c_0^2}\frac{Dp}{Dt} + \rho\boldsymbol{\nabla}\cdot\boldsymbol{v} = \frac{\sigma}{T}\dot{\vartheta} + \left(1 - \frac{\sigma}{T}\frac{p}{\rho}\right)\dot{m} \tag{2.83}$$

2.3.4. Linearized gas dynamics

The actual responsible for the sensation of sound is the time depended fluctuating sound pressure p'. One fluctuating property in a fluid domain induces, to a greater or lesser extent, other fluctuating properties. Hence, all flow variables can be composed of a mean steady value plus a small, but unsteady perturbation.

To account for the smallness of the striped values $\epsilon \ll 1$ is used.

$$(p, \boldsymbol{v}, \rho, ...) = \left(p_0 + \epsilon p', \boldsymbol{v}_0 + \epsilon\boldsymbol{v}', \rho_0 + \epsilon\rho', ...\right) \tag{2.84}$$

[11] The Speed of sound for dry air: $\kappa = 1.4$, $R = 287\frac{J}{kg\cdot K}$, $T = 288K \Longrightarrow c_0 = \sqrt{1.4\cdot 287\cdot 288} = 340.2^{m}/_{s}$

Equation 2.84 is inserted into equations 2.81, 2.82 and 2.83 assuming that the mean value of the source terms are zero $\left(\dot{m}_0 = \boldsymbol{f}_0 = \dot{\vartheta}_0 = 0\right)$.

This process is demonstrated in A.4 only based on equation 2.81.

2.3.5. Acoustics in a stagnant homogeneous media: The acoustic wave equation

Considering the case of zero mean flow $\boldsymbol{v}_0 = 0$ and that the mean density is constant in space and time $\rho_0 \neq \rho_0(x,t)$ equations A.18, A.19 and A.20 simplify to

$$\frac{\partial \rho'}{\partial t} + \rho_0 \boldsymbol{\nabla} \cdot \boldsymbol{v}' = \dot{m}' \tag{2.85}$$

$$\rho_0 \frac{\partial \boldsymbol{v}'}{\partial t} + \boldsymbol{\nabla} p' = \boldsymbol{f}' \tag{2.86}$$

$$\frac{1}{c_0^2}\frac{\partial p'}{\partial t} + \rho_0 \boldsymbol{\nabla} \cdot \boldsymbol{v}' = \underbrace{\frac{\sigma_0}{T_0}\dot{\vartheta}' + \left(1 - \frac{\sigma_0}{T_0}\frac{p_0}{\rho_0}\right)\dot{m}'}_{\left[\frac{\kappa-1}{c_0^2}\dot{\vartheta}' + \frac{1}{\kappa}\dot{m}'\right]_{pg}} \tag{2.87}$$

This is the final set of equations to derive the acoustic wave equation.

1. Take the divergence of equation 2.86

$$\rho_0 \frac{\partial}{\partial t}\left(\boldsymbol{\nabla} \cdot \boldsymbol{v}'\right) = -\boldsymbol{\nabla} \cdot \boldsymbol{\nabla} p' + \boldsymbol{\nabla} \cdot \boldsymbol{f}'$$

2. Then take the time derivative of 2.87

$$\frac{1}{c_0^2}\frac{\partial^2 p'}{\partial t^2} + \rho_0 \frac{\partial}{\partial t}\left(\boldsymbol{\nabla} \cdot \boldsymbol{v}'\right) = \frac{\partial}{\partial t}\left[\frac{\kappa - 1}{c_0^2}\dot{\vartheta}' + \frac{1}{\kappa}\dot{m}'\right]_{pg}$$

3. Eliminating the divergence of the velocity perturbation yields the *acoustic wave equation.*

$$\frac{1}{c_0^2}\frac{\partial^2 p'}{\partial t^2} - \boldsymbol{\nabla}^2 p' = \frac{\partial}{\partial t}\dot{\Theta}' - \boldsymbol{\nabla} \cdot \boldsymbol{f}' = Q_P \tag{2.88}$$

$$Q_p = \frac{\sigma_0}{T_0}\frac{\partial \dot{\vartheta}'}{\partial t} + \left(1 - \frac{\sigma_0}{T_0}\frac{p_0}{\rho_0}\right)\frac{\partial \dot{m}'}{\partial t} - \boldsymbol{\nabla} \cdot \boldsymbol{f}' \tag{2.89}$$

$$Q_p = \left[\frac{\kappa - 1}{c_0^2}\frac{\partial \dot{\vartheta}'}{\partial t} + \frac{1}{\kappa}\frac{\partial \dot{m}'}{\partial t}\right]_{pg} - \boldsymbol{\nabla} \cdot \boldsymbol{f}' \tag{2.90}$$

The r.h.s. of equation 2.88 are the sources of sound Q_p. Unsteady mass and heat flow as well as unsteady forcing exerted on the fluid are sources of sound. It can be shown that if these sources are known variables one can obtain the resulting acoustic pressure field by integrating over all sources in a finite source region.

$$p'(\boldsymbol{x}, t) = \frac{1}{4\pi}\int_{V_S} \frac{Q_p(\tau, \boldsymbol{y})}{r_S} dV_S \tag{2.91}$$

$\boldsymbol{x}$ and t are the spatial and temporal coordinates of the sound pressure field. The sound sources are exerted on the fluid some time earlier at a *retarded time*[12] $\tau = t - \frac{r_S}{c_0}$ and at the *source location* $\boldsymbol{y}$. r_S is the distance between the sound source and the listeners position and is determined through $r_S = |\boldsymbol{x} - \boldsymbol{y}|$. Figure 2.24 sketches this situation.

The fact that the acoustic pressure decays with $(4\pi r_S)^{-1}$ is because of assumed three dimensional spherical wave propagation.

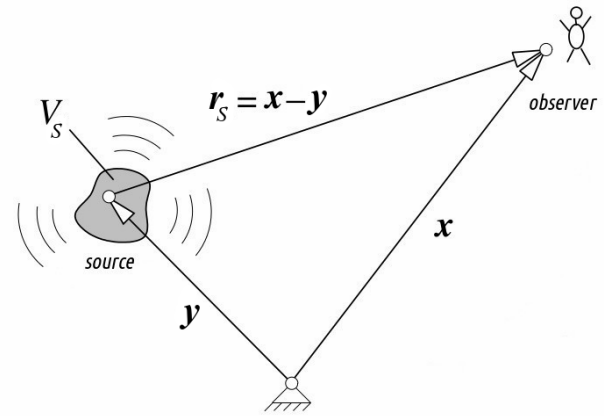

Figure 2.24.: Sound propagation distance [11]

2.3.6. Model sound sources

The acoustic pressure field is fully defined once the source terms Q_p are known variables. To get a better insight into the characteristics of sound source terms one can combine elementary model sound sources in order to model more complex source structures. These elementary shapes are a pulsating or breathing sphere, an oscillating sphere and a combination of both, a breathing and/or oscillating sphere, monopoles, dipoles and quadrupoles respectively. Figure 2.25 shows the three types of model sound sources.

The mass and heat sources from equation 2.90 correspond to a monopole source. Forces exerted on a flow a are related to dipoles.

A formal way to expand the multipole sound source Q_p into its elementary components can be done with a *multipole expansion* [11, 32].

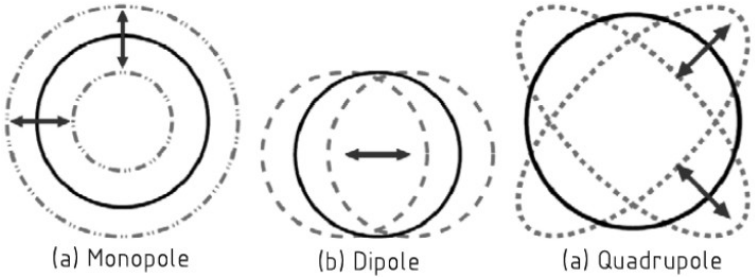

Figure 2.25.: Model sound sources [30]

[12]The *retarded time* is the time it takes the pressure waves to arrive at the listeners position $\boldsymbol{x}$.

2.3.7. Acoustics in a turbulent flow: Aeroacoustic analogies

In Section 2.3.5 the influence of mass and heat sources or of an imposed external force field on the generation of sound in an elsewhere quiescent fluid domain is discussed. An inhomogeneous wave equation, assuming that these sources induce very small perturbations out of the reference quiescent fluid state, is derived. The source region is assumed to be in a stagnant quiescent domain.

In this Section the subtle difference is to look at arbitrary source regions. The idea behind aeroacoustic analogies is to formulate a wave equation with sources located in an arbitrary flow field. Therefore the exact NS-equations are rearranged into a wave equation as described below. Only the listener stand outside in assumed quiescent conditions where the inhomogeneous wave equation reduces to the homogeneous wave equation of standard free field sound propagation. Aeroacoustic analogies represent a generalization of the inhomogeneous wave equation 2.88 [32].

2.3.7.1. Lighthill's analogy

Sir J. Lighthill first derived his famous analogy out of the exact NS-equations in 1952 motivated by the extreme noise originating from jet turbines. He found that the noise from a jet is proportional to the eighth power of the jet velocity.[13]

The derivation is quite simple.

1. Take the time derivative from equation 2.3 with zero mass source $\dot{m}$.

$$\frac{\partial^2 \rho}{\partial t^2} + \frac{\partial}{\partial t} \boldsymbol{\nabla} \cdot (\rho \boldsymbol{v}) = 0 \tag{2.92}$$

2. Then take the divergence from equation 2.2

$$\frac{\partial}{\partial t} \boldsymbol{\nabla} \cdot (\rho \boldsymbol{v}) = -\boldsymbol{\nabla} \cdot \boldsymbol{\nabla} \cdot (\rho \boldsymbol{v}\boldsymbol{v}) - \boldsymbol{\nabla} \cdot \boldsymbol{\nabla} p + \boldsymbol{\nabla} \cdot \boldsymbol{\nabla} \cdot \underline{\boldsymbol{\tau}} + \boldsymbol{\nabla} \cdot \boldsymbol{f} \tag{2.93}$$

3. Subtract equation 2.93 from 2.92

$$\frac{\partial^2 \rho}{\partial t^2} = \boldsymbol{\nabla} \cdot \boldsymbol{\nabla} \cdot (\rho \boldsymbol{v}\boldsymbol{v}) + \boldsymbol{\nabla} \cdot \boldsymbol{\nabla} p - \boldsymbol{\nabla} \cdot \boldsymbol{\nabla} \cdot \underline{\boldsymbol{\tau}} - \boldsymbol{\nabla} \cdot \boldsymbol{f} \tag{2.94}$$

4. Subtracting $c_0^2 \triangle \rho$ from both sides of equation 2.94 yields

$$\frac{\partial^2 \rho}{\partial t^2} - c_0^2 \triangle \rho = \boldsymbol{\nabla} \cdot \boldsymbol{\nabla} \cdot \left[(\rho \boldsymbol{v}\boldsymbol{v}) + \left(p - c_0^2 \rho \right) \underline{\boldsymbol{I}} - \underline{\boldsymbol{\tau}} \right] - \boldsymbol{\nabla} \cdot \boldsymbol{f}$$

5. For small perturbations out of the reference state at the listeners position, $\rho' = \rho - \rho_0$ and $p' = p - p_0$, one get the famous *Lighthill analogy*. Note that neither ρ' nor p' are

[13] Knowing about the importance of the jet velocity on the jet noise because of Lighthill's analogy following jet designs in the 1960s aimed at reducing the flow Mach numbers.

necessarily small in the source region.

$$\frac{\partial^2 \rho'}{\partial t^2} - c_0^2 \triangle \rho' = \boldsymbol{\nabla} \cdot \boldsymbol{\nabla} \cdot \underbrace{\left[(\rho \boldsymbol{v}\boldsymbol{v}) + \left(p' - c_0^2 \rho' \right) \underline{\boldsymbol{I}} - \underline{\boldsymbol{\tau}} \right]}_{\underline{\boldsymbol{T}}_L} - \boldsymbol{\nabla} \cdot \boldsymbol{f} \tag{2.95}$$

The Lighthill analogy states that one find additional sources of sound in an arbitrary source region with turbulence occurring. The tensor $\underline{\boldsymbol{T}}_L$ is called the *Lighthill stress tensor* and it vanishes outside the turbulent source region. The stress tensor $\underline{\boldsymbol{T}}_L$ has a quadrupole sound source characteristic.

The forcing $-\boldsymbol{\nabla} \cdot \boldsymbol{f}$ enters identical to equation 2.88. However the mean force $\boldsymbol{f}_0$ can be non zero in an arbitrary turbulent source region. The entropy production term $\left(p' - c_0^2 \rho' \right) \underline{\boldsymbol{I}}$ is a generalization of the heat production term in equation 2.88, however it enters as a quadrupole source term compared to a monopole characteristic before. Furthermore Lighthill also takes the viscous stresses into account as a source of sound. But the most important aspect of equation 2.95 is a sound source due to induced turbulence in the source region, the Reynolds stresses $\rho \boldsymbol{v}\boldsymbol{v}$. One of the key ideas of Lighthill is to neglect viscous forces due to high momentum transport at high flow velocities. When neglecting viscous effects, entropy production and additionally external imposed forcing the sound sources can be approximated by the Reynolds stress term.

$$\underline{\boldsymbol{T}}_L \approx \rho \boldsymbol{v}\boldsymbol{v} \tag{2.96}$$

The classic formulation of the Lighthill analogy 2.95 is expressed in terms of ρ' as the acoustic variable. This is useful when looking at flows with large variations in the speed of sound in the source region.

The Lighthill analogy can also be expressed in terms of p' as in equation 2.97. In that case the effect of entropy fluctuation $\frac{\partial^2}{\partial t^2} \left(\frac{p'}{c_0^2} - \rho' \right)$ has the character of a monopole sound source [32]. Expression 2.97 is best suited to investigate combustion processes with subsonic flames in which entropy production is the dominant sound source [27, 32].

$$\frac{1}{c_0^2} \frac{\partial^2 p'}{\partial t^2} - \triangle p' = \boldsymbol{\nabla} \cdot \boldsymbol{\nabla} \cdot \left[(\rho \boldsymbol{v}\boldsymbol{v}) - \underline{\boldsymbol{\tau}} \right] + \frac{\partial^2}{\partial t^2} \left(\frac{p'}{c_0^2} - \rho' \right) - \boldsymbol{\nabla} \cdot \boldsymbol{f} \tag{2.97}$$

In order to solve equation 2.95 or 2.97 for the acoustic variable the sound sources on the right hand side due to turbulence, entropy production or external forcing on the fluid need to be modeled or simulated numerically. They can be simulated for instance applying CFD techniques to solve the turbulent flow field in the source region [32].

2.3.7.2. Ffowcs-Williams and Hawkings equation

Because Lighthill was aiming at describing noise from jets his analogy does not include the effects of the presence of solid walls in an turbulent source region. Nevertheless in many technical application solid surfaces in a turbulent flow do play a role. Therefore Ffowcs-Williams and Hawkings in 1969 extended Lighthill's analogy to describe the phenomena of noise originating from moving solid objects in a turbulent flow. This makes the Ffowcs-Williams and Hawkings equation a generalization of the Lighthill analogy [13].

For the derivation Ffowcs-Williams and Hawkings applied *generalized functions*. In essence

generalized functions serve as a tool to define all variables in space, even at points of discontinuity. The presence of a moving surface represents such a discontinuity in the flow field. Generalized functions help to formulate time or space derivatives of these parameters required for the governing equations.

After applying generalized functions to the equations of mass and momentum conservation a wave equation is derived the same way as for the derivation of Lighthill's analogy, taking the time derivative from the (generalized) mass equation and subtracting the divergence of the (generalized) momentum equation from it. The derivation of the Ffowcs-Williams and Hawkings is not demonstrated here.

The resulting wave equation can again be expressed in terms of ρ' [11] or p' [32] as the acoustic variable as follows

$$\begin{aligned}\frac{\partial^2}{\partial t^2}\left(\rho' H\right) - c_0^2 \triangle\left(\rho' H\right) = &\boldsymbol{\nabla}\cdot\boldsymbol{\nabla}\cdot\left(\left[(\rho\boldsymbol{v}\boldsymbol{v}) + \left(p' - c_0^2\rho'\right)\underline{\boldsymbol{I}} - \underline{\boldsymbol{\tau}}\right] H\right) - \boldsymbol{\nabla}\cdot(\boldsymbol{f}H) - \\ &- \boldsymbol{\nabla}\cdot\left(\left[\rho\boldsymbol{v}\left(\boldsymbol{v}-\boldsymbol{v}_H\right) + p'\underline{\boldsymbol{I}} - \underline{\boldsymbol{\tau}}\right]\cdot\boldsymbol{\nabla}H\right) + \\ &+ \frac{\partial}{\partial t}\left(\left[\rho\left(\boldsymbol{v}-\boldsymbol{v}_H\right) + \rho_0\boldsymbol{v}_H\right]\cdot\boldsymbol{\nabla}H\right) \end{aligned} \tag{2.98}$$

$$\begin{aligned}\frac{1}{c_0^2}\frac{\partial^2}{\partial t^2}\left(p' H\right) - \triangle\left(p' H\right) = &\boldsymbol{\nabla}\cdot\boldsymbol{\nabla}\cdot\left(\left[(\rho\boldsymbol{v}\boldsymbol{v}) - \underline{\boldsymbol{\tau}}\right] H\right) + \frac{\partial^2}{\partial t^2}\left[\left(\frac{p'}{c_0^2} - \rho'\right) H\right] - \boldsymbol{\nabla}\cdot(\boldsymbol{f}H) - \\ &- \boldsymbol{\nabla}\cdot\left(\left[\rho\boldsymbol{v}\left(\boldsymbol{v}-\boldsymbol{v}_H\right) + p'\underline{\boldsymbol{I}} - \underline{\boldsymbol{\tau}}\right]\cdot\boldsymbol{\nabla}H\right) + \\ &+ \frac{\partial}{\partial t}\left(\left[\rho\left(\boldsymbol{v}-\boldsymbol{v}_H\right) + \rho_0\boldsymbol{v}_H\right]\cdot\boldsymbol{\nabla}H\right) \end{aligned} \tag{2.99}$$

H is the Heaviside function which is $H = 0$ inside the surface and $H = 1$ outside the surface. The first line in equation 2.98 or 2.99 is identical to the source terms of Lighthill's analogy. The multiplication with H indicates that it only acts throughout the volume exterior to the data surface.

The second and third source terms are the surface source terms and are of dipole or monopole character. They are called the *loading noise or thickness noise* terms respectively and can be interpreted as noise that is caused due to an unsteady load distribution on the surface (loading noise) or as noise generated due to the displacement of fluid of the solid surface (thickness noise). The quadrupole sound source is an inefficient sound source for flows at low Mach numbers and can be neglected for such flows [13].

3. Software Models

In Chapter 2 basic aerodynamic aspects of the flow around a wind turbine are outlined as well as a concept to calculate the forcing on the turbine blades. Furthermore, in Section 2.3 it is discussed that forcing exerted on a fluid is a source of sound.

This Chapter describes how the loading on the turbine blades and consequently the acoustic noise emissions of a wind turbine are calculated.

3.1. Overview

In the present master thesis a set of design codes from NREL (National Renewable Energy Laboratory) for aeroelastic modelling of horizontal axis wind turbines is used. The source codes of FAST, AeroDyn and TurbSim are written in FORTRAN and are freely available on NREL's homepage.[1]

FAST (Fatigue, Aerodynamics, Structures and Turbulence) is structural software to simulate torsional and bending modes as well as peak and/or fatigue loading of wind turbines. It works in conjunction with AeroDyn which embodies aerodynamic subroutines to calculate the aerodynamic loading on the blades. FAST controls the whole simulation. AeroDyn gets called by FAST during runtime to calculate the aerodynamic forces of every blade and blade section. First AeroDyn computes the induced velocities and then determines the local actual angle of attack of every blade section. With this angle of attack it calculates the aerodynamic forces based on two-dimensional airfoil polar tables. The airfoil polars of every sectional airfoil profile along the span are listed in input files.

The sectional forces are then integrated over the spanwise direction and FAST updates the structural deflections. The two models available in AeroDyn to calculate the induced velocities are described in Section 3.3.

The integration of FAST and AeroDyn is fully aeroelastic, meaning, that the structural deflections affect the aerodynamic flow around the turbine blades and consequently the aerodynamic loading. The resulting unsteady aerodynamic forces again affect structural calculations of the main program [17].

Furthermore, FAST incorporates a noise prediction subroutine based on semi-empirical aeroacoustic formulations, which are described in Section 3.4. Inputs are the actual angle of attack, the local flow speed vector and information about the turbulence level of the wind. The output of the noise subroutine in FAST is a non-weighted audio spectrum in one-third octave bands at a far field observer position. Note that no atmospheric attenuation is accounted for in the FAST noise subroutine.

[1] http://wind.nrel.gov/designcodes/

The noise output of FAST's inherent noise prediction subroutine is compared to an analytical aeroacoustic approach based on an integral formulation of the Ffowcs-Williams and Hawkings equation, as described in Section 3.5. The loading terms are replaced by a spanwise force distribution.

The source code for the analytical aeroacoustic approach is taken from the OpenFOAM[2] project and adopted for MATLAB. The data handling between FAST and the FWH-code is accomplished with text files. Several modifications to both source codes are made by the author. In terms of FAST an additional loop for multiple observer noise prediction is implemented as well as several data output subroutines. The FWH source code was already set up for multiple observer prediction but an additional loop for n-blades needed to be implemented.

The FWH-code runs post-process to FAST. It reads in data files, generated by FAST, of the blade nodes current position (including blade deflection), velocity vector and the blade nodes current spanwise aerodynamic force vector. All quantities are in reference to FAST's tower base coordinate system with the x-axis positive in the wind direction, the y-axis positive to the left (looking downwind) and the z-axis positive away from the earth's surface and indent with the wind turbine's tower center line, see Figure 3.1. Note, the turbine outlined in Figure 3.1a depicts a downwind turbine.

Additionally, TurbSim was used to generate wind input files for AeroDyn. TurbSim is a full-field, stochastic, turbulent-wind simulator which utilizes statistical modelling of the wind field. More information on TurbSim can be found in [20]. The binary wind input file is generated according to the TurbSim quick-start guidelines for IEC turbulence in [20]. Table 3.1 lists the basic settings for TurbSim as used in the present thesis.

Figure 3.2 outlines the calculation procedure. Before executing the noise calculation several preparatory steps have to be carried out. First the *fast* executable needs to be compiled. Therefore, the *makefile* is set up with preferred settings for the favored compiler, compilation flags (bounds checking, optimization, etc...), object names, the source code locations regarding the local machine of the user, the name of the executable (e.g. *fast*) to name the most important. As a compiler INTEL's *ifort* compiler is used in the present thesis to compile the source code of FAST and AeroDyn. It is freely available for academic use. Alternatively one can also set up the makefile to use the open source *gfortran* compiler.

The second preparatory step is to generate a full field wind file with TurbSim. The TurbSim settings for the Wind.ipt file, used in this thesis, are listed in Table 3.1. TurbSim is executed by entering *TurbSim Wind.ipt* into the terminal.

For a new run, a new folder with all the input files (*.dat, *.ipt, *.wnd) is created. Then one needs to make sure that all the settings in the input files match with the case one wants to investigate. The settings for FAST, AeroDyn and TurbSim, as used in this thesis, are listed in Section 3.2.

[2] http://www.openfoam.com/

(a) FAST tower-base coordinate system [21]

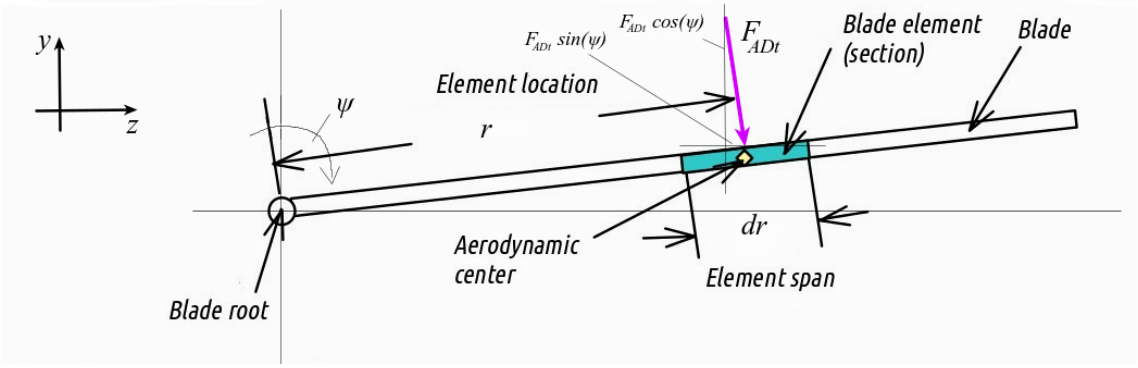

(b) Sketch of the blade element geometry and nomenclature [15]

Figure 3.1.: Coordinate system

The program FAST starts by entering the command *fast *case-name*.ipt.*[3] FAST then concurrently outputs the aerodynamic forces and blade kinematics for all blades and blade elements to output files. After FAST has finished it also outputs the one-third octave noise spectrum file at a far field observer position (*.nos) to the folder.

The FWH-code is executed in MATLAB after FAST has finished. It first reads in all blade force and kinematic files and stores the values in matrices. Then the time curve of the sound pressure at a far field observer position is computed. Finally MATLAB performs a Fourier analysis and plots the final one-third octave band spectrum of the sound pressure time curve. The MATLAB script for the post process audio analysis is written by the author. Main components of it are the *pwelch()* and the new (since MATLAB 8.01) *fdesign* functions.

[3]The file **case-name*.ipt* here represents the FAST_primary.ipt from Figure 3.2.

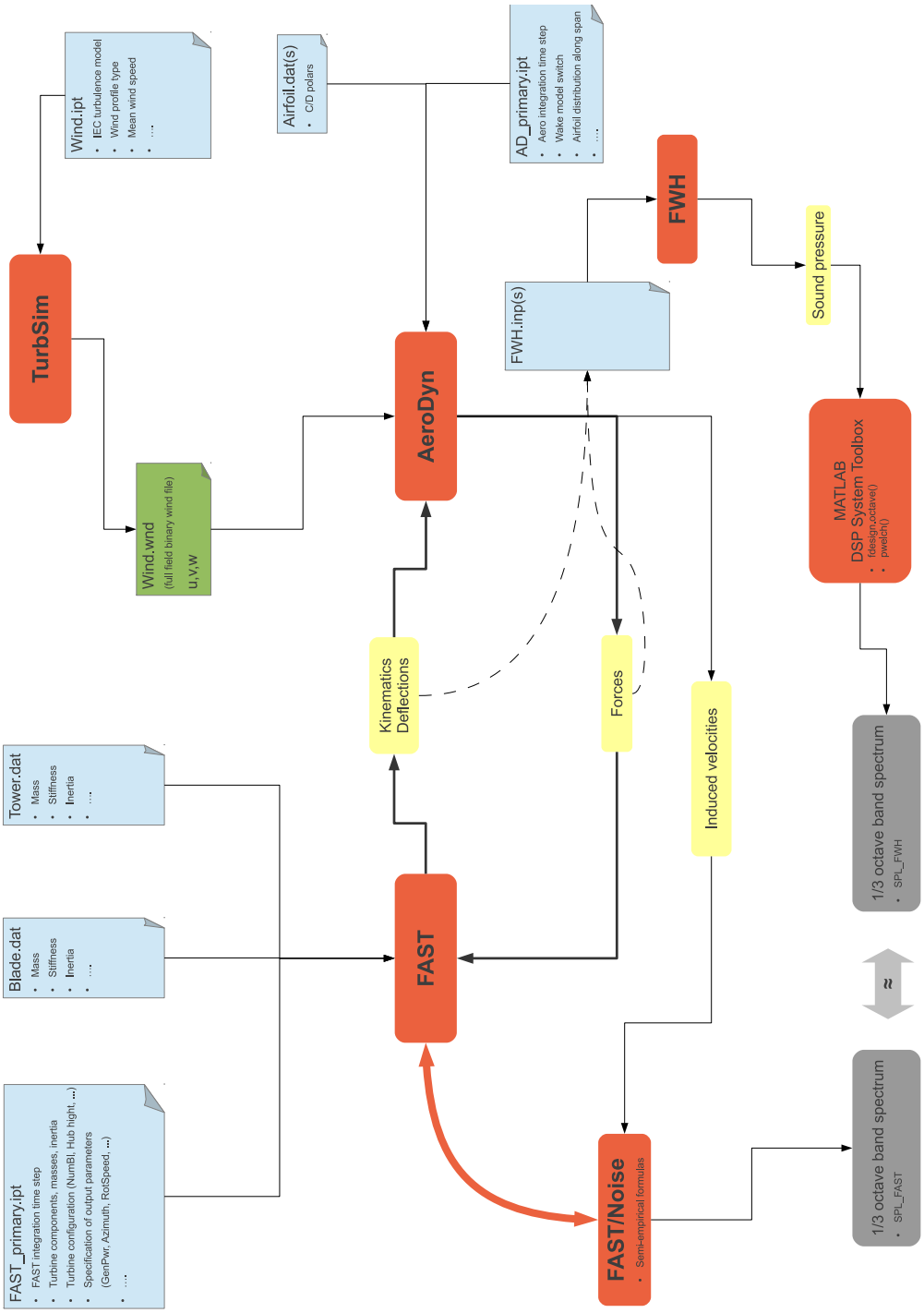

Figure 3.2.: FAST - AeroDyn - TurbSim - FWH interaction

3.2. Software Settings and Wind Turbine Specifications

In the present thesis the noise emissions of a small 50kW downwind wind turbine (AOC 15/50) and a concept study of a 5MW upwind wind turbine (NREL5M) are investigated. A sketch about the upwind and downwind configuration of a wind turbine can be found in Figure 3.3. This Section sums up the software settings for FAST, AeroDyn and TurbSim. Table 3.1 lists the TurbSim settings according to the quick-start guidelines for IEC turbulence in [20]. The input files for FAST, of both wind turbine models, are provided by NREL. The most important basic settings of FAST and AeroDyn are summed in Table 3.2. Table 3.3 presents the key parameter of the investigated wind turbines. Tables 3.4 and 3.5 list the parameters according the airfoil distribution along the span.

Table 3.1.: TurbSim settings

Turbulence model	Kaimal	IECKAI
IEC Standard 61400-x	x=3	1-ED3
IEC turbulence characteristic	B	B
Wind type	Normal	NTM
Wind profile	Power law	PL
Reference height [m]	10	RefHt
Reference wind speed [m/s]	8	URef
Power law exponent	0.143	PLExp
Surface roughness length [m]	0.05	z0

Table 3.2.: Fast/AeroDyn settings

	AOC 15/50	NREL5M	
Time step	0.0001	0.00005	DT/DTAero
Compute aerodynamic forces	True	True	CompAero
Compute aerodynamic noise	True	True	CompNoise
Wake model	GDW	GDW	DYNIN
Stall model	Steady	Steady	STEADY

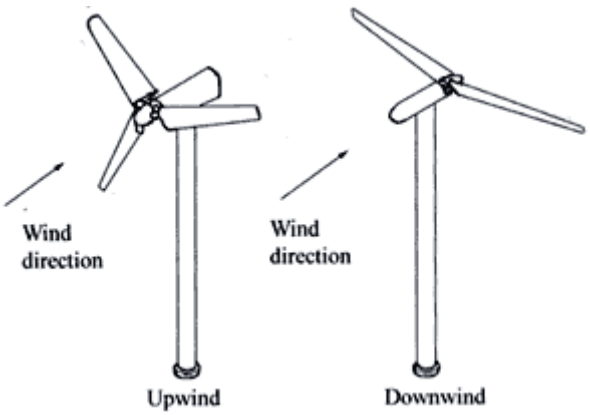

Figure 3.3.: Upwind and downwind turbine configuration of a wind turbine

Table 3.3.: Key parameters of investigated wind turbines

Make and Model	AOC 15/50	NREL5M
Rotation axis (H/V)	horizontal	horizontal
Orientation (upwind/downwind)	downwind	upwind
Number of blades	3	3
Number of blade elements	10	17
Rotor diameter [m]	15	126
Hub height [m]	25	90
Average chord length [m]	0.6	3.4
Average trailing edge thickness [m]	0.006	0.002*
Rated electrical power [kW]	50	5000
Rated wind speed [m/s]	12	11.4
Rotor speed [RPM]	64	12.1
Observer circle radius R_0 [m]	32.5	153

* Default value. No geometrical data of trailing edge bluntness available.

Table 3.4.: Airfoil distribution AOC 15/50 (according to AOC1550_AD.ipt)

Blade node	r [m]	u_t [m/s]	β [deg]	dr [m]	c [m]	d_{TE} [m]	Airfoil
1	0.5150	3.4516	7.6900	0.4700	0.4940	0.0049	S814_1
2	1.1240	7.5331	5.0400	0.7480	0.5790	0.0058	S814_1
3	1.8740	12.5597	4.6000	0.7520	0.6800	0.0068	S814_1
4	2.6240	17.5862	4.2600	0.7480	0.7440	0.0074	S814_1
5	3.3740	22.6128	3.8500	0.7520	0.7380	0.0074	S814_15
6	4.1200	27.6125	3.1500	0.7400	0.6770	0.0068	S814_15
7	4.8700	32.6391	2.4500	0.7600	0.6160	0.0062	S812_15
8	5.6200	37.6656	1.7500	0.7400	0.5580	0.0056	S812_15
9	6.3700	42.6921	1.0500	0.7600	0.4970	0.0050	S813_15
10	7.1200	47.7187	0.3500	0.7400	0.4360	0.0044	S813_15

Table 3.5.: Airfoil distribution NREL5M (according to NREL5M_AD.ipt)

Blade node	r [m]	u_t [m/s]	β [deg]	dr [m]	c [m]	d_{TE} [m]	Airfoil
1	2.8667	3.6324	13.3080	2.7333	3.5420	0.002	Cylinder1
2	5.6000	7.0958	13.3080	2.7333	3.8540	0.002	Cylinder1
3	8.3333	10.5592	13.3080	2.7333	4.1670	0.002	Cylinder2
4	11.7500	14.8885	13.3080	4.1000	4.5570	0.002	DU40_A17
5	15.8500	20.0837	11.4800	4.1000	4.6520	0.002	DU35_A17
6	19.9500	25.2788	10.1620	4.1000	4.4580	0.002	DU35_A17
7	24.0500	30.4740	9.0110	4.1000	4.2490	0.002	DU30_A17
8	28.1500	35.6691	7.7950	4.1000	4.0070	0.002	DU25_A17
9	32.2500	40.8643	6.5440	4.1000	3.7480	0.002	DU25_A17
10	36.3500	46.0594	5.3610	4.1000	3.5020	0.002	DU21_A17
11	40.4500	51.2546	4.1880	4.1000	3.2560	0.002	DU21_A17
12	44.5500	56.4497	3.1250	4.1000	3.0100	0.002	NACA64_A17
13	48.6500	61.6449	2.3190	4.1000	2.7640	0.002	NACA64_A17
14	52.7500	66.8400	1.5260	4.1000	2.5180	0.002	NACA64_A17
15	56.1667	71.1693	0.8630	2.7333	2.3130	0.002	NACA64_A17
16	58.9000	74.6327	0.3700	2.7333	2.0860	0.002	NACA64_A17
17	61.6333	78.0961	0.1060	2.7333	1.4190	0.002	NACA64_A17

3.3. Aerodynamic Model

As mentioned previously AeroDyn performs the aerodynamic calculations in FAST. It calculates the local induced velocities in the rotor plane, the local angle of attack and consequently the aerodynamic forces. This output data together with kinematic information serve as an input for the aeroacoustic calculations. There are two models implemented in AeroDyn to calculate the induced velocities. They are referred to as *wake models*.

The first and most commonly used wake modelling method is the *blade element momentum method* (BEM). The second one is the *generalized dynamic wake model* (GDW). They mainly differ in how changes to an unsteady inflow are treated as an affect on the wake field. In terms of BEM it is assumed that the airflow around the airfoil and the wake are always in equilibrium. That means that the wake reacts instantaneous on given changes of the aerodynamic loadings. In fact the fluid can not accelerate that fast so there is always a finite time lag until the wake reacts to new inflow or turbine operating conditions. A dynamic wake model account for this time lag, especially in highly pitched, transient and/or yawed conditions [35]. Both wake models used by AeroDyn are described briefly in the following Sections.

3.3.1. Blade element momentum theory

Blade element momentum theory (BEM) is one of the oldest and most commonly used wind turbine wake modelling methods. It is a combination of the blade element theory and the momentum theory.

The main idea is to iteratively solve the equations of the blade element and the momentum theory for thrust and torque for the flow inductions factors a and a' in order to calculate the aerodynamic forces that act on the blade.

The BEM does not account for three dimensional phenomena in the airflow around a turbine blade, especially in the tip and hub regions. To account for these three dimensional flow phenomena, one has to apply corrections.

Tip/Hub loss correction The BEM does not account for vortices that being shed from the blade tip or the hub. These vortices have a significant influence on the induced velocities distribution in the rotor plane. To account for this effect, a correction factor F_{loss} is applied to the momentum part of the BEM equations, reformulating 2.43 and 2.42 as follows

$$dF_T = 4\pi r \rho U_\infty^2 (1-a)\, a F_{loss} dr \tag{3.1}$$

$$dQ = 4\pi r^3 \rho U_\infty \Omega (1-a) a' F_{loss} dr \tag{3.2}$$

$$F_{tip} = \frac{2}{\pi} \cos^{-1}\left[e^{-\left(\frac{B}{2}\frac{(r_{out}-r)}{r \sin\phi}\right)} \right] \tag{3.3}$$

$$F_{hub} = \frac{2}{\pi} \cos^{-1}\left[e^{-\left(\frac{B}{2}\frac{(r-r_{in})}{r_{in} \sin\phi}\right)} \right] \tag{3.4}$$

$$F_{loss} = F_{tip} F_{hub} \tag{3.5}$$

Turbulent wake state To account for effects when the turbine transitions into the turbulent wake state for induction factors of $a \geq 0.5$ a new thrust coefficient for this conditions is approximated as follows[4]

$$C_T = \frac{8}{9} + \left(4F - \frac{40}{9}\right) a + \left(-4F + \frac{50}{9}\right) a^2 \tag{3.6}$$

Or, solving for a gives

$$a = \frac{18F - 20 - 3\sqrt{C_T\,(50 - 36F) + 12F\,(-4 + 3F)}}{36F - 40} \tag{3.7}$$

Skewed wake There is also a correction for yaw misalignment implemented in AeroDyn. Yaw misalignment describes the situation when the wind is approaching the rotor plane at every angle but 90 degrees. To correct the induction factor following formula is used.

$$a_{skew} = a\left[1 + \frac{15\pi}{32}\frac{r}{r_{out}}\tan\frac{\chi}{2}\cos\psi\right] \tag{3.8}$$

The rotor wake angle χ is slightly larger than the rotor yaw angle γ and can be approximated with $\chi = (1 + 0.6a)\,\gamma$. Figure 3.4 sketches a rotor under yawed conditions. It can be seen that the yaw angle γ, the angle between the free stream velocity and the rotor axis, is slightly smaller than the wake skew angle χ, the angle between the overall wake motional direction and the rotor axis.

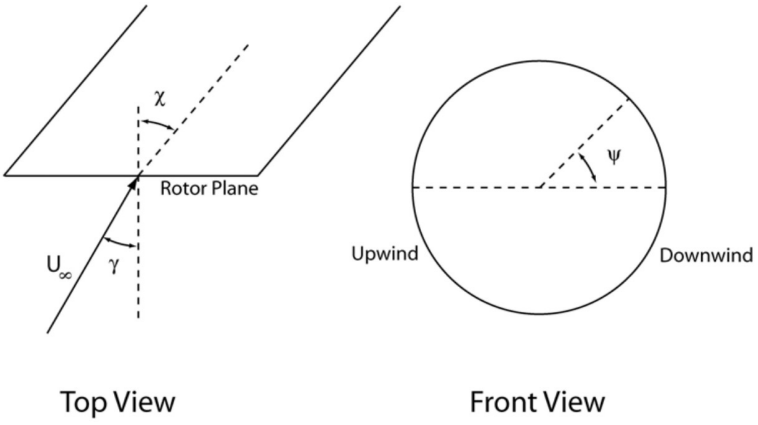

Figure 3.4.: Yaw misalignment coordinates [17]

BEM governing equations Before introducing the iterative process of the BEM the required equations for the thrust coefficient C_T and the induction factors a and a' are derived in this paragraph.

The thrust coefficient is straightforward from its formulation

$$C_T = \frac{F_T}{\frac{1}{2}\rho A_D U_\infty^2} = \frac{\frac{1}{2}\rho\left(\frac{U_\infty(1-a)}{\sin\phi}\right)^2 BcC_n dr}{\frac{1}{2}\rho 2\pi r dr U_\infty^2}$$

$$C_T = \frac{\sigma_B\,(1-a)^2\,C_n}{\sin^2\phi} \tag{3.9}$$

[4]The thrust coefficient of classic one dimensional wake state is $C_T = 4a\,(1-a)$.

$\sigma_B = \frac{Bc}{2\pi r}$ is a local solidity factor.
An expression for a can be derived when equating equations 3.1 and 2.51 in dF_T.

$$dF_T = 4\pi r\rho U_\infty^2 (1-a)\, aF_{loss}dr = \frac{1}{2}\rho \left(\frac{U_\infty (1-a)}{\sin\phi}\right)^2 BcC_n dr$$

$$a = \left[1 + \frac{4F_{loss}\sin^2\phi}{\sigma_B C_n}\right]^{-1} \tag{3.10}$$

In the same way equations 3.2 and 2.52 are equated.

$$dQ = 4\pi r^3 \rho U_\infty \Omega (1-a) a' F_{loss} dr = dQ = \frac{1}{2}\rho \left(\frac{U_\infty (1-a)}{\sin\phi}\right)\left(\frac{r\Omega (1-a')}{\cos\phi}\right) BcrC_t dr$$

$$a' = \left[-1 + \frac{4F_{loss}\sin\phi\cos\phi}{\sigma_B C_t}\right] \tag{3.11}$$

BEM iteration regime

1. Initialize a and a':
   As an initialization the axial induction factor gets estimated with equation 2.48 and 3.10, assuming small inflow angles ($\sin\phi \approx \phi$, $\cos\phi \approx 1$), $a' = 0$, $F_{loss} = 1$, $C_d = 0$, $C_l = 2\pi\alpha$ and $\alpha = \phi - \beta$.

   $$a = \frac{1}{4}\left[2 + \pi\lambda_r\sigma - \sqrt{4 - 4\pi\lambda_r\sigma_B + \pi\lambda_r^2\sigma_B(8\beta + \pi\sigma_B)}\right]$$

   $$a' = 0$$

2. Compute the inflow angle ϕ using equation 2.48.
3. Compute the thrust coefficient C_T using equation 3.9.
4. Calculate tip- and hub-loss correction factors with equation 3.5.
5. Check if $C_T > 0.96F$.
   If yes, then calculate a with equation 3.7.
   If not, then go to the next step.
6. Compute the local angle of attack using equation 2.53.
7. Read off C_L and C_D from a polar table.
8. Calculate a and a' from equations 3.10 and 3.11.
9. If a and a' has changed more than a certain tolerance, go to step (2) or else finish.[5]
10. Compute the local forces on the segment of the blades.

[5] The tolerance level used in AeroDyn is $\Delta a \leq 0.005$ but is adjustable by an input file.

3.3.2. Generalized dynamic wake model

The second available wake modeling approach in AeroDyn is the *generalized dynamic wake* model (GDW) . According to the AeroDyn theory manual [17] the basic governing equations of the generalized dynamic wake model are derived from the *Euler equations*. Assuming that the induced velocities are small perturbations relative to the free stream inflow, the conservation of momentum simplifies to

$$\frac{\partial u}{\partial t} + U_\infty \frac{\partial u}{\partial x} = -\frac{1}{\rho}\frac{\partial p}{\partial x} \tag{3.12}$$

$$\frac{\partial v}{\partial t} + U_\infty \frac{\partial v}{\partial x} = -\frac{1}{\rho}\frac{\partial p}{\partial y} \tag{3.13}$$

$$\frac{\partial w}{\partial t} + U_\infty \frac{\partial w}{\partial x} = -\frac{1}{\rho}\frac{\partial p}{\partial z} \tag{3.14}$$

With the conservation of mass

$$\frac{\partial u}{\partial x} + \frac{\partial v}{\partial y} + \frac{\partial w}{\partial z} = 0 \tag{3.15}$$

one finally gets the Laplace equation for the pressure distribution:

$$\nabla^2 p = 0 \tag{3.16}$$

The pressure loading on the rotor blades forms the boundary conditions for the governing equations [35]. A more detailed description of the GDW model is provided in [17, 35, 8].

The main advantage of the GDW method over the BEM is an enhanced modeling of the dynamic wake effects and that tip- and hub-losses as well as yaw misalignment effects are already included and no additional correction models are needed.

In the present thesis, the GDW model is used to calculate the induced velocity distribution over the rotor disc. These induced velocities are then used to determine the angle of attack for each element and the aerodynamic force is calculated using airfoil polar tables.

Several drawbacks also arise for the GDW [17].

- Instabilities for low wind speeds because of the assumption $U_\infty \gg u_i$. The GDW switches to BEM when the mean free stream wind speed reaches values lower than $8^m/_s$.
- Wake rotation not considered. To account for this effect the tangential induction factor is calculated with the BEM equation.
- Flat rotor disk assumption corrupted by large blade deflections or significant blade coning. This leads to imprecise GDW aerodynamics.

3.4. Semi-empirical Aeroacoustic Formulation

As mentioned in Section 3.1 the aeroacoustic subroutine in FAST is based on semi-empirical aeroacoustic formulations. These equations rest upon acoustic measurements of an airfoil in an anechoic wind tunnel under either non-turbulent [23] or turbulent [6] inflow conditions.

Five independent noise source mechanism of an airfoil in a non-turbulent stream where identified in [23], which are related to as *airfoil self-noise*. The exact semi-empirical formulations of this equations can be reviewed in [23] or [24].

The semi-empirical formulation for noise generated by an airfoil in a turbulent stream was derived by Lowson [22] and is based on Amiet's [6] work. The exact formulation can be found in [22] or [24].

The total emitted noise spectra, at a far field observer position in one-third octave bands, is calculated according to equation 3.17. SPL_i^S are the five airfoil self-noise mechanisms and SPL^T adds to the total emitted noise spectra under turbulent inflow conditions.

$$TOTAL = 10\log_{10}\left[\left(\sum_{i=1}^{5} 10^{0.1SPL_i^S}\right) + 10^{0.1SPL^T}\right] \tag{3.17}$$

3.4.1. Airfoil self-noise

The proposed semi-empirical formulas for the different self noise mechanisms are all of similar form only differing in various scaling laws applied [18]. Figure 3.5 gives a schematic overview over the five described self-noise mechanisms of an airfoil in [23].

- Turbulent boundary layer trailing edge noise (TBLTEp/s)
- Separation stall noise (TBLTEα)
- Laminar boundary layer vortex shedding noise (LBLVS)
- Trailing edge bluntness vortex shedding noise (TEBVS)
- Tip vortex formation noise (TIPVF)

Turbulent boundary layer trailing edge noise The major contributer to airfoil self-noise is the interaction of the turbulent boundary layer of the pressure and the suction side with the trailing edge of the airfoil. Along the chord the boundary layer transitions from laminar to turbulent. Small turbulent eddies then convect past the trailing edge generating fluctuating pressures on either side of the airfoil, scattering broadband sound at the edge. Since the boundary layer displacement thickness on the suction side δ_s^* is usually larger than on the pressure side δ_p^*, the noise produced by the suction side boundary layer usually has higher levels and lower frequencies than noise generated on the pressure side [28].

Separation stall noise The turbulent boundary layer on the suction side of an airfoil increases with an increasing angle of attack. At high angles of attack the flow separates from the suction side of the airfoil - the airfoil is stalling - and the recurring formation of relatively large-scale unsteady structures cause low frequency noise. For mild angles of attack, noise is emitted near the trailing edge, whereas at deep stall conditions sound is radiated from the

entire chord. This noise source is closely related to trailing edge noise and it is an important noise source for wind turbines because the blades encounter high angles of attack for a significant portion of time.

Laminar boundary layer vortex shedding noise For small chord lengths and/or low flow speeds the turbulence in the boundary layer might not be fully developed at the trailing edge. When the turbulence level in the boundary layer at the trailing edge is low, mild turbulent edge scatter causes acoustic wavefronts that travel upstream triggering instabilities (Tollmien-Schlichting waves) in the laminar upstream boundary layer. These instabilities grow downstream and are shed at the trailing edge. This mechanism leads to a concurrent amplifying feedback loop as acoustic waves caused by the shed vortices again trigger instabilities in the upstream laminar boundary layer resulting again in a wave formation. The vortex formation occurs at a discrete frequency resulting in tonal noise.

For big modern wind turbines LBLVS noise only plays a minor role, but may be important for smaller sized wind turbines (<500kW), since chord lengths are rather massive and flow speeds in the tip region, where most noise is produced, are fairly large. Hence, the boundary layer at the trailing edge is fully turbulent.

Trailing edge bluntness vortex shedding noise Vortex shedding can be also occur due to a blunt trailing edge even when the boundary layer is fully turbulent at the trailing edge. This results in tonal peaks in the noise spectrum. The frequency and amplitude of this peaks are largely dependent on the geometry of the trailing edge. Therefore, it is vital for the trailing edge to be well-manufactured and sufficiently slim to limit noise emissions due to TEBVS.

The frequency occurrence of this noise mechanism can be estimated with the Strouhal number St, which puts the vortex shedding frequency at the trailing edge in relation to the inflow velocity. f_{St} is the vortex shedding frequency, d_{TE} is the bluntness of the trailing edge and U_{St} is the inflow velocity. The Strouhal number can be approximated with $0.2 < St < 0.3$ for considered flows speeds around a wind turbine blade.

$$St = \frac{f_{St} \cdot d_{TE}}{U_{St}} \tag{3.18}$$

Tip vortex formation noise Another noise source is related to the tip vortex formation. As described in theory Section 2.1.4 the loading on a wing can be approximated with a distribution of circulations. As a consequence a vortex system develops behind a wing of finite length. The interaction of the vortices with the blade tip and the trailing edge is also a source of aerodynamic noise. The sound pressure level of tip noise is generally low for wind turbines, at pronounced frequencies in the mid to higher frequency range.

Tip noise was a problem with older squared and thick blade tips but is, the same as TEBVS noise, controlled presently through progressively advanced blade design.

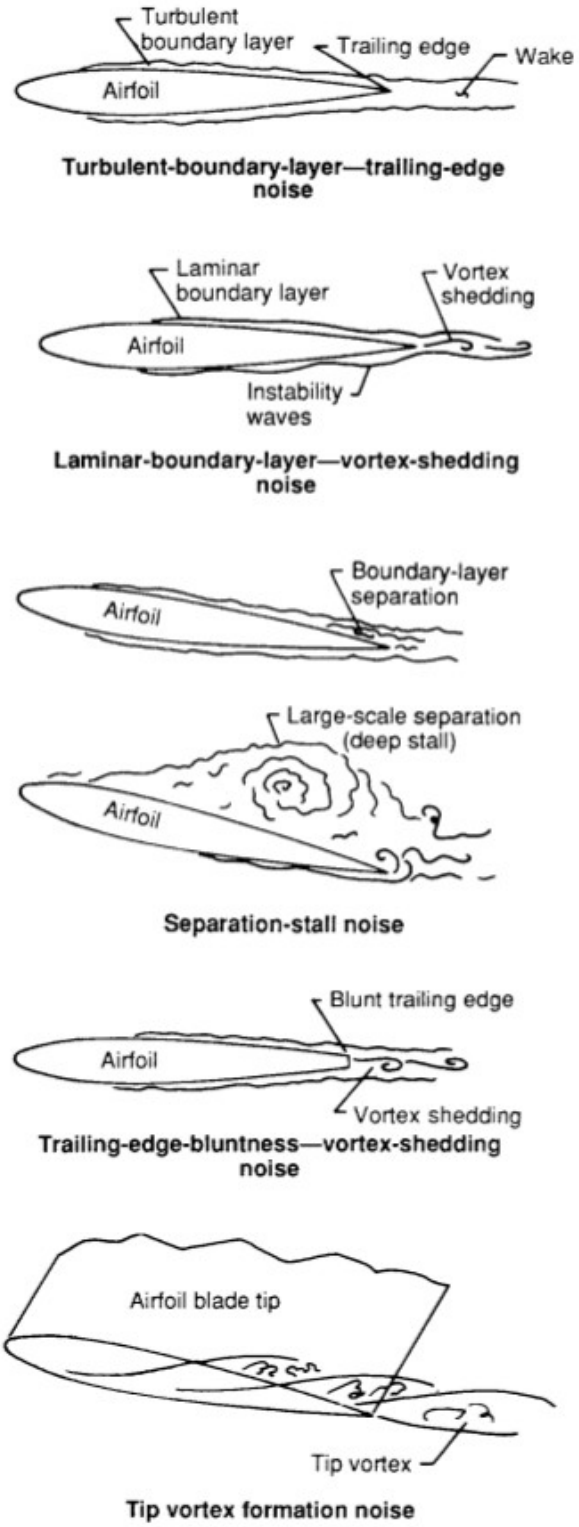

Figure 3.5.: Schematic of airfoil self-noise mechanism [23]

3.4.2. Turbulent inflow noise

For wind-turbine applications, the interaction of incoming turbulence (produced by the atmospheric boundary layer) with the leading edge of the turbine blades is a significant noise source, particularly at low frequencies [24].

Large incoming eddies cause a fluctuating force on the complete blade while small imping-

ing eddies do not affect the global aerodynamic force. The emitted frequency depends on the size of the incoming turbulent eddies (turbulent length scales Λ) and is characterized by how many eddies impinge on the airfoil per second. This disturbance occurs at a frequency of $f \sim \frac{U_\infty}{\Lambda}$ [28].

Natural atmospheric turbulence is expected to cause broadband noise for frequencies up to 1kHz, but it is still an open issue as to what extent turbulent inflow noise contributes to the overall sound pressure level [27, 28].

In FAST an empirical relation formulated by Lowson [22] is used to model the low and high frequency behavior of turbulent inflow noise. The sound intensity (the mean square sound pressure), in this empirical formulation, is directly proportional to the turbulent length scale and the turbulence intensity of the incoming flow. The exact formulation of this equation is reviewed in [24, 22].

FAST uses the isotropic turbulence integral-scale parameter of the atmospheric boundary layer as specified in the IEC standard 61400-1 [1]. It is 2.45 times the hub hight up to a maximum of 73.5m. This parameter should be chosen with care because it is sensitive to the wind turbine's rotor size and site specific atmospheric inflow conditions [24]. The turbulent length scale is adjusted to a value 0.4 times the IEC specified length in this thesis, as the results obtained with this value better agree with the reference data.

3.4.3. Directivity characteristic

Aeroacoustic noise has a directivity characteristic. In order to account for the frequency depended radiation pattern, the predicted sound pressure levels of the semi-empirical formulas are corrected with analytical directivity functions. The directivity functions also account for convective amplification [24].

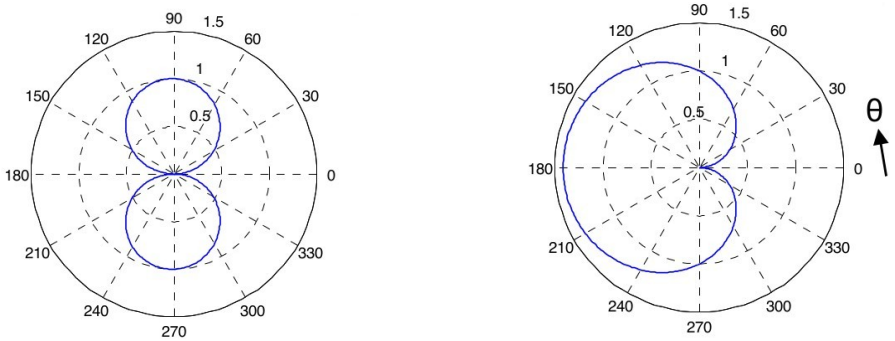

(a) (b)

Figure 3.6.: (a) Low- and (b) high- frequency directivity pattern [27]

For high frequency noise emissions (TBLTEp/s, LBLVS, TEBVS, TIPVF) the radiation pattern in the plane is given by $\sin^2\left(\frac{\Theta}{2}\right)$, for low frequency noise emissions (TBLTEα, TURBIN) by $\sin^2(\Theta)$ [24, 27]. From Figure 3.6 it can be seen that for low frequency highest noise levels are radiated in the direction perpendicular to the rotor plane while highest levels for high frequency sound is radiated in direction of motion of the blade. In fact the overall

radiation pattern, depending on the different emitted frequencies, looks more like in Figure 3.7, a combination of high frequency and low frequency directivity pattern.

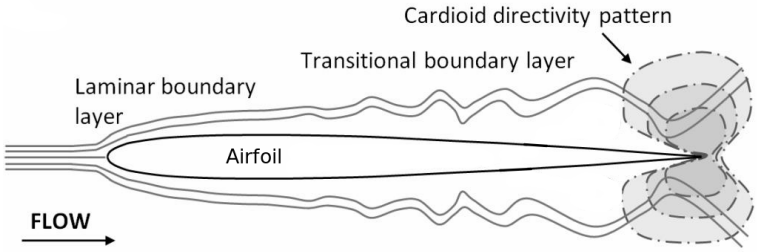

Figure 3.7.: Schematic of airfoil directivity pattern for low to moderate Reynolds numbers and zero angle of attack [7]

3.5. Analytical Aeroacoustic Formulation

As mentioned in Section 3.1 the noise output from FAST, based on semi-empirical aeroacoustic formulations, is compared to an analytical aeroacoustic approach based on the Ffowcs-Williams and Hawkings equation.

Farassat derived an integral formulation of the Ffowcs-Williams and Hawkings equation based on free field Green's functions and neglecting the quadrupole source term [12]. The *Farassat formulation 1A* is widely used in rotor noise prediction nowadays [13]. The source code for the Farassat formulation 1A is taken from the OpenFOAM project.

The acoustic pressure at an far field observer position is given by equation 3.19 [13]. p'_T denotes the thickness noise and p'_L the loading noise terms.

$$p'(\boldsymbol{x},t) = p'_T(\boldsymbol{x},t) + p'_L(\boldsymbol{x},t) \tag{3.19}$$

$$\begin{aligned} 4\pi p'_T(\boldsymbol{x},t) = &\int_{f_H=0} \left[\frac{\dot{q}_\rho}{r_S\left|1-M_r\right|^2}\right]_\tau dS + \\ &+ \int_{f_H=0} \left[\frac{q_\rho\left(r\dot{M}_r + c_0 M_r - c_0 M_S^2\right)}{r_S^2\left|1-M_r\right|^3}\right]_\tau dS \end{aligned} \tag{3.20}$$

$$\begin{aligned} 4\pi p'_L(\boldsymbol{x},t) = &\frac{1}{c_0}\int_{f_H=0} \left[\frac{\dot{l}_r}{r_S\left|1-M_r\right|^2}\right]_\tau dS + \\ &+ \int_{f_H=0} \left[\frac{l_r - l_M}{r_S^2\left|1-M_r\right|^2}\right]_\tau dS + \end{aligned} \tag{3.21}$$

$$+ \frac{1}{c_0}\int_{f_H=0} \left[\frac{l_r\left(r\dot{M}_r + c_0 M_r - c_0 M_S^2\right)}{r_S^2\left|1-M_r\right|^3}\right]_\tau dS \tag{3.22}$$

The loading terms l_i in the classic interpretation of the Farassat formulation 1A enter as a pressure fluctuation times a unit normal vector $p'\hat{\boldsymbol{n}}_H$ on a surface element dS, when neglecting viscous stresses as a source of sound. However, for some technical applications, when it is not convenient or not possible to simulate a full chordwise pressure load distribution of an entire blade, a *compact chordwise loading* can be used instead. This means that for every blade section, the otherwise chordwise pressure distribution collapses in a point load placed along the span of the blade. This is well suited for low frequency noise prediction and can predict noise within a few decibels [26, 9].

The thickness noise terms q_ρ enter as the fluid density times the dot product of the surface velocity with the normal vector on the surface $\rho(\boldsymbol{v}_H \cdot \boldsymbol{n}_H)$ and are neglected in this thesis.

The loading noise terms, as used in this thesis, are

$$\boldsymbol{M}_S = \frac{\boldsymbol{v}_H}{c_0} \tag{3.23}$$

$$M_S = |\boldsymbol{M}_S| \tag{3.24}$$

$$M_r = \boldsymbol{M}_S \cdot \hat{\boldsymbol{r}}_S \tag{3.25}$$

$$l_r = -\left(\boldsymbol{F}'_{AD}\right) \cdot \hat{\boldsymbol{r}}_S \qquad [\mathrm{N/m}] \tag{3.26}$$

$$l_M = -\left(\boldsymbol{F}'_{AD}\right) \cdot \boldsymbol{M}_S \qquad [\mathrm{N/m}] \tag{3.27}$$

$\boldsymbol{M}_S$ is the Mach number vector of the source (blade) motion. $\boldsymbol{v}_H$ is the source surface velocity vector. $\hat{\boldsymbol{r}}_S$ is the unit radiation vector $\hat{\boldsymbol{r}}_S = \frac{\boldsymbol{x}-\boldsymbol{y}}{r_S}$. $\boldsymbol{F}'_{AD}$ is the fluctuation of the aerodynamic force vector per unit span. All vectors are in tower base coordinates. Furthermore, the integration variable dS needs to be substituted with dr.

4. Results and Discussion

This Chapter presets the results of the aeroacoustic analysis of the two investigated wind turbines. First reference data is given in Section 4.1. The resulting one-third octave plots of the two different noise prediction methods and a thorough analysis of the results are presented in Section 4.3.

4.1. Reference Data

All reference noise measurement data in this thesis refer to the downwind reference position 1 at a reference wind speed of 8m/s at 10m height, as specified by the IEC 61400-11 standard [3]. Thus, all calculated one-third octave sound spectra in Section 4.3 correspond to this reference settings as well.

The IEC 61400-11 standard is an international standard on the methodology of measuring noise emissions originating from a wind turbine. It defines the instrumentation used, measurement procedures and reporting [3]. In principal, a microphone is mounted on a reflecting board, placed on the ground at a reference position approximately $R_0 = H + \frac{D}{2}$ away from the tower centerline. H denotes the turbines hub hight and D the rotor diameter (see Figure 4.4). Figure 4.1 shows a photo of the microphone covered with a wind shield. The measured sound pressure levels are converted into the *apparent sound power level* of an imaginary point source in the rotor center that would radiate the same sound in the direction where the measurement is taken[3, 29].

Figure 4.1.: Microphone on the ground plate for wind turbine noise measurements according to IEC61400-11 [3]

For the small AOC 15/50 wind turbine, one-third octave reference noise measurement data for the reference position 1 is provided [2]. Note that the values from Table 4 on page 7 in [2] are shifted two units down in order to match the bar plot on page 16 in and to be qualitatively in line with the continuous spectrum on page 20 in with a significant peak at 500Hz.

For turbines in the range of 5MW and above no direct measurement data is available. However, in [29] noise measurement data of 48 wind turbines in the range of 1-3MW is merged in order to extrapolate an assumed A-weighted third octave spectra of wind turbines in the range of 5MW and above. Figures 4.2 and 4.3 indicate that the sound power level increases and that the frequency spectra shifts down towards lower frequencies with increasing turbine size. Thus, according to Figure 4.2, the estimated A-weighted sound power level of a wind turbine in the range of 5MW is approximately $L_{WA} \approx 109dB$.

The sound power level can be converted back into a sound pressure level at an observer position according to equation 4.1. $A_{atm} = \alpha_{atm} \cdot R_1$ and A_{gr} are corrections for attenuation due to atmospheric absorption and ground effects, respectively, where α_{atm} is the atmospheric attenuation coefficient. R_1 is the distance from the hub to the observer as shown in Figure 4.4.

$$SPL_A = L_{WA} - 20\,dB \cdot \log_{10}\left(\frac{R_1}{1\,m}\right) - 11\,dB - A_{atm} - A_{gr} \tag{4.1}$$

No attenuation effects are considered by the computer models so A_{atm} and A_{gr} are set to zero when calculating the reference 1/3 sound pressure spectrum at a observer position for the 5MW turbine.

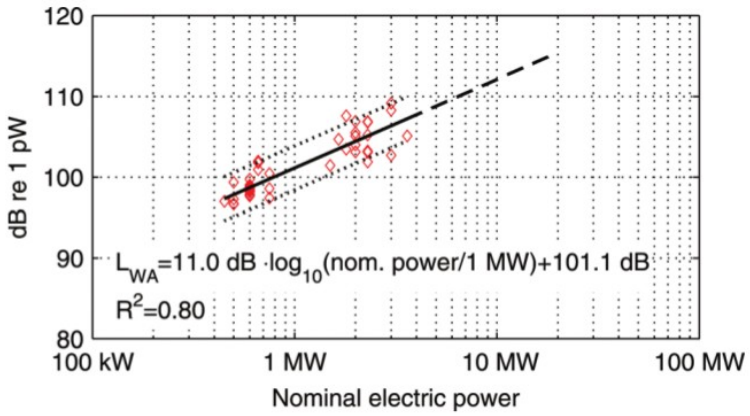

Figure 4.2.: Apparent sound power level L_{WA} as a function of turbine size. Wind speed 8m/s, measured 10m above ground. 90% confidence interval [29]

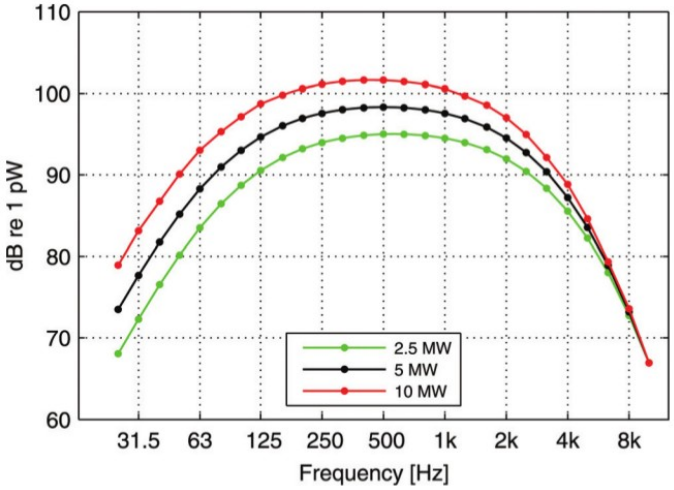

Figure 4.3.: Estimated A-weighted one-third octave sound power spectrum [29]

4.2. Reference Position

Figure 4.4 shows the reference measurement positions as specified in the IEC standard 61400-11 [3]. All plots in Sections 4.3 and 4.4 refer to observer positions 1. The additional results in Sections C.1 and C.2 refer to the observer positions 2-4 as well as in the rotor plane. Reference data is only available for observer position 1.

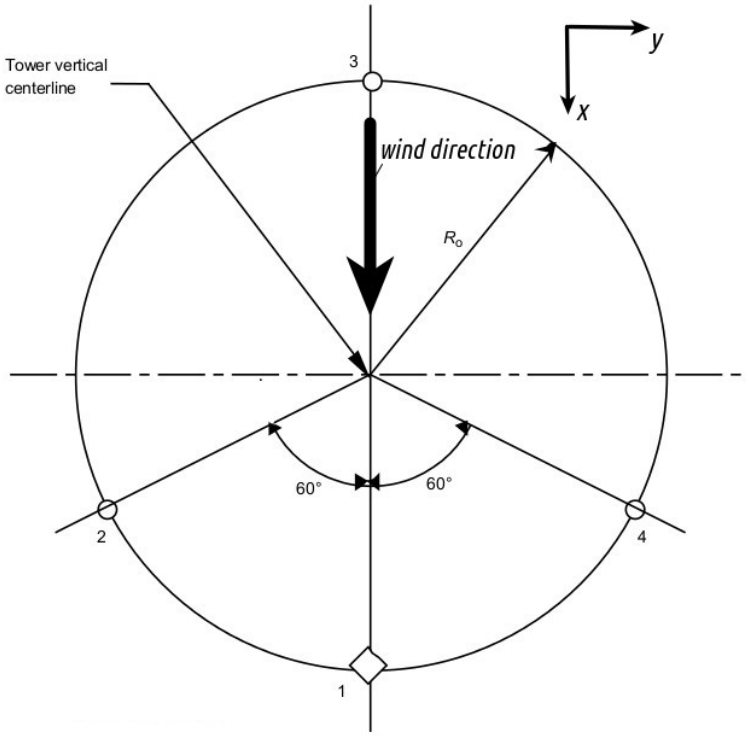

(a) Reference positions 1-4 on observer circle

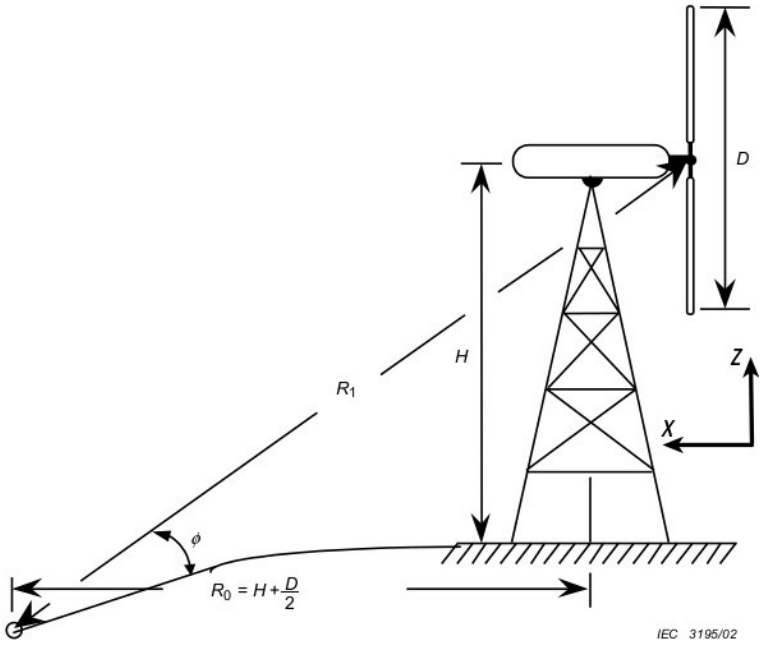

(b) Downwind reference position 1

Figure 4.4.: Observer reference position in tower base coordinate system [3]

4.3. Predicted Sound Spectra

This Section presents the predicted non-weighted and A-weighted one-third octave band spectra for the two investigated wind turbines at reference position 1, averaged over multiple revolutions. For all plots the reference wind speed is 8m/s at 10m height. The one-third octave spectrum plots contain the acoustic results of the semi-empirical aeroacoustic noise calculations done by FAST in comparison with the analytical aeroacoustic results of the FWH calculation with compact chordwise loading terms. The predicted FAST spectrum covers an audible range of 25Hz to 20kHz, whereas the predicted FWH spectrum only covers an audible range of 25Hz to 4kHz in the case of the AOC 15/50 turbine (Section 4.3.1), and up to 8kHz in the case of the NREL5M turbine (Section 4.3.2). All results are plotted against reference data.

The total sound pressure level of the semi-empirical calculation (TOTAL) is computed according to equation 3.17. The FWH spectrum curve is the result of a Fourier analysis of the pressure curve as calculated according to equation 3.19. The reference sound pressure is $p_{ref} = 2 \cdot 10^{-5} Pa$.

4.3.1. AOC 15/50

This Section presents the results for the small AOC 15/50 wind turbine. First the non-weighted audio spectra are analyzed in subsection 4.3.1.1 and then A-weighting is applied to the spectra in subsection 4.3.1.2. Each Section shows two plots. The first plot compares the predicted spectra with reference measurements [2]. The second plot shows the contribution of every semi-empirical noise mechanisms to the TOTAL predicted sound pressure level.

4.3.1.1. Non-weighted

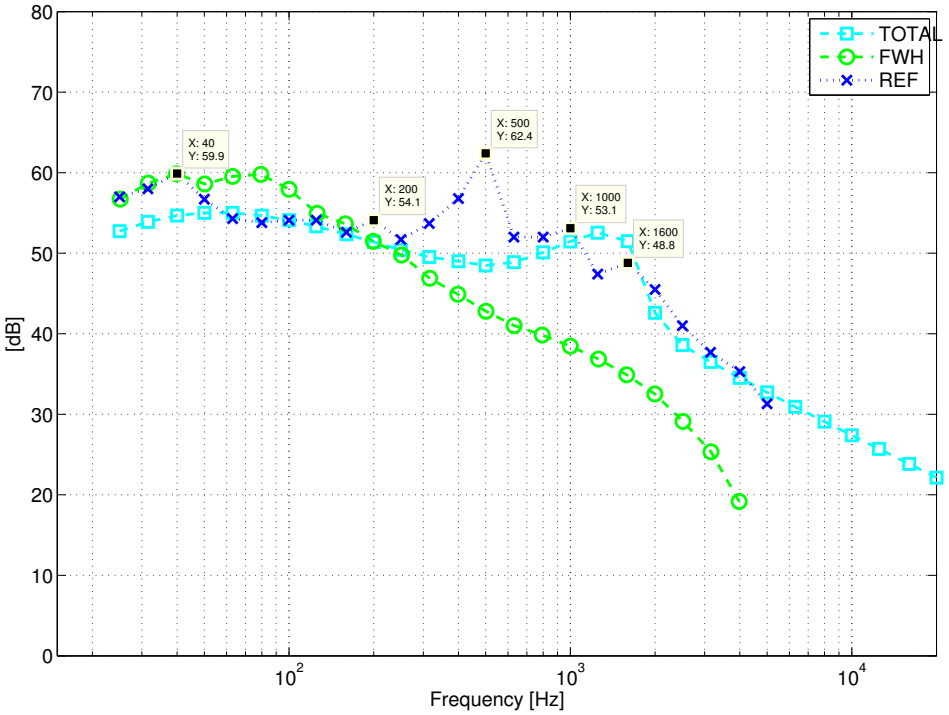

Figure 4.5.: Measured and predicted one-third octave spectra for the AOC 15/50 wind turbine at reference position 1. Wind speed 8m/s at 10m height. Turbulent length scale $\Lambda = 24.5m$. Turbulence intensity $I = 11.53\%$.

Figure 4.5 shows the non-weighted predicted spectra of the small AOC 15/50 wind turbine against reference measurement data [2]. The measured spectrum shows 5 peaks at 40Hz (59.9dB), 200Hz (54.1dB), 500Hz (62.4dB), 1kHz (53.1dB) and 1.6kHz (48.8dB). The 500Hz peak is believed to be gearbox noise [24] and is therefore not represented of any aeroacoustic model. The overall sound pressure level[1] of the reference measurement data is 68.7dB. The blade passing frequency of the AOC 15/50 wind turbine is $BPF = \frac{RPM}{60} \cdot B = \frac{64}{60} \cdot 3 = 3.2Hz$, hence it is not represented in the graph.

The predicted TOTAL sound pressure level of the semi-empirical model shows good agreement with the measurement results throughout the spectrum, except the tonal peak at 500Hz (gearbox noise) and the lowest frequencies below 50Hz. The solution of FAST and the FWH model predict diverse levels throughout the spectrum. However, the FWH model exactly predicts the lowest frequencies up to 50Hz but over predicts measured levels between 50 and 125Hz and significantly under predicts them for frequencies above 200Hz. The OASPL of the FAST and the FWH prediction in Figure 4.5 are 65.4dB and 67.7dB respectively.

[1] The overall sound pressure level $OASPL$ is the integrated sound spectrum.

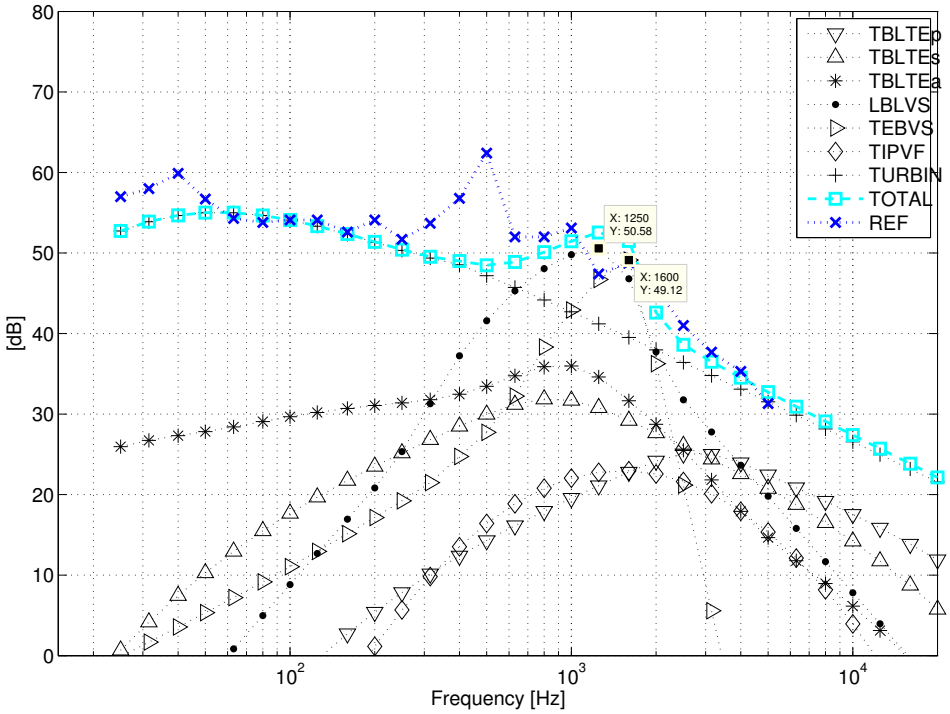

Figure 4.6.: Measured and self-noise one-third octave spectra for the AOC 15/50 wind turbine at reference position 1. Wind speed 8m/s at 10m height. Turbulent length scale $\Lambda = 24.5m$. Turbulence intensity $I = 11.53\%$.

Figure 4.6 shows the contribution of every semi-empirical noise mechanism to the TOTAL sound pressure level concerning the non-weighted spectrum. The turbulent length scale of the TURBIN model is $\Lambda = 24.5m$ which is about the hub height from Table 3.3. The turbulence level is $I = 11.53\%$. The hub height mean wind speed is 8.52m/s.

It can be seen that broadband turbulent inflow noise is the dominant aeroacoustic noise mechanism for the small AOC 15/50 wind turbine throughout the non-weighted spectrum except tonal vortex shedding noise in the range of 1-2kHz. The latter two peaks in the measured spectrum are well predicted by the semi-empirical model. They occur in the same frequency range where the semi-empirical model predicts laminar boundary layer and trailing edge bluntness vortex shedding noise (see the doted line (LBLVS) and the line with the backwards orientated triangles (TEBVS) in Figure 4.6). The peak frequencies of TEBVS and LBLVS noise are 1.6kHz and 1.25kHz at levels of 50.6dB and 49.1dB respectively. The predicted TEBVS frequency roughly coincides with the anticipated vortex shedding frequency due to an estimate with an assumed Strouhal number of $St = 0.22$ and assumed flow speeds of around $U_{St} \approx 45$m/s. The anticipated vortex shedding frequency with the average trailing edge bluntness of the AOC 15/50 turbine blade from Table 3.3 is $f_{St} = \frac{0.22 \cdot 45}{0.006} = 1.65kHz$.

The remaining semi-empirical noise mechanisms are of minor importance for the small wind turbine. However, the characteristic of trailing edge noise, even if not pronounced, with enhanced suction side levels in the lower frequency range and lower pressure side levels in the higher frequency range [28], is evident. The peak frequency level of TBLTEs noise is 5dB higher than the peak frequency level of TBLTEp noise. The peak frequency of separation stall noise (TBLTEα) coincides with the peak frequency of TBLTEs noise (800Hz) with a

4dB higher level (36dB). The peak frequency of TBLTEp noise is 2.5kHz. High frequency tip noise (TIPVF) shows the lowest peak sound pressure level of 23dB at 1.6kHz for the small turbine.

Generally turbulent inflow noise dominates the whole spectrum of the small turbine. It is 30dB louder than the second loudest self-noise mechanism (TBLTEα) in the lower frequency range (TBLTEα) and 10-15dB louder than second loudest self-noise mechanism in the higher frequency range (TBLTEp).

4.3.1.2. A-weighted

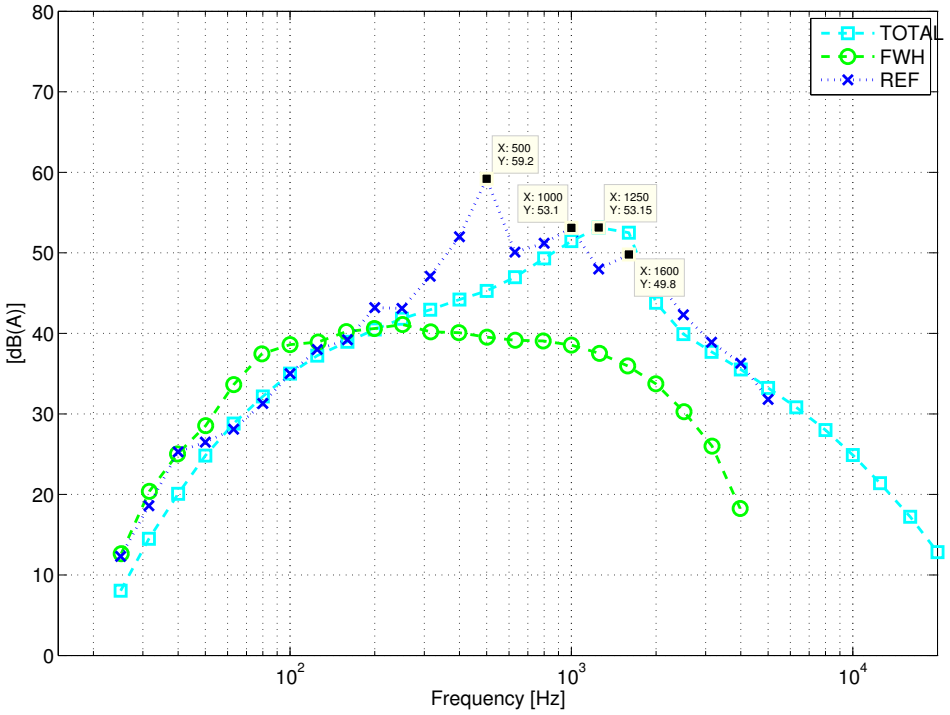

Figure 4.7.: A-weighted measured and predicted and one-third octave spectra for the AOC 15/50 wind turbine at reference position 1. Wind speed 8m/s at 10m height. Turbulent length scale $\Lambda = 24.5m$. Turbulence intensity $I = 11.53\%$.

Figure 4.7 shows the A-weighted audio spectrum of the AOC turbine. The peak at 500Hz of the reference measurement still shows the highest level (59.2dB(A)). Due to audio weighting the latter two peaks in the spectrum, that are related to LBL- and TEBVS noise (see previous Section), become more important, with levels of 53.1dB(A) for the 1kHz and 49.8dB(A) for the 1.6kHz peak. The overall A-weighted sound pressure level of the reference measurement in Figure 4.7 is 62.5dB(A). The A-weighted predicted peak sound pressure level of the semi-empirical model is 53.2dB(A) at frequency of 1250Hz. The A-weighted predicted peak sound pressure level of the FWH model is around 40dB(A). The predicted A-weighted OASPLs are 59.2dB(A) and 51dB(A) for FAST and FWH respectively.

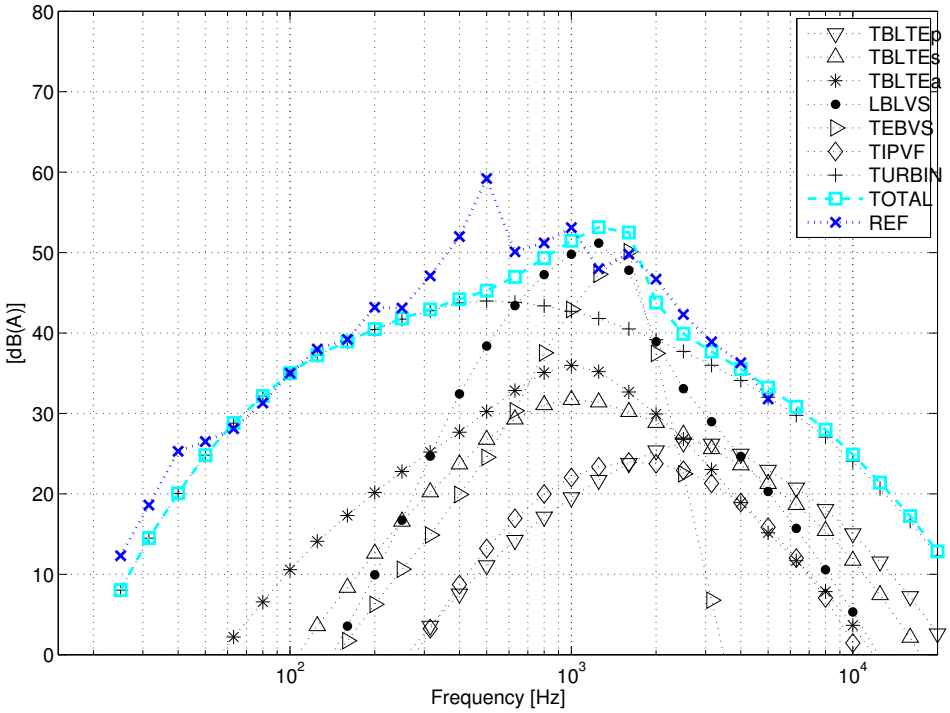

Figure 4.8.: A-weighted measured and self-noise one-third octave spectra for the AOC 15/50 wind turbine at reference position 1. Wind speed 8m/s at 10m height. Turbulent length scale $\Lambda = 24.5m$. Turbulence intensity $I = 11.53\%$.

Figure 4.8 shows the contribution of every single semi-empirical noise mechanism to the predicted A-weighted TOTAL sound pressure level. In Figure 4.8 it can be seen that the airfoil self-noise mechanisms gain importance w.r.t the A-weighted audio spectrum but are still dominated by the broadband turbulent inflow noise mechanism throughout the spectrum. Peak frequencies and levels of the single noise mechanisms do not change significantly compared to the non-weighted spectrum in Figure 4.6.

4.3.1.3. Variation of Λ

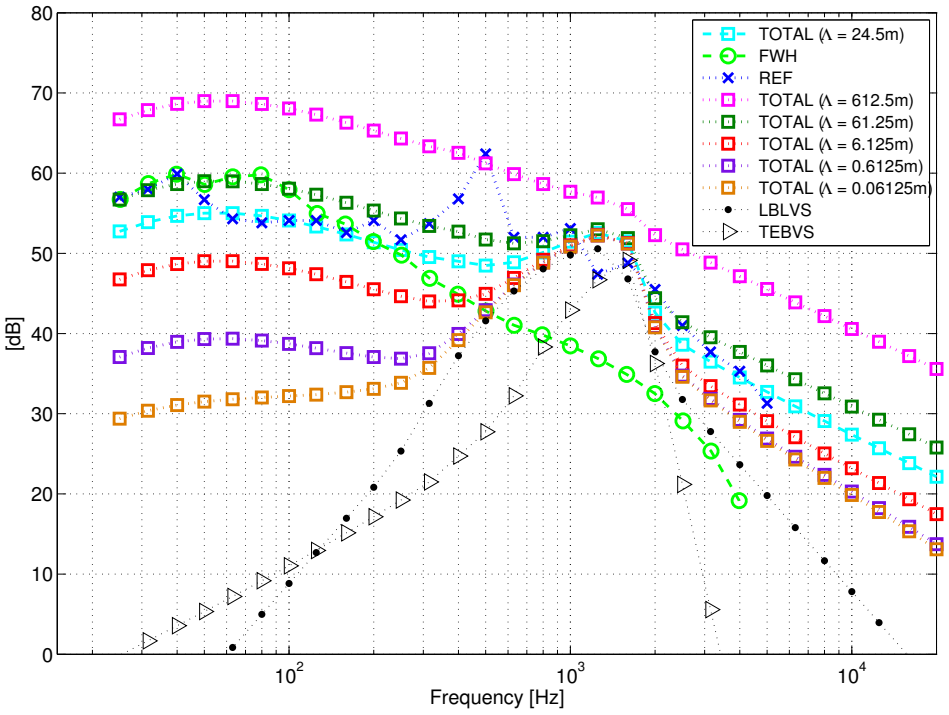

Figure 4.9.: Effect of inflow turbulence length scale on TOTAL sound pressure level prediction for the AOC 15/50 wind turbine. Wind speed 8m/s at 10m height. Turbulence intensity $I = 11.53\%$.

As mentioned in Section 3.4.2 the turbulent length scale is a sensitive parameter for turbulent inflow noise (TURBIN) prediction. It depends on the rotor size and site specific turbulence characteristic and should be chosen with care [24]. Figure 4.9 shows the dependence of the TOTAL predicted sound pressure level on this parameter for the non-weighted spectrum. Note, only the TURBIN noise mechanism changes with Λ, the remaining self-noise mechanisms are independent of this parameter. The smaller Λ is, the more pronounced are the tonal vortex shedding components in the spectrum in Figure 4.9. For a very large Λ almost no tonal peak can be observed in the predicted spectrum anymore.

The turbulent length scale Λ in this plot varies over several orders of magnitude from some hundred meters (612.5m) to some centimeters (0.06125m). Best agreement with the reference data throughout the spectrum is given for a length scale of 24.5m, which is about the hub height of the AOC 15/50 wind turbine from Table 3.3. This value is 0.4 times the proposed value for the IEC specified length scale in [1]. However, the lowest frequencies up to 50Hz are best predicted with the larger IEC length scale of 61.25m. Interestingly the FWH model exactly predicts the lowest frequencies of the reference measurements as well as the FAST model for a turbulent length scale of 61.25m. The predicted curves then show significant diverse results for frequencies above 200Hz.

4.3.2. NREL5M

In this Section the results of the large NREL5M wind turbine are discussed. First the non-weighted audio spectra are analyzed in subsection 4.3.2.1 and then A-weighting is applied to the spectra in subsection 4.3.2.2. Each subsection shows two plots. The first plot compares the predicted spectra with estimated reference data in [29]. The second plot shows again the breakdown of the TOTAL predicted sound pressure level of the semi-empirical model into its independently contributing noise mechanisms.

4.3.2.1. Non-weighted

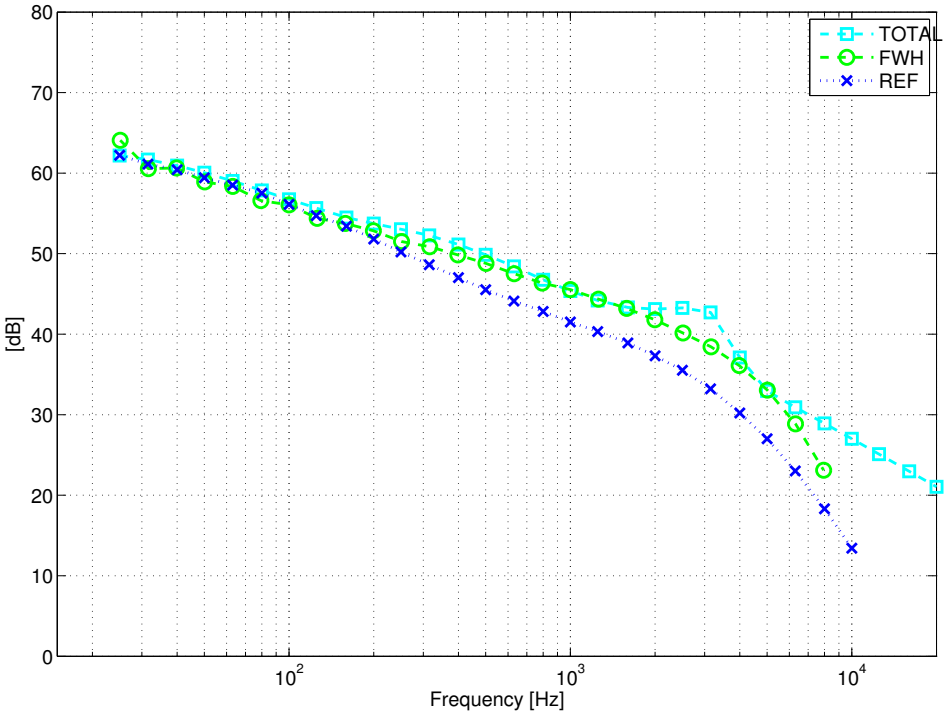

Figure 4.10.: Estimated and predicted one-third octave spectra for the NREL5M wind turbine at reference position 1. Wind speed 8m/s at 10m height. Turbulent length scale $\Lambda = 29.4m$. Turbulence intensity $I = 8.75\%$.

Since the reference data for the NREL5M wind turbine is a statistically based extrapolation of noise measurement data of 48 wind turbines in the rage of 1-3MW [29], care should be taken in interpreting the results. Furthermore, by virtue of the inherent statistical characteristic of that data, it does not represent any tonal events in the spectrum. No direct reference measurement for the NREL5M wind turbine is available since this turbine is only a virtual prototype at present. The overall sound pressure level of the reference spectrum in Figure 4.10 is 68.8dB.

However, the most striking feature of the plot in Figure 4.10 is that the predicted sound pressure level of the FWH model, with compact chordwise loading terms, agrees well with the prediction of the semi-empirical model throughout the spectrum. Both of them exactly predict the lowest frequencies of the estimated spectrum up to 200Hz and both models agree in predicting higher level, compared to the reference data, for frequencies above 200Hz. However,

the predicted tonal component in the FAST spectrum around 3.15kHz is not reproduced by the FWH model as well as the FWH prediction disagrees with FAST for 8kHz.

The highest levels in this spectrum are predicted for the lowest frequency. The FWH model predicts a peak level of 64.1dB at 25Hz while the reference data and the FAST prediction show peak levels of 62.2dB. The overall predicted sound pressure levels are 68.9dB for FAST and 69.3dB for the FWH prediction.

The blade passing frequency of the NREL5M wind turbine is not represented in the spectrum in Figure 4.10 $\left(BPF = \frac{RPM}{60} \cdot B = \frac{12.1 \cdot 3}{60} = 0.605Hz\right)$.

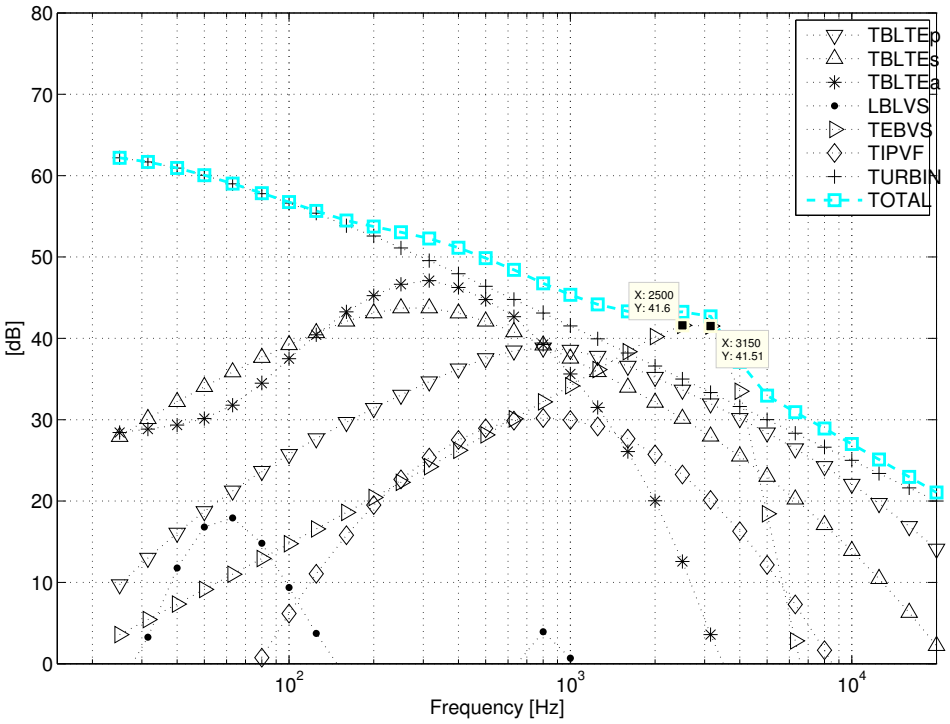

Figure 4.11.: Estimated and self-noise one-third octave spectra for the NREL5M wind turbine at reference position 1. Wind speed 8m/s at 10m height. Turbulent length scale $\Lambda = 29.4m$. Turbulence intensity $I = 8.75\%$.

Figure 4.11 shows again the breakdown of the TOTAL predicted sound pressure level of the semi-empirical model into the contribution of every noise mechanism throughout the spectrum. The turbulent length scale of the TURBIN model is $\Lambda = 29.4m$ which is about one-third of the turbines hub height from Table 3.3. The turbulence level is $I = 8.75\%$. The hub height mean wind speed is 11.49m/s.

It can be seen that broadband turbulent inflow noise is an important - but not the dominant - aeroacoustic noise mechanism for the large NREL5M wind turbine throughout the non-weighted spectrum. The contribution of the remaining semi-empirical airfoil self-noise mechanisms to the TOTAL predicted sound pressure level spectrum of the large NREL5M wind turbine are much more pronounced than of the several orders of magnitude smaller AOC 15/50 wind turbine. This contribution is most significant for frequencies above 200Hz where the level difference between turbulent inflow noise and airfoil self noise mechanisms reaches values less than 3dB.

The major self-noise contributer is TBLTE noise. Again, the high level low frequency suction side, and low level high frequency pressure side characteristic of TBLTE noise [28] is evident. The peak frequency level of TBLTEs noise is again 5dB higher than the peak frequency level of TBLTEp noise. The peak frequency of TBLTEα noise (315Hz) roughly coincides with the peak frequency level of TBLTEs noise (250Hz). The level difference between the noise contributer of the suction side, TBLTEs (peak level 43.7dB) and TBLTEα (peak level 47.1dB), is 3.4dB. The peak frequency of TBLTEp noise is 800Hz. High frequency tip noise (TIPVF) shows the lowest peak sound pressure level of 30.2dB at 800Hz.

Tonal TEBVS noise occurs at around 2-3kHz. The predicted TEBVS peak level is 41.6dB at a peak frequency of 3.15kHz. For the large wind turbine an estimation of the TEBVS peak frequency with an assumed Strouhal number of $St = 0.3$ delivers a frequency much larger than predicted peak TEBVS frequency. With an assumed flow speeds of $U_{St} \approx 75^{\mathrm{m}}/_{\mathrm{s}}$ the vortex shedding frequency with an average trailing edge bluntness of 0.002m is $f_{St} = \frac{0.3 \cdot 80}{0.002} = 11.25kHz$. Morover, it should be noted, that no geometrical data of the blunt trailing edge of the NREL5MW wind turbine concept study was available and default values for trailing edge bluntness from Table 3.3 are used instead. So, no reliable assertion about the peak TEBVS frequency can be made as well as the peak frequency and level in Figure 4.11 above might not represent the real bluntness noise frequency and amplitude of the investigated wind turbine. Further research with actual geometrical trailing edge data of the large turbine blade is necessary.

Furthermore, as one would expect for big multi-Megawatt wind turbines, laminar boundary layer vortex shedding noise is of no relevance. A mild spectral peak of LBLVS noise can be observed at 63Hz with 17.9dB and an even smaller one at 800Hz with only 3.9dB. The transition of the boundary layer on either side of the turbine blade from laminar to turbulent happens well before the flow reaches the trailing edge when considering an average chord length of several meters.

4.3.2.2. A-weighted

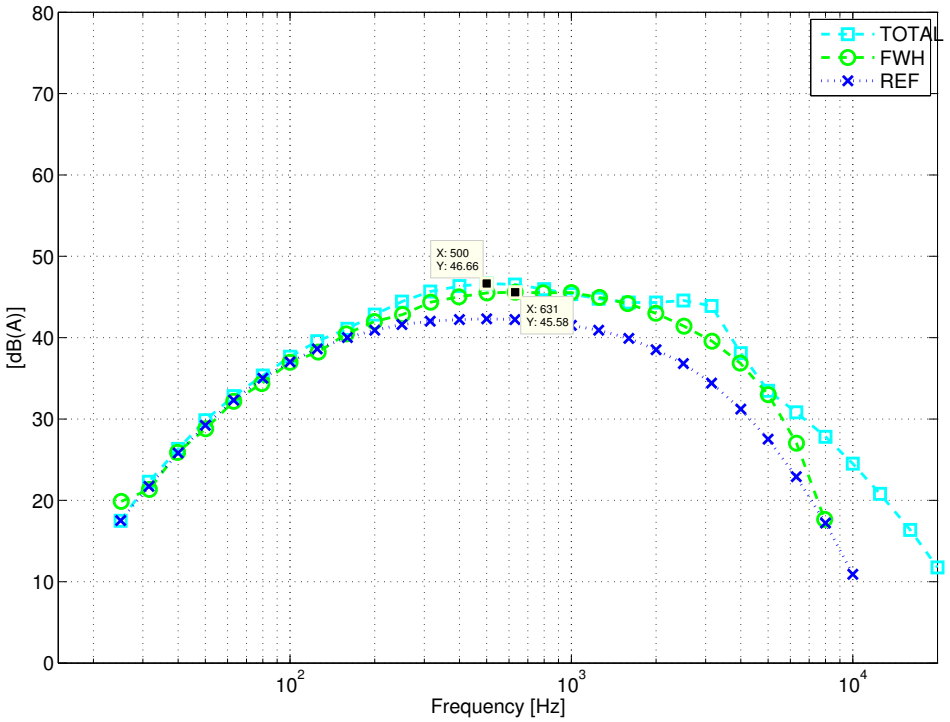

Figure 4.12.: A-weighted estimated and predicted one-third octave spectra for the NREL5M wind turbine at reference position 1. Wind speed 8m/s at 10m height. Turbulent length scale $\Lambda = 29.4m$. Turbulence intensity $I = 8.75\%$.

Figure 4.12 shows the A-weighted audio spectrum of the NREL5M wind turbine. As mentioned before, the reference data is a statistical estimate. Therefore, care should be taken in interpreting the results obtained with the reference spectrum.

However, the highest levels of the reference data are estimated around 200-1kHz at levels around 40-42.3dB(A). The overall A-weighted sound pressure level of the reference data in Figure 4.12 is 52.8dB(A). The highest predicted levels also occur in this frequency range. The highest predicted FAST level is 46.6dB(A) and the highest predicted FWH level is 45.5dB(A). The predicted A-weighted OASPLs are 56.8dB(A) and 55.7dB(A) for FAST and FWH respectively.

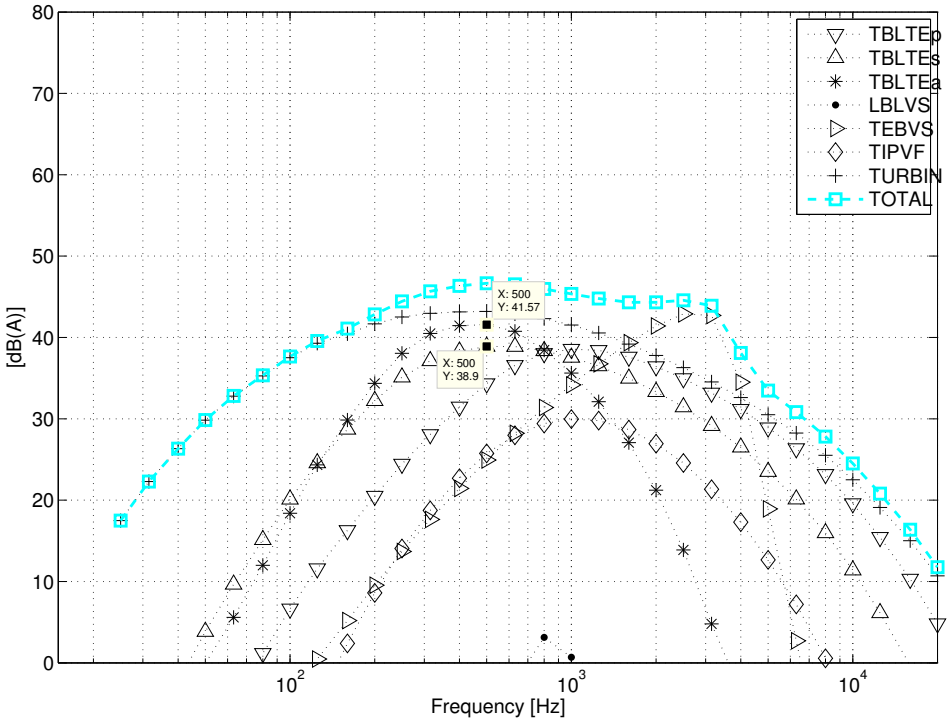

Figure 4.13.: A-weighted estimated and self-noise one-third octave spectra for the NREL5M wind turbine at reference position 1. Wind speed 8m/s at 10m height. Turbulent length scale $\Lambda = 29.4m$. Turbulence intensity $I = 8.75\%$.

Figure 4.13 shows the contribution of every semi-empirical noise mechanism to the predicted A-weighted TOTAL sound pressure level. It can be seen that the influence of the self-noise mechanisms on the TOTAL predicted sound pressure level in the A-weighted audio spectrum is much more pronounced than for the smaller turbine. Peak frequencies and levels of the single noise mechanisms do not change significantly compared to the non-weighted spectrum in Figure 4.11 except TBLTEα and TBLTEs. The peak frequency of TBLTEα and TBLTEs in the A-weighted spectrum shift to 500Hz (315Hz in non-weighted audio spectrum from Figure 4.11) and the peak level of TBLTEα is 5.5dB lower (41.6dB(A)) than in Figure 4.11. The peak level of TBLTEs noise, at now 500Hz, is 4.8dB lower (38.9dB(A)) than the peak level of TBLTEs noise in Figure 4.11. Furthermore, the peak level of TEBVS noise raises slightly by 1.2dB but the peak frequency stays the same.

Besides that, the usual cut-off of the low frequencies in the A-weighted spectrum according the A-weighting specifications from Section B.2 can be observed.

4.3.2.3. Variation of Λ

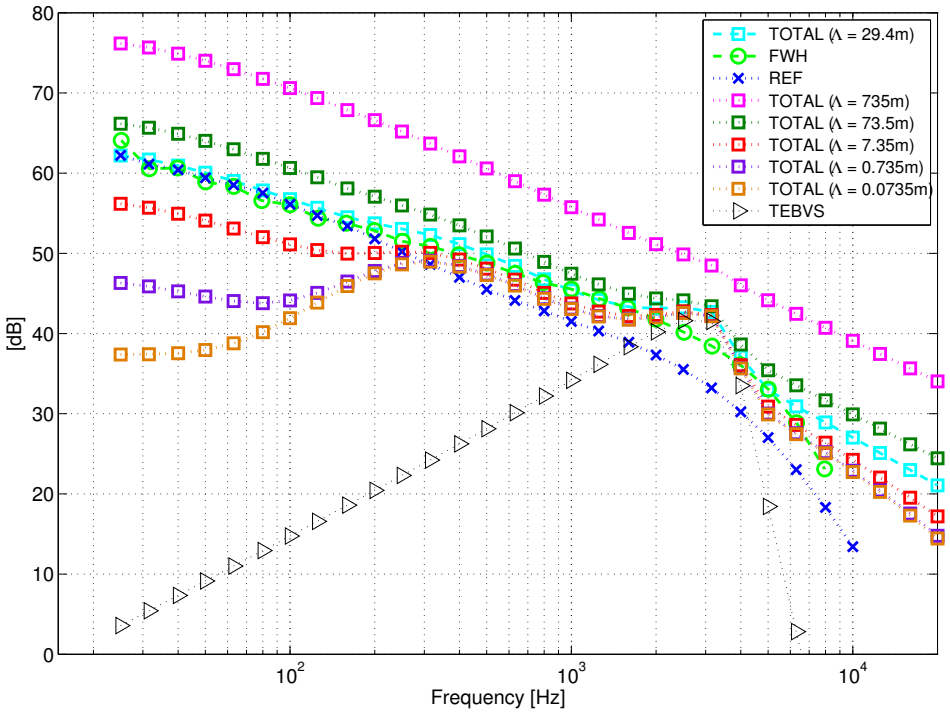

Figure 4.14.: Effect of inflow turbulence length scale on TOTAL sound pressure level prediction for the NREL5M wind turbine. Wind speed 8m/s at 10m height. Turbulence intensity $I = 8.75\%$.

As mentioned in Section 3.4.2 the turbulent length scale is a sensitive parameter for the turbulent inflow noise (TURBIN) prediction. It depends on the rotor size and site specific turbulence characteristic and should be chosen with care [24]. Figure 4.14 shows the dependence of the TOTAL predicted sound pressure level on this parameter for the non-weighted spectrum of the large turbine. Note, only the TURBIN noise mechanism changes with Λ, the remaining self-noise mechanisms are independent of this parameter. The smaller Λ is, the more pronounced are the self-noise components in the spectrum in Figure 4.14. For a very large Λ almost no tonal peak can be observed in the predicted spectrum anymore.

The turbulent length scale Λ in this plot varies over several orders of magnitude from some hundred meters (735.0m) to some centimeters (0.0735m). Best agreement between the two prediction methods is given for a length scale of $\Lambda = 29.4m$. This is 0.4 times the proposed value for the turbulent length scale in [1] which is 2.45 times the turbines hub hight up to a maximum of $\Lambda = 73.5m$ [24].

It is not yet known to what extent the turbulent inflow noise contributes to the total sound pressure level [27]. Λ might be handled as input parameter for future revisions of FAST [24] to account for the turbine and site specific characteristics of this parameter.

4.4. Directivity

Next the overall sound pressure levels around the investigated wind turbines are predicted in order to asses the directivity characteristic of wind turbine noise. The OASPL directivity pattern around a wind turbine is predicted for frequencies up to 1kHz, due to computational simulation time reasons, since these are the most pronounced frequencies in the non-weighted spectrum.

In the plots below the observers are equally distributed on the observer circle every 15 degrees. Observer position 1 in Figures 4.15 and 4.16 correspond to reference observer position 1 in Figure 4.4 in Section 4.2. Thus, 5 corresponds to 2, 13 to 3 and 21 to 4. The dOASPL in the plots below is the difference of the local observer position's OASPL to the mean OASPL over all positions of the observer circle.

Both noise prediction methods show good agreement concerning the OASPL directivity prediction for downwind observer positions (1-6, 21-24) for both investigated wind turbines. However, for the AOC 15/50 wind turbine a slight asymmetry in the predicted values can be observed which is even more pronounced for upwind observer positions (9-18).

For observer positions in the rotor plane or close to it the predicted values of both prediction methods show a significant mismatch. Nevertheless, both methods predict reduced noise levels in the rotor plane.

4.4.1. AOC 15/50

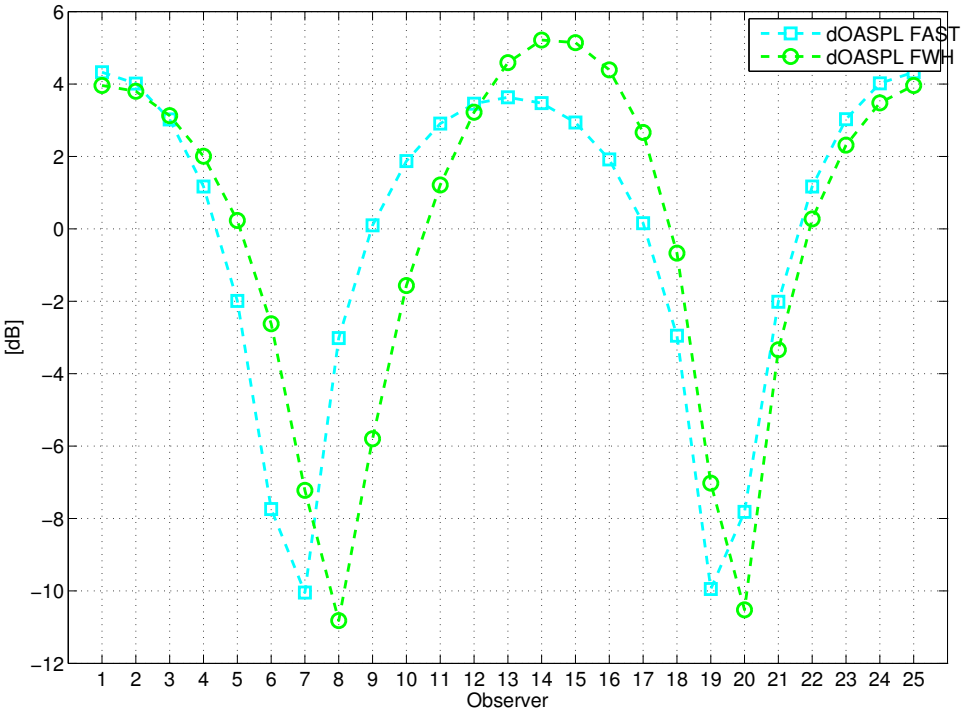

Figure 4.15.: OASPL directivity pattern around the AOC 15/50 wind turbine

4.4.2. NREL5M

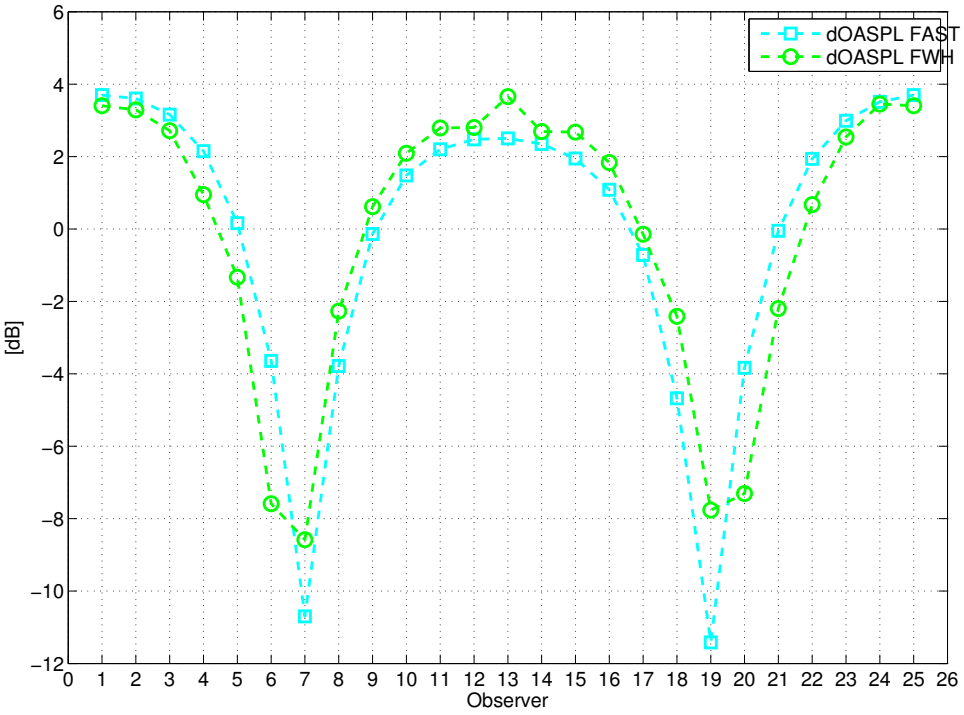

Figure 4.16.: OASPL directivity pattern around the NREL5M wind turbine

4.5. Comparison

In this Section a comparison of every single semi-empirical noise mechanisms, the total predicted sound pressure levels and the reference data between the two wind turbines is made. All spectra in this Section are related to the reference position 1 [3] in Section 4.2. The horizontal distance to the wind turbine in the case of the small AOC wind turbine is 32.5m, in case of the large NREL5M wind turbine the distance is 153m.

4.5.1. Reference data

The measured reference spectrum for the small AOC 15/50 turbine can be found in [2]. The reference spectrum for the large NREL5M wind turbine is a statistical estimate and derived through a thorough analysis of 48 wind turbines in the range of 1-3MW in [29]. It does not contain tonal information of any tonal vortex shedding mechanism. As noted before, care should be taken in interpreting the reference data for the large turbine, so only general statements about the reference spectra are possible. See Section 4.1 for the derivation of the reference SPL values out of the estimated A-weighted sound power spectrum in [29].

Non-weighted Both reference spectra in Figure 4.17, of the two wind turbines, show a broadband characteristic with pronounced low frequency levels and gradually decreasing SPLs towards higher frequencies. The reference spectrum for the small turbine shows 5 peaks at 40Hz (59.9dB), 200Hz (54.1dB), 500Hz (62.4dB), 1kHz (53.1dB) and 1.6kHz (48.8dB). The 500Hz peak is believed to be gearbox noise [24] and shows the highest level throughout the spectrum. The highest level of 62.2dB of the large turbine is estimated to occur at 25Hz.

The overall sound pressure level of the measured reference spectrum for the small turbine is 68.7dB and 68.8dB for the large turbine.

A-weighted The the tonal 500Hz peak in the A-weighted reference spectrum of the small turbine in Figure 4.18 still shows the highest level of 59.2db(A) throughout the spectrum. Highest levels for the large turbine are estimated for frequencies in the range of 200Hz to 1kHz (42.3dB(A)).

The overall A-weighted sound pressure level of the measured reference spectrum for the small turbine is 62.5dB(A) and for the large turbine the estimated OASPL is 52.8dB(A).

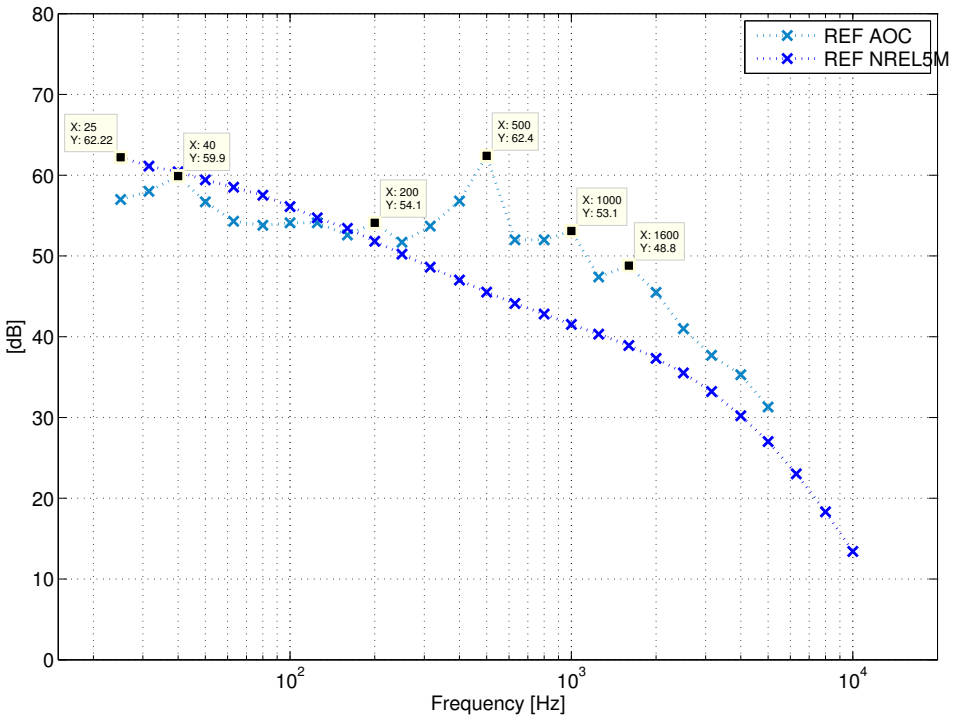

Figure 4.17.: Comparison of reference data for the non-weighted spectrum

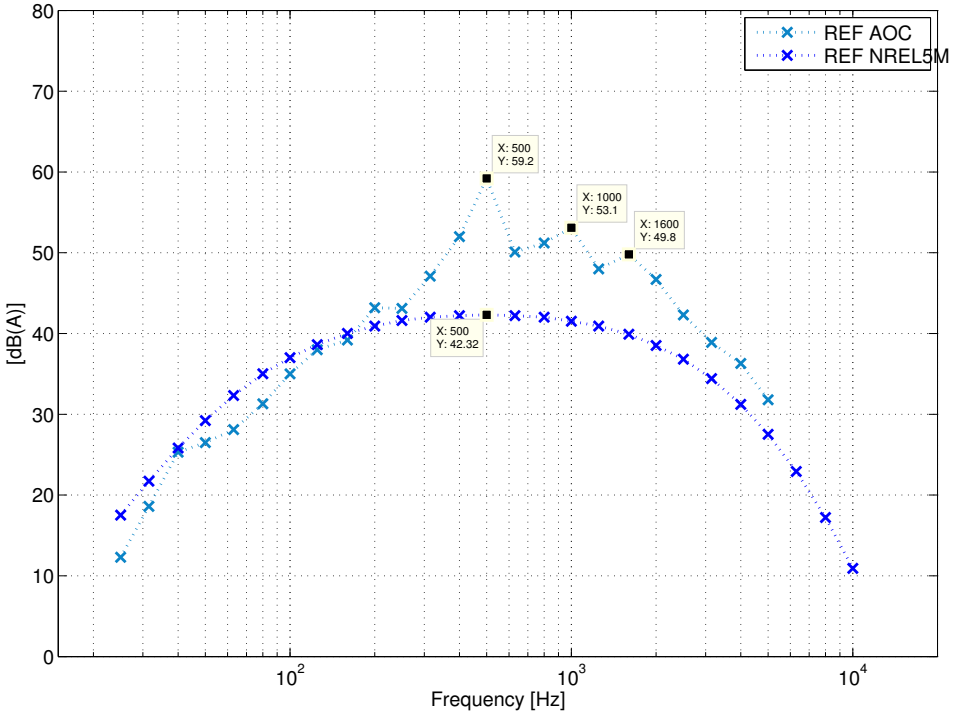

Figure 4.18.: Comparison of reference data for the A-weighted spectrum

4.5.2. Total predicted SPL

In this Section the total predicted sound pressure level spectra of the FAST and the FWH prediction of both turbines are compared to each other.

4.5.2.1. FAST

The FAST model predicts higher low frequency levels for the large turbine. Both spectra of both turbines, whether for the non- or A-weighted spectra, are dominated by broadband turbulent inflow (TURBIN) noise except for some vortex shedding noise at an annoying frequency range of 1-4kHz. This tonal peaks, due to vortex shedding noise, are even more pronounced when A-weighting is applied.

Non-weighted The highest non-weighted level for the small turbine is predicted by FAST at 63Hz with 55dB. Two tonal peak are predicted in the spectrum in Figure 4.19 of the small turbine, one at at 1.25kHz with 52.6dB and one at 1.6kHz with 51.6dB. The highest level for the large turbine is predicted at 25Hz with 62.2dB. One tonal peak is predicted at 3.15kHz with 42.7dB.

A-weighted In the A-weighted spectrum in Figure 4.20 of the small turbine the tonal peak frequencies remains the same with levels of 53.2dB(A) and 52.5dB(A). The peak level of the large turbine is predicted to be 46.7dB(A) at 500Hz and the tonal component remains at 3.15kHz with 43.9dB(A).

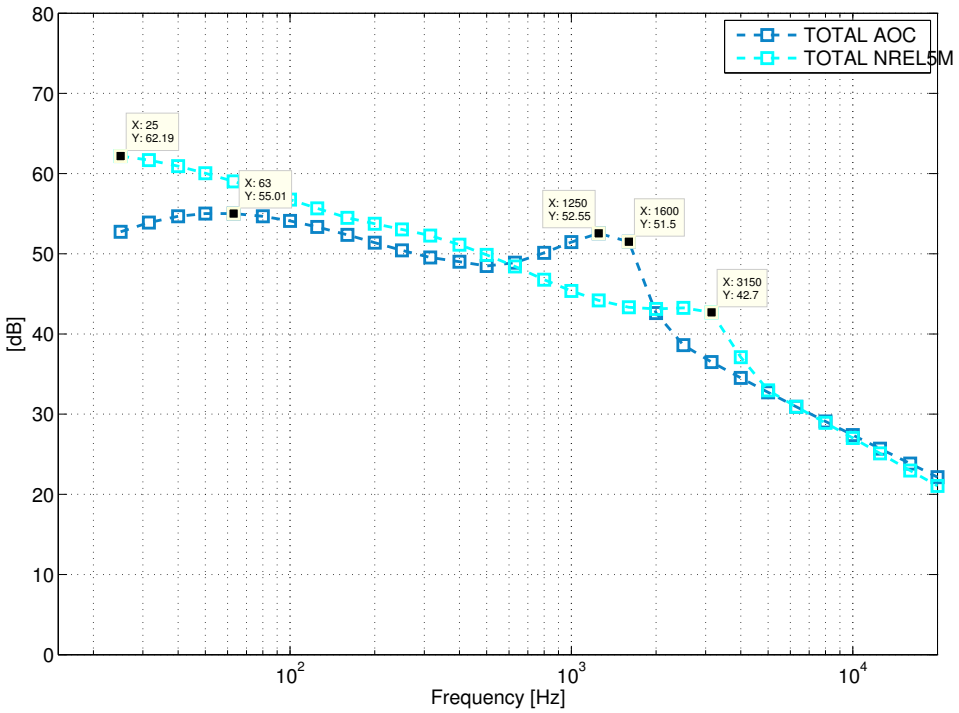

Figure 4.19.: Comparison of FAST prediction for the non-weighted spectrum

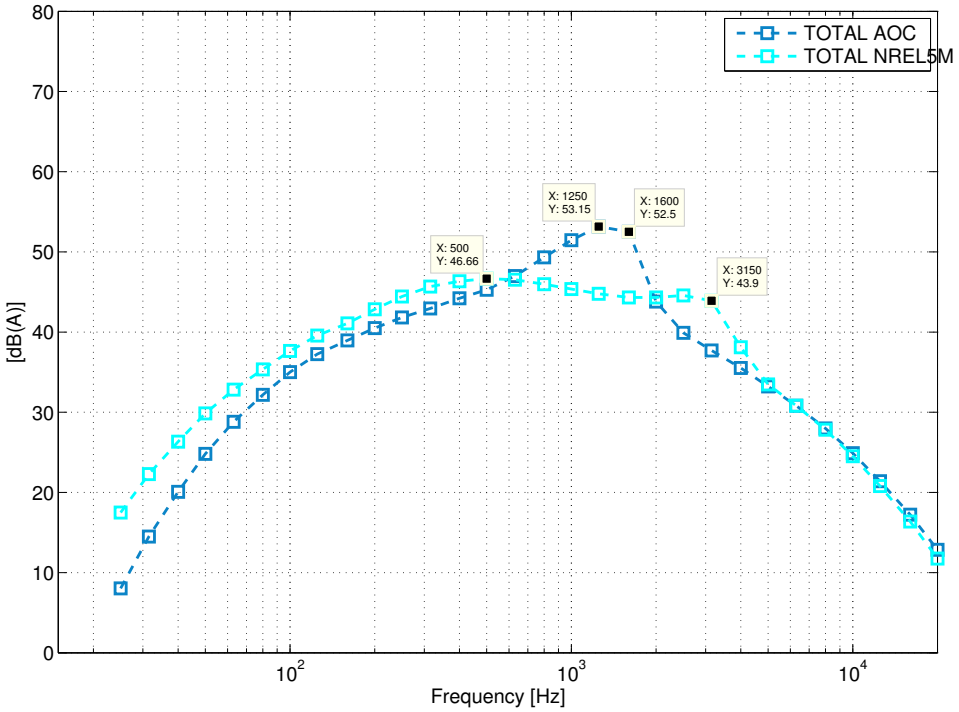

Figure 4.20.: Comparison of FAST prediction for the A-weighted spectrum

4.5.2.2. FWH

Figures 4.21 and 4.22 show the non- and A-weighted predicted spectra of the small and the large turbine with the FWH model. The FWH spectrum curve is the result of a Fourier analysis of the pressure curve as calculated according to equation 3.19. The reference sound pressure is $p_{ref} = 2 \cdot 10^{-5} Pa$.

Non-weighted The non-weighted spectrum of the turbines in Figure 4.21 shows highest predicted levels for the lowest frequencies at around 40-80Hz with around 60dB for the small and at 25Hz with 64dB for the large turbine.

A-weighted The A-weighted spectrum in Figure 4.22 shows a plateau for the small turbine at around 40dB(A) and a highest level of 45.5dB(A) for the large turbine.

4.5.2.3. Summary

Following Table 4.1 summarizes the predicted and reference non- and A-weighted OASPLs for both turbines at the observer position 1.

Table 4.1.: Reference and predicted non- and A-weighted OASPLs of the AOC 15/50 and the NREL5M wind turbines

OASPL	non-weighted [dB]			A-weighted [dB(A)]		
	Reference	FAST	FWH	Reference	FAST	FWH
AOC 15/50	68.7	65.4	67.7	62.5	59.2	51
NREL5M	68.8	68.9	69.3	52.8	56.8	55.7

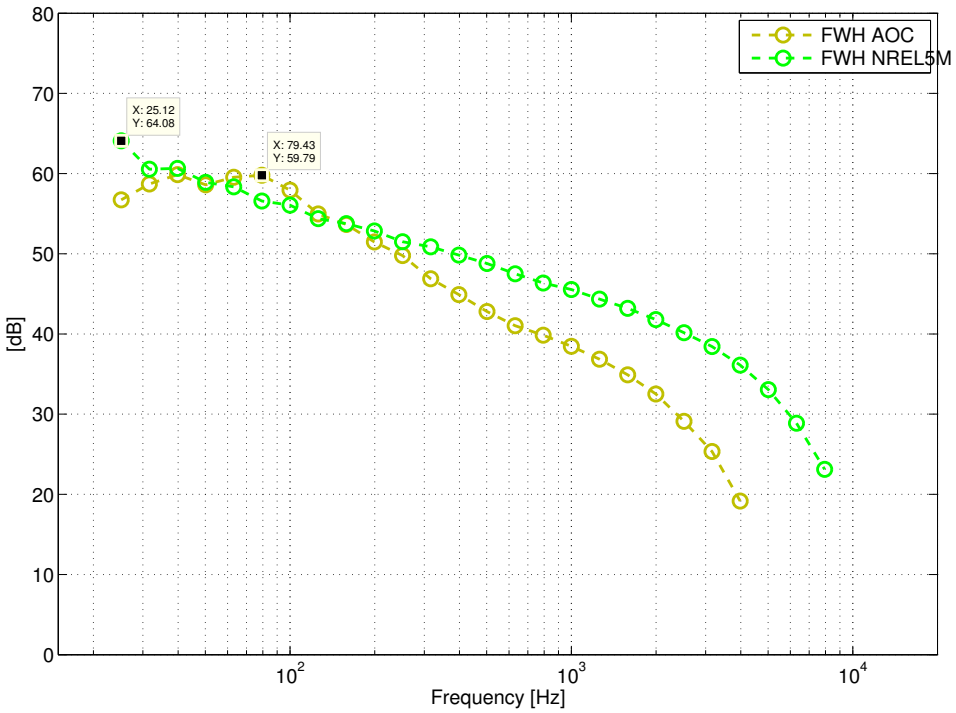

Figure 4.21.: Comparison of FWH prediction for the non-weighted spectrum

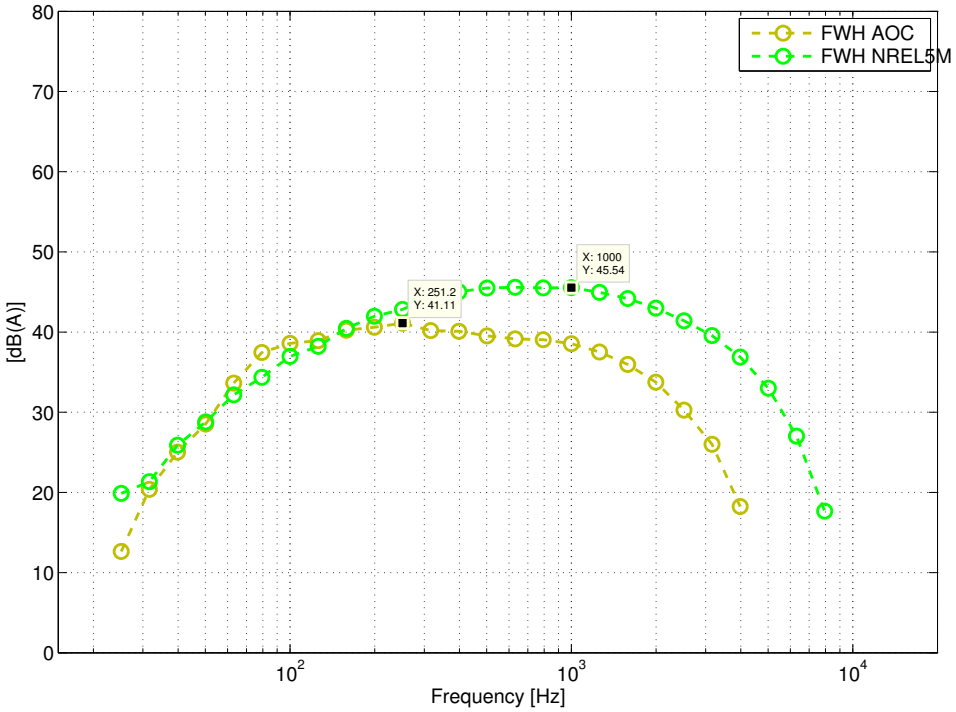

Figure 4.22.: Comparison of FWH prediction for the A-weighted spectrum

4.5.3. Self-noise

In this Section the single self-noise contributer to the predicted TOTAL SPL spectra of the FAST prediction for both turbines are compared to each other.

4.5.3.1. TBLTEp/s

From Figures 4.23 and 4.24 it can be seen that trailing edge scatter noise is more pronounced for the large wind turbine.

Non-weighted Concerning the non-weighted spectrum from Figure 4.23 the peak level of TBLTEs noise of the large turbine (43.7dB at 250Hz) is 11.9dB higher than of the small turbine (31.8dB at 800Hz). The peak level of TBLTEp noise is 13.7dB higher of the large (38.8dB at 800Hz) compared to the small turbine (25.1dB at 2.5kHz).

The peak frequencies shift towards lower frequencies with growing turbine size. The peak level of TBLTEs noise shifts down from 800Hz to 250Hz and the peak frequency of TBLTEp noise shifts down from 2.5kHz to 800Hz.

A-weighted Concerning the A-weighted spectrum in Figure 4.24 the lower frequency TBLTEs peak level of the large turbine shifts from 250Hz to 500Hz. There is also a slight shift in frequency for the TBLTEp peak level from 800Hz to 1kHz but the level changes are marginal. The same holds for the TBLTEs peak level of the small turbine. A small frequency shift can be observed from 800Hz to 1kHz when applying A-weighting but the level changes are also marginal. The peak level of TBLTEp noise of the small turbine gains some 1.3dB when A-weighting is applied but the peak frequency stays the same.
The peak level of TBLTEs noise of the large turbine is 7.2dB higher than for the small turbine. The peak level of TBLTEp noise of the large turbine is 12.2dB higher than for the small turbine.

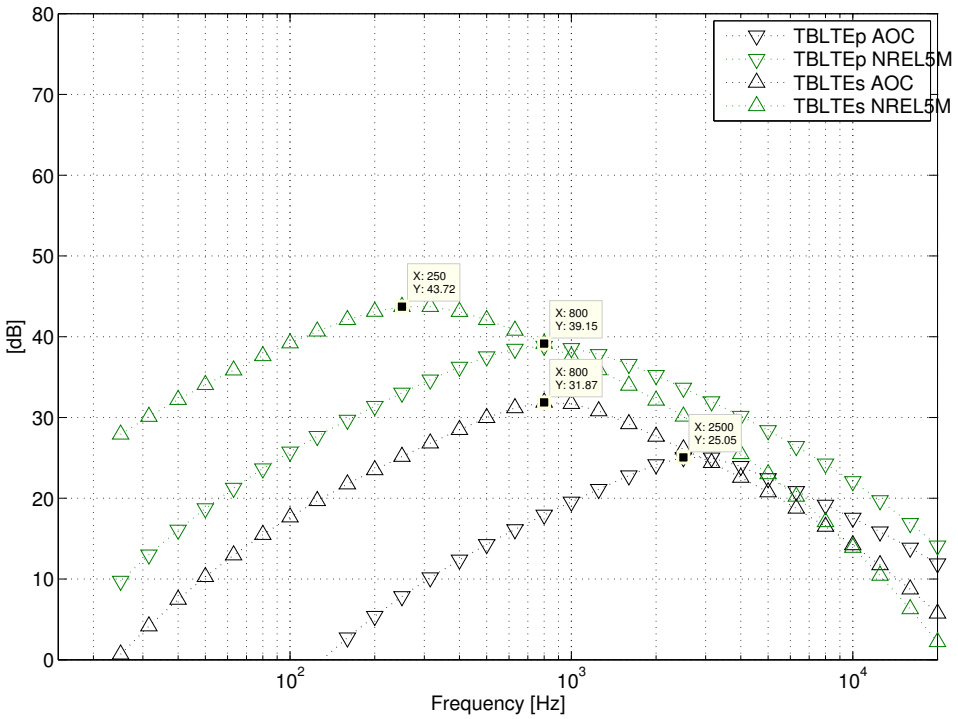

Figure 4.23.: Comparison of TBLTEp/s noise for the non-weighted spectrum

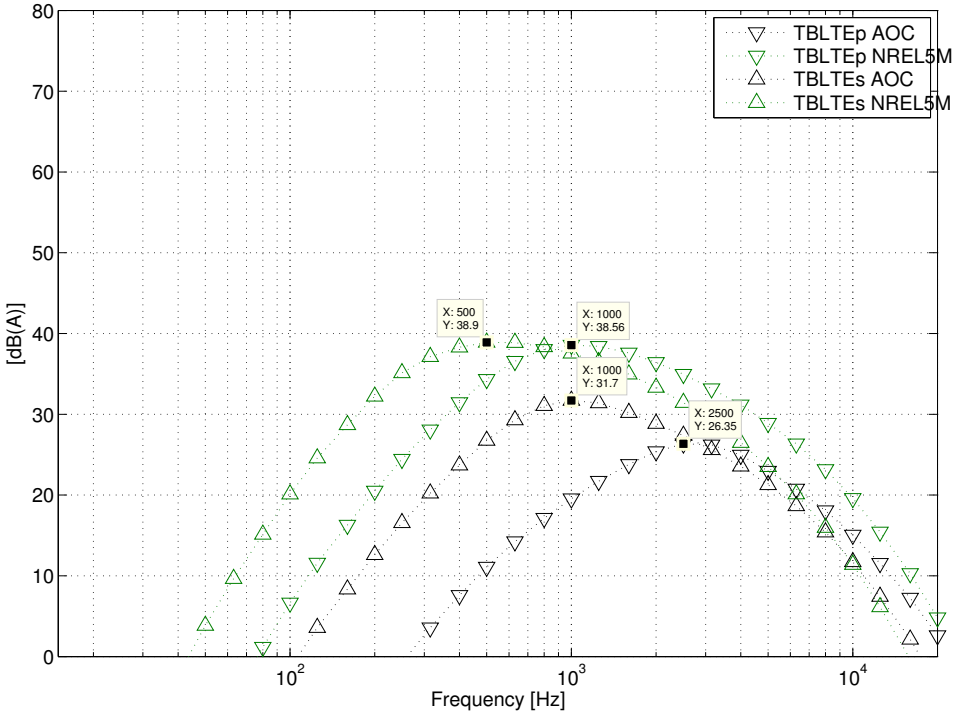

Figure 4.24.: Comparison of TBLTEp/s noise for the A-weighted spectrum

4.5.3.2. TBLTEa

Separation stall noise (TBLTEa) is also more pronounced for the large turbine.

Non-weighted The spectrum in Figure 4.25 shows a peak level of 47.1dB of the large turbine which is 11.5dB higher than the small turbine. The peak frequency on the other hand is lower for the large turbine (315Hz) than for the small turbine (1kHz) as expected. Further, the small turbine is predicted to emit almost the same level of TBLTEa noise in in the lowest frequency range from 25-50Hz as the large turbine.

A-weighted The A-weighted spectrum in Figure 4.26 shows a decreased peak level of TBLTEa noise by 5.5dB (41.6dB(A)) and a slightly shifted peak frequency to around 400-500Hz of the large turbine. The peak level of TBLTEa noise of the small turbine stays the same, same as the peak frequency. The lower frequencies are cut-off in the A-weighted spectrum.

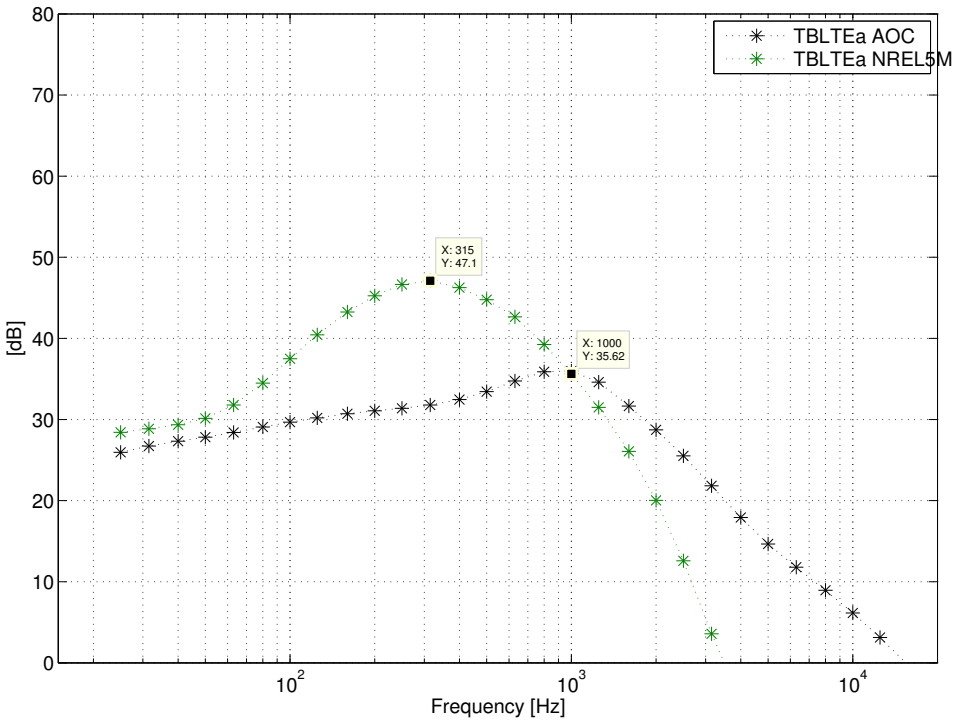

Figure 4.25.: Comparison of TBLTEa noise for the non-weighted spectrum

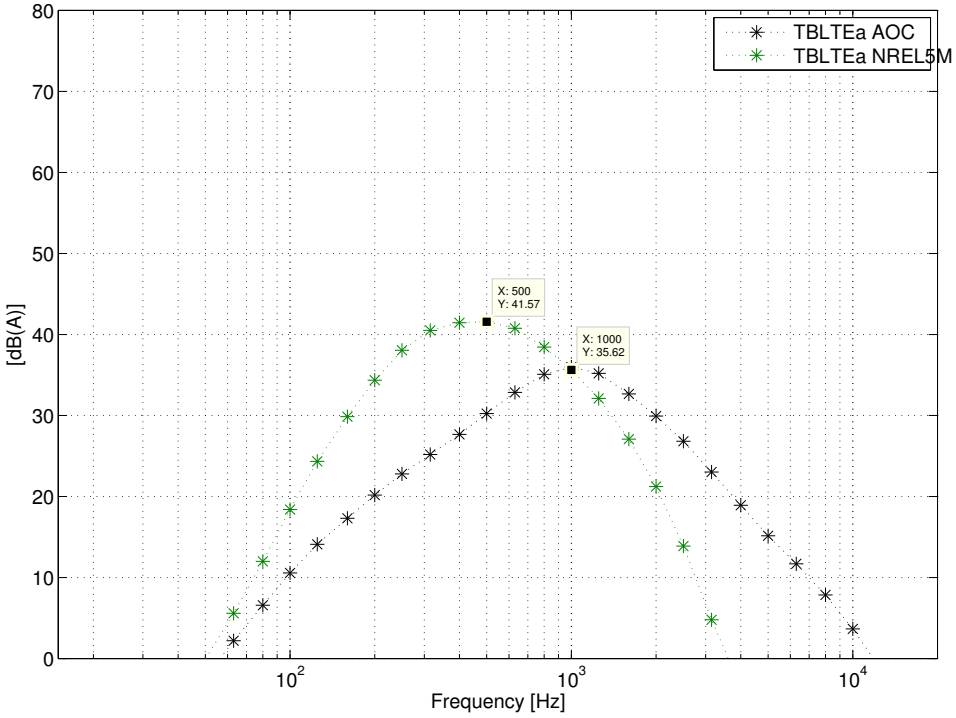

Figure 4.26.: Comparison of TBLTEa noise for the A-weighted spectrum

4.5.3.3. LBLVS

LBLVS noise is of minor importance for the large turbine, as one would expect. The transition of the boundary layer, on either side of the turbine blade, from laminar to turbulent, happens well before the flow reaches the trailing edge, when considering an average chord length of several meters.

For the small turbine, LBLVS noise is responsible for a significant peak in either spectrum, non-weighted or A-weighted.

Non-weighted The peak level of LBLVS noise in the non-weighted spectrum of the small turbine in Figure 4.27 is 50.6dB. The peak frequency is 1250Hz. A mild spectral peak of LBLVS noise can also be observed for the large turbine at 63Hz with 17.9dB and an even smaller one at 800Hz with only 3.9dB.

A-weighted The peak level of LBLVS noise in the A-weighted spectrum of the small turbine in Figure 4.28 does not change significantly. It is 51.2dB(A). The peak frequency stays the same at 1.25kHz. The mild spectral peak of LBLVS noise of the large turbine at 63Hz drops of the scale, the 800Hz peak remains at 3.1dB(A).

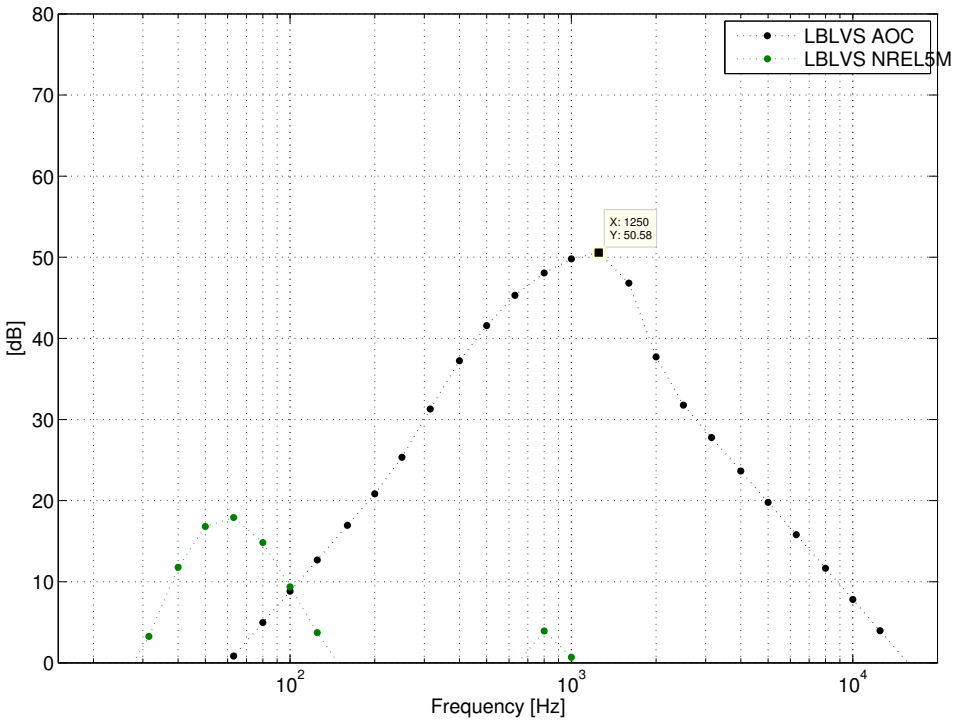

Figure 4.27.: Comparison of LBLVS noise for the non-weighted spectrum

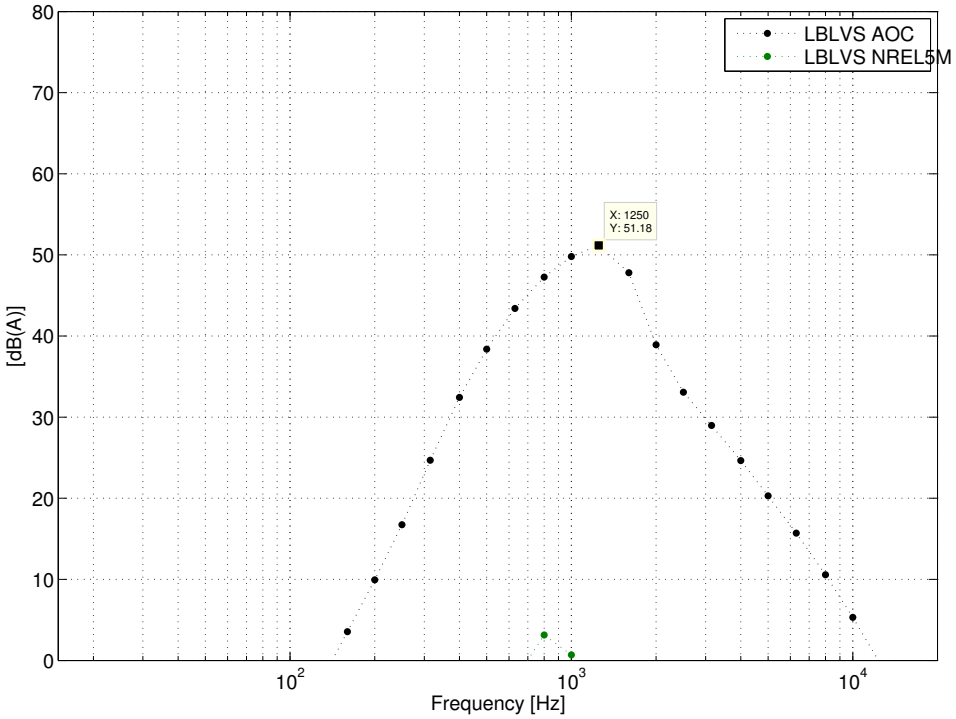

Figure 4.28.: Comparison of LBLVS noise for the A-weighted spectrum

4.5.3.4. TEBVS

TEBVS noise is a significant tonal noise component for both turbines. Nevertheless, no geometrical data for trailing edge bluntness for the large turbine was available and default values are used, so the predicted peak levels and frequency of TEBVS noise might not represent the actual values.

Non-weighted The peak level of TEBVS of the small turbine, where trailing edge thickness data was available, for the non-weighted spectrum in Figure 4.29 is 49.1dB at 1.6kHz. In Section 4.3.1.1 a brief explaination is given for how to estimate the occurrence of this vortex shedding frequency with the Strouhal number. For the large turbine a peak level of TEBVS noise of 41.5dB is predicted at a frequency of 2-3kHz.

A-weighted The A-weighted spectrum in Figure 4.30 shows no significant change in predicted peak TEBVS level or frequency for both turbines. All peak levels raise about 1dB compared to the non-weighted spectrum. TEBVS noise gains importance when A-weighting is applied.

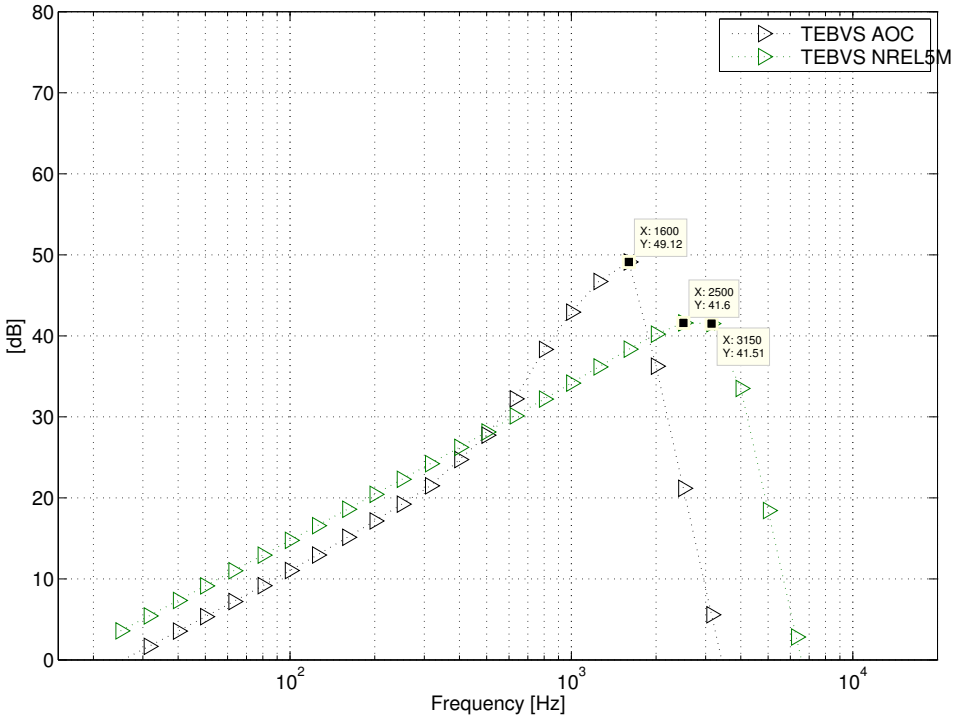

Figure 4.29.: Comparison of TEBVS noise for the non-weighted spectrum

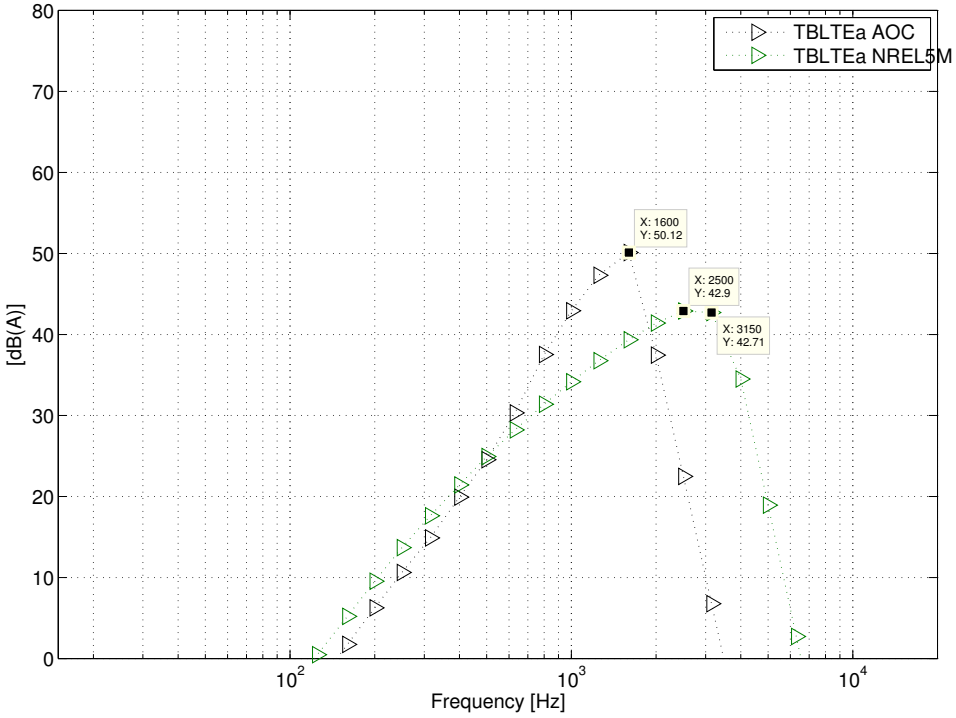

Figure 4.30.: Comparison of TEBVS noise for the A-weighted spectrum

4.5.3.5. TIPVF

Tip vortex formation noise is an inefficient noise source for both turbine models. However, its spectral peak shifts downwards with growing turbine size with an enhanced amplitude which might be due to an enhanced loading on the large turbine. As discussed in the theory Section 2.1.4, the loading can be expressed as a circulation around the turbine blade (wing). As a consequence a stronger tip vortex is formed and hence a higher level of TIPVF noise can be observed.

Non-weighted The spectral peak level of TIPVF of the large turbine concerning the non-weighted spectrum in Figure 4.31 is 30.2dB at a peak frequency of 800Hz. The peak level of the small turbine is 7.3dB lower (23dB) at a peak frequency of 1.6kHz.

A-weighted The A-weighted values in Figure 4.32 do not change significantly. However, the peak frequency of the large turbine slightly shifts to 1kHz, the level is maintained. The peak level of for the small turbine slightly rises 1dB at the same frequency.

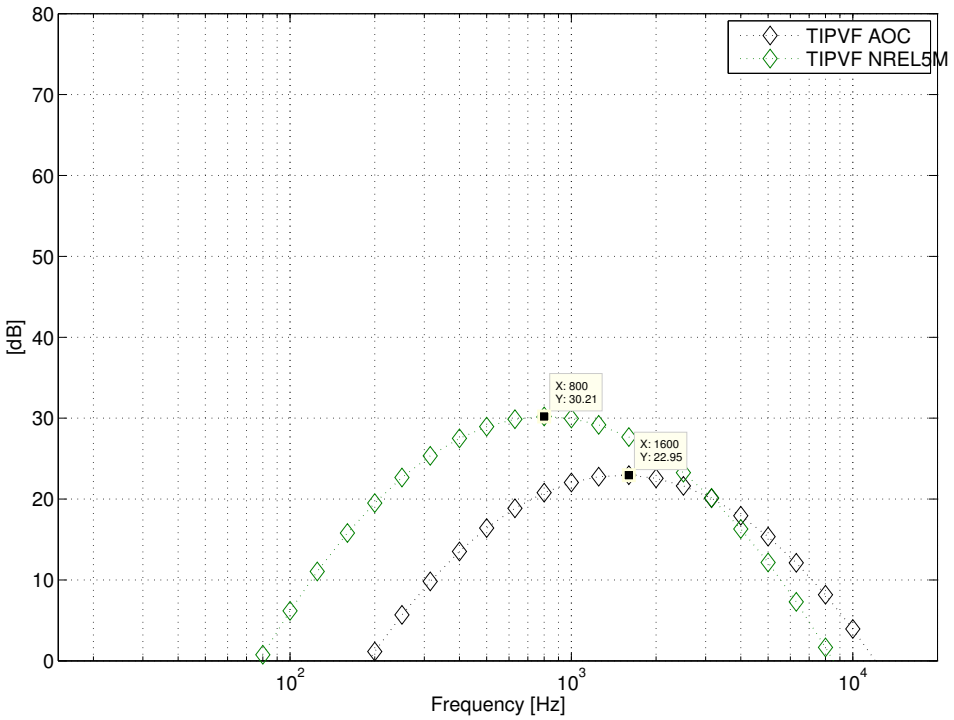

Figure 4.31.: Comparison of TIPVF noise for the non-weighted spectrum

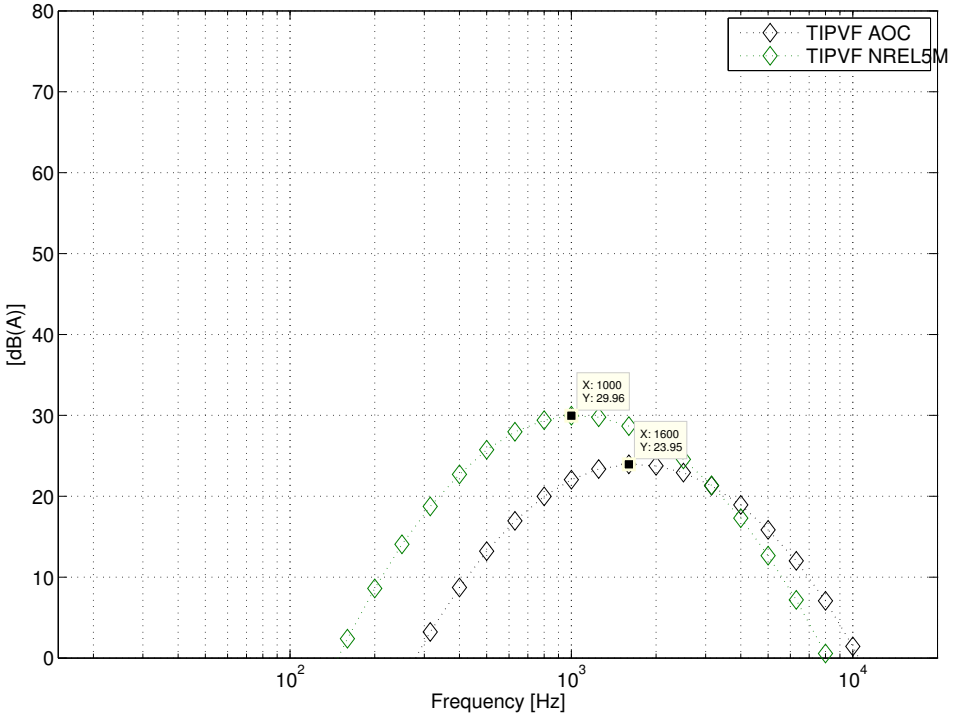

Figure 4.32.: Comparison of TIPVF noise for the A-weighted spectrum

4.5.4. Turbulent inflow noise

In this Section the TURBIN contribution to the predicted TOTAL SPL spectra of the FAST prediction of both turbines is compared to each other.

TURBIN noise is the dominant noise contributer to the predicted TOTAL SPL. This noise mechanism shows the highest levels throughout the spectrum. The predicted level is quite sensitive to the adjusted turbulent length scale. The turbulent length scales used in the spectra of Figures 4.33 and 4.34 are 24.5m for the small turbine and 29.4m for the large turbine. The TURBIN noise spectrum shows higher levels in the low frequency range up to 200Hz for the large turbine and the levels of both turbines lay within 2dB for frequencies above 200Hz in the non- as well as in the A-weighted spectrum.

Non-weighted The highest levels in the non-weighted spectrum in Figure 4.33 occur for the lowest frequencies, 62.2dB at 25Hz for the large turbine and 55dB at 63Hz for the small turbine.

A-weighted The spectral peaks in the A-weighted spectrum in Figure 4.34 occur at 500Hz for both turbines at levels of 43.2dB(A) for the large and 44dB(A) for the small turbine.

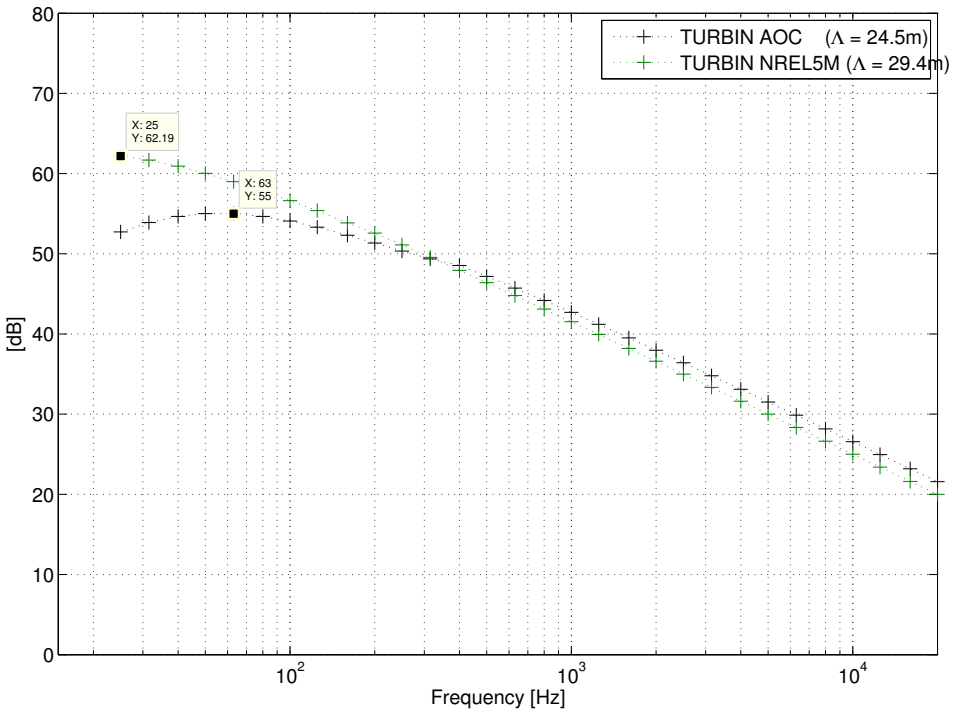

Figure 4.33.: Comparison of TURBIN noise for the non-weighted spectrum

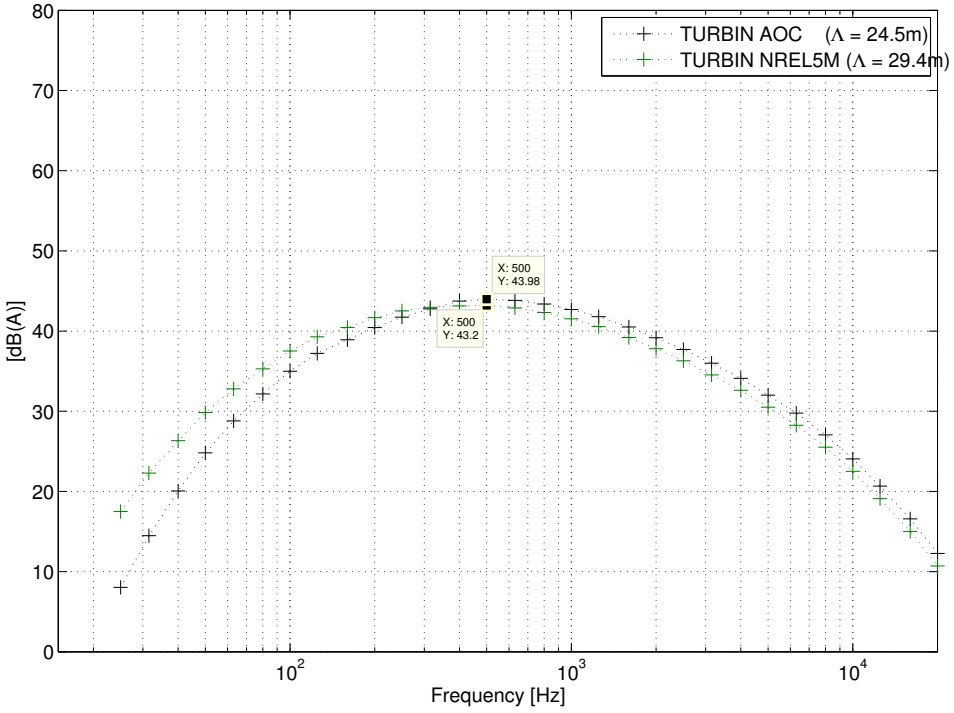

Figure 4.34.: Comparison of TURBIN noise for the A-weighted spectrum

4.6. Conclusion

For the small AOC 15/50 wind turbine the FAST and the FWH methods predict significantly different sound pressure levels. Only the FAST model is in good agreement with the reference measurement data, except the lowest frequencies below 50Hz. In this frequency range the FWH model shows good agreement with the reference data. The results obtained for the large NREL5M wind turbine, however, show good agreement between the two prediction methods throughout the spectrum. The estimated levels, at low frequencies up to 200Hz, are exactly predicted of both prediction methods and both methods agree in predicting higher levels for higher frequencies.

The two tonal peaks of the measured reference spectrum of the small AOC 15/50 are well predicted by the semi-empirical model. These peaks are related to vortex shedding noise due to LBLVS and TEBVS. Applying A-weighting to the spectrum makes these peaks even more pronounced because they occur at a frequency range of 1-4kHz. Generally, all non-weighted spectra of both prediction models show enhanced low frequency noise levels with highest levels at around 40-80Hz for the small turbine and at the lowest frequency of 25Hz for the large NREL5M wind turbine. As the major contributer to the low frequency noise levels turbulence inflow noise (TURBIN) is identified. The low frequency levels of the large turbine are generally larger. Furthermore, the TURBIN mechanism dominates the spectrum of both turbines, especially of the small turbine. However, the spectrum of the large turbine shows an increasing influence of the self-noise mechanisms for intermediate to high frequencies. For the A-weighted spectrum this effect is, off course, even more pronounced. As the major broadband self-noise contributer to the total predicted A-weighted spectrum, suction and pressure sided edge scatter (TBLTEs/p) as well as separation stall (TBLTEα) noise are identified. The low frequency high level and high frequency low level characteristic of TBLTE noise is evident.

The TOTAL predicted spectra of the semi-empirical model is sensitive to the turbulent length scale Λ used for the TURBIN noise mechanism. Λ is a turbine size and site specific parameter [24]. Best agreement in the TOTAL predicted SPLs, concerning the spectra of both wind turbines, is obtained with a length scale of 0.4 times smaller than the proposed value for the turbulent length scale in [1]. The length scales used for the small and the large turbine are 24.5m (IEC value 61.25m) and 29.4 (IEC value 73.5m), respectively. Because there is the uncertainty in the turbulent length scale, it is suggested in [24] to appoint this as an input parameter for future revisions of FAST.

The FWH prediction showed good agreement with the FAST prediction for the large NREL5M turbine and diverse results for the small AOC 15/50 wind turbine. The reason could be related to the different levels of blade loading. The blade loading on the large NREL5M turbine blades is significantly higher than the loading on the small AOC 15/50 wind turbine. Hence, the fluctuating overall aerodynamic force on the heavily loaded rotor represents an integral value over all fluctuating surface pressures. In other words, it incorporates all effects due to inflow turbulence impingement, turbulent boundary layer trailing edge scatter and separation stall effects. Therefore the sound pressure field of an highly loaded rotor can be calculated by using an FWH approach with unsteady chordwise aerodynamic loadings when it is not practical or possible to numerically calculate the complete pressure distribu-

tion around a wind turbine blade by means of computational expensive CFD. However, tonal events such as laminar boundary layer or trailing edge bluntness vortex shedding are not represented by the FWH method. No tonal peaks can be observed in the predicted FWH spectra.

Both noise prediction methods deliver acceptable results for the large wind turbine but only the semi-empirical model is applicable to predict noise for the small wind turbine. This and together with the fact that the noise subroutines in FAST executes much faster than the FWH-code and the ability to predict tonal events in the spectrum makes the semi-empirical model clearly the more favorable and a powerful wind turbine noise prediction tool.

5. Summary and outlook

This thesis deals with aeroacoustic noise prediction of wind turbines. Two different approaches are used and compared to each other. One method is based on semi-empirical aeroacoustic formulations and the other uses an analytical approach based on the Ffowcs-Williams and Hawkings (FWH) aeroacoustic analogy wave equation. The loading terms in the FWH approach are replaced by a spanwise load distribution as calculated in AeroDyn. The results of both methods are plotted against reference data in one-third octave bands.

In the introduction to this project a thorough literature study was done in order to learn more about aeroacoustic noise from wind turbines. As a next step the source codes were needed to be adapted. Several data handling subroutines and additional loops to account for multiple observer prediction as well as multiple blades are implemented by the author. The sources codes, used in this master thesis, are all freely available. FAST is used to predict noise by means of semi-empirical aeroacoustic formulations. The FWH source code is taken from the OpenFOAM project. The post processing of the resulting acoustic data is done in MATLAB. All post processing audio analysis scripts are written by the author.

The noise emissions of two different sized wind turbines, a small 50kW downwind wind turbine (AOC 15/50) and a concept study of a 5MW upwind wind turbine (NREL5M), are analyses in this thesis. The results are compared to reference data. Generally the one-third octave plots obtained show enhanced low frequency noise emissions of wind turbines with even more pronounced low frequencies noise emissions of the large wind turbine. Tonal noise occurs for both turbine models in an most annoying frequency range of 1-4kHz and is likely to dominate the A-weighted spectrum. Further, trailing edge noise is increasingly important for large wind turbines and is also most pronounced in the A-weighted spectrum. The turbulent length scale, that is use for the turbulent inflow model, is set to a value 0.4 times smaller than the IEC specified length scale, as this shows the best agreement with the reference data. The predicted spectra of both noise predicting methods show good agreement for the large turbine. Only the FAST model delivers acceptable results for the small turbine.

Further improvements:

- The noise subroutine in FAST uses the original thickness subroutine from the study of BPM [23] to calculate the boundary layer displacement thickness. This subroutine uses empirical relations to calculate the displacement thickness of a NACA0012 profile. In order to account for actual airfoil profiles used in recent wind turbine design to obtain more accurate results of the boundary layer displacement thickness, airfoil design tools such as XFOIL[1] or XFLR5[2] should be used instead.

[1] http://web.mit.edu/drela/Public/web/xfoil/
[2] http://www.xflr5.com/xflr5.htm

- Errors in airfoil data tables are the single largest source of error in most rotor load and performance predictions [17]. So it is important to use reliable airfoil polars as input for AeroDyn which also gives room for further improvements.
- In order to improve vortex shedding noise prediction due to trailing edge bluntness of the large NREL5M wind turbine actual trailing edge geometrical data is vital.
- Best results in predicted noise for the large turbine are obtained when using a turbulent length scale much smaller than the standardized one. The correct use of the turbulent length scale of incoming atmospheric turbulence is another lead for further improvement.

References

[1] Wind turbine generator systems - part 1: Saftey requirements. iec standard 61400-1, 1998.

[2] Acoustic noise test report for the aoc 15/50 wind turbine. Technical report, National Wind Technology Center (NWTC). Golden, Colorado, 1999.

[3] Wind turbine generator systems - part 11: Acoustic noise measurement techniques. iec standard 61400-11, 2002.

[4] Normal equal-loudness-level contours, 2003.

[5] Life cycle assessment of offshore and onshore sited wind power plants based on vestas v90-3.0 mw turbines. 2006.

[6] R.K. Amiet. Acoustic radiation from an airfoil in a turbulent stream. *Journal of sound vibration*, 1975.

[7] E. Arcondoulis. Investigation of airfoil noise generation mechanisms at low to moderate reynolds number.

[8] T. Burton N. Jenkins D. Sharpe E. Bossanyi. *Wind Energy Handbook*. Wiley, 2nd edition edition, 2011.

[9] K.S. Brentner. Sensitivity of acoustic predicitions to variations of input parameters. *Journal of the american helicopter society*, 1994.

[10] R.H. Crawford. Life cycle energy and greenhouse emissions analysis of wind turbines and the effect of size on energy yield. *Renewable and Sustainable Energy Reviews 13*, 2009.

[11] J. Delfs. *Grundlagen der Aeroakustik (Basics of aeroacoustics)*. 2012.

[12] F. Farassat. Derivation of formulation 1 and 1a of farassat. 2007.

[13] K.S. Brentner F. Farassat. Modeling aerodynamically generated sound of helicopter rotors.

[14] H. Schlichting K. Gersten. *Grenzschicht-Theorie*. Springer, 2006.

[15] D.J. Laino A.C. Hansen. *AeroDyn Theory User's Guide*. Windward Engineering, December 2004.

[16] M.O.L. Hansen. *Aerodynamics of wind turbines*. Earthscan, 2008.

[17] P.J. Moriarty A.C. Hansen. *AeroDyn Theory Manual*. NREL, National Renewable Energy Laboratory Windward Engineering, December 2004.

[18] G. Leloudas W. J. Zuh J. N. Sorensen W. Z. Shen S. Hjort. Prediction and reduction of noise from a 2.3mw wind turbine. *Journal of Physics*, 2007.

[19] G. Ingram. Wind turbine blade analysis using the blade element momentum method., 2011.

[20] B.J. Jonkman. *TurbSim Theory User's Guide.* NREL, National Renewable Energy Laboratory, August 2009.

[21] J.M. Jonkman M.L. Buhl Jr. *Fast User's Guide.* NREL, National Renewable Energy Laboratory, August 2005.

[22] M.V. Lowson. Assessment and predicition of wind turbine noise, 1992.

[23] T.F. Brooks D.S. Pope M.A. Marcolini. Airfoil self-noise and prediction. Technical report, NASA, 1989.

[24] P.J. Moriarty P. Migliore. *Semi-Empirical Aeroacoustic Noise Prediction Code for Wind Trubines.* NREL, National Renewable Energy Laboratory, December 2003.

[25] M. Moeser. *Engineering Acoustics.* Springer-Verlag Berlin Heidelberg NewYork, 2004.

[26] P. Mohanamuraly. Acoustic prediction of heavy lift rotor configuration using momentum source method. Master's thesis, The Pennsylvania State University, 2010.

[27] S. Oerlemans. *Detection of Aeroacoustic Sound Sources on Aircraft and Wind Turbines.* 2009.

[28] S. Oerlemans. Wind turbine noise: Primary noise sources. 2011.

[29] H. Moller C.S. Pedersen. Low-frequency noise from large wind turbines. *Journal of the Acoustical Society of America*, 2010.

[30] A. Marn H.P. Pirker. *Technische Akustik und laermarm Konstruieren.* 2011.

[31] J.F. Mannwell J.G. McGowan A.L. Rogers. *Wind energy explained - Theory, design and application.* Wiley, 2009.

[32] C. Wagner T. Huettl P. Sagaut. *Large-Eddy Simulation for Acoustics.* Cambridge University Press, 2007.

[33] D.G. Shepherd. Historical development of the windmill. 1990.

[34] H. Steiner. *Advanced Fluid Mechanics and Heat Transfer.* Institute of Fluid Mechanics and Heat Transfer, Graz University of Technology, 2009.

[35] A. Suzuki. *Application of Dynamic Inflow Theory to Wind Turbine Rotors.* PhD thesis, University of Utah, 2000.

[36] E. Truckenbrodt. *Fluidmechanik.* Springer, 1996.

[37] H. Schlichting E. Truckenbrodt. *Aerodynamik des Flugzeugs.* Springer, 2001.

[38] E. Pedersen F. van den Berg R. Bakker J. Bourma. Response to noise from modern wind farms in the netherlands. *Journal of the Acoustical Society of America*, 2009.

[39] E. Pedersen K. Persson Wayne. Perception and annoyance due to wind turbine noise. a dose-response relationship. *Journal of the Acoustical Society of America*, 2004.

A. Governing equations

A.1. Stress tensor

$$\underline{\boldsymbol{\tau}} = \begin{bmatrix} \tau_{xx} & \tau_{yx} & \tau_{zx} \\ \tau_{xy} & \tau_{yy} & \tau_{zy} \\ \tau_{xz} & \tau_{yz} & \tau_{zz} \end{bmatrix} \tag{A.1}$$

$$\tau_{xx} = \mu \left[2\frac{\partial u}{\partial x} - \frac{2}{3}\boldsymbol{\nabla} \cdot \boldsymbol{v} \right] \tag{A.2}$$

$$\tau_{yy} = \mu \left[2\frac{\partial v}{\partial y} - \frac{2}{3}\boldsymbol{\nabla} \cdot \boldsymbol{v} \right] \tag{A.3}$$

$$\tau_{zz} = \mu \left[2\frac{\partial w}{\partial z} - \frac{2}{3}\boldsymbol{\nabla} \cdot \boldsymbol{v} \right] \tag{A.4}$$

$$\tau_{xy} = \tau_{yx} = \mu \left[\frac{\partial u}{\partial y} + \frac{\partial v}{\partial x} \right] \tag{A.5}$$

$$\tau_{yz} = \tau_{zy} = \mu \left[\frac{\partial v}{\partial z} + \frac{\partial w}{\partial y} \right] \tag{A.6}$$

$$\tau_{xz} = \tau_{zx} = \mu \left[\frac{\partial w}{\partial x} + \frac{\partial u}{\partial z} \right] \tag{A.7}$$

A.2. Dissipation function

$$\frac{1}{\mu}\Phi_\mu = 2\left[\left(\frac{\partial u}{\partial x}\right)^2 + \left(\frac{\partial v}{\partial y}\right)^2 + \left(\frac{\partial w}{\partial z}\right)^2 \right] + \tau_{xy}^2 + \tau_{zy}^2 + \tau_{xz}^2 - \frac{2}{3}\left(\boldsymbol{\nabla} \cdot \boldsymbol{v}\right)^2 \tag{A.8}$$

A.3. Derivation of primitive formulation

$$\frac{\partial \rho}{\partial t} + \boldsymbol{\nabla} \cdot (\rho \boldsymbol{v}) = \dot{m} \tag{A.9}$$

$$\frac{\partial \rho \boldsymbol{v}}{\partial t} + \boldsymbol{\nabla} \cdot (\rho \boldsymbol{v}\boldsymbol{v}) = -\boldsymbol{\nabla} p + \boldsymbol{\nabla} \cdot \underline{\boldsymbol{\tau}} + \boldsymbol{f} + \dot{m}\boldsymbol{v} \tag{A.10}$$

$$\frac{\partial \rho e_t}{\partial t} + \boldsymbol{\nabla} \cdot (\rho e_t \boldsymbol{v}) = -\boldsymbol{\nabla} \cdot (p\boldsymbol{v}) - \boldsymbol{\nabla} \cdot \boldsymbol{q} + \boldsymbol{\nabla} \cdot (\underline{\boldsymbol{\tau}} \cdot \boldsymbol{v}) + \dot{\vartheta} + \boldsymbol{f} \cdot \boldsymbol{v} + \dot{m} e_t \tag{A.11}$$

1. Multiply the mass equation A.9 with $\boldsymbol{v}$ and

$$\boldsymbol{v}\frac{\partial \rho}{\partial t} + \boldsymbol{v}\boldsymbol{v} \cdot \boldsymbol{\nabla}\rho + \rho \boldsymbol{v} \boldsymbol{\nabla} \cdot \boldsymbol{v} = \dot{m}\boldsymbol{v}$$

2. subtract it form the momentum equation A.10.

$$\rho\frac{\partial \boldsymbol{v}}{\partial t}+\boldsymbol{v}\frac{\partial \rho}{\partial t}+\underbrace{\rho\boldsymbol{v}\cdot\boldsymbol{\nabla}\boldsymbol{v}+\boldsymbol{v}\boldsymbol{v}\cdot\boldsymbol{\nabla}\rho+\rho\boldsymbol{v}\boldsymbol{\nabla}\cdot\boldsymbol{v}}_{\boldsymbol{\nabla}\cdot(\rho\boldsymbol{v}\boldsymbol{v})}+\boldsymbol{\nabla}p=\boldsymbol{\nabla}\cdot\underline{\boldsymbol{\tau}}+\boldsymbol{f}+\dot{m}\boldsymbol{v}$$

$$\Longrightarrow \rho\frac{\partial \boldsymbol{v}}{\partial t}+\rho\boldsymbol{v}\cdot\boldsymbol{\nabla}\boldsymbol{v}=-\boldsymbol{\nabla}p+\boldsymbol{\nabla}\cdot\underline{\boldsymbol{\tau}}+\boldsymbol{f} \tag{A.12}$$

3. Multiply the mass equation A.9 with e_t

$$\left(e+\frac{1}{2}\left|\boldsymbol{v}\right|^2\right)\frac{\partial \rho}{\partial t}+\left(e+\frac{1}{2}\left|\boldsymbol{v}\right|^2\right)\boldsymbol{\nabla}\cdot(\rho\boldsymbol{v})=\dot{m}\left(e+\frac{1}{2}\left|\boldsymbol{v}\right|^2\right)$$

$$\Longrightarrow e\frac{\partial \rho}{\partial t}+\left(\frac{1}{2}\left|\boldsymbol{v}\right|^2\right)\frac{\partial \rho}{\partial t}+e\boldsymbol{\nabla}\cdot(\rho\boldsymbol{v})+\left(\frac{1}{2}\left|\boldsymbol{v}\right|^2\right)\boldsymbol{\nabla}\cdot(\rho\boldsymbol{v})=\dot{m}e+\dot{m}\left(\frac{1}{2}\left|\boldsymbol{v}\right|^2\right) \tag{A.13}$$

4. Then take the dot product of equation A.12 with $\boldsymbol{v}$

$$\rho\frac{\partial \frac{1}{2}(\boldsymbol{v}\cdot\boldsymbol{v})}{\partial t}+\rho\boldsymbol{v}\cdot\boldsymbol{\nabla}\underbrace{\frac{1}{2}(\boldsymbol{v}\cdot\boldsymbol{v})}_{\left(\frac{1}{2}|\boldsymbol{v}|^2\right)}=-\boldsymbol{v}\cdot\boldsymbol{\nabla}p+\boldsymbol{v}\cdot[\boldsymbol{\nabla}\cdot\underline{\boldsymbol{\tau}}]+\boldsymbol{v}\cdot\boldsymbol{f}$$

$$\Longrightarrow \rho\frac{\partial\left(\frac{1}{2}\left|\boldsymbol{v}\right|^2\right)}{\partial t}+\rho\boldsymbol{v}\cdot\boldsymbol{\nabla}\left(\frac{1}{2}\left|\boldsymbol{v}\right|^2\right)=-\boldsymbol{v}\cdot\boldsymbol{\nabla}p\overbrace{-(\underline{\boldsymbol{\tau}}:\boldsymbol{\nabla}\boldsymbol{v})+\boldsymbol{\nabla}\cdot(\underline{\boldsymbol{\tau}}\cdot\boldsymbol{v})}^{\boldsymbol{v}\cdot[\boldsymbol{\nabla}\cdot\underline{\boldsymbol{\tau}}]}+\boldsymbol{v}\cdot\boldsymbol{f} \tag{A.14}$$

5. Subtract equations A.13 and A.14 from the energy balance A.11.

$$\frac{\partial\rho\left(e+\frac{1}{2}\left|\boldsymbol{v}\right|^2\right)}{\partial t}+\boldsymbol{\nabla}\cdot\left(\rho\left(e+\frac{1}{2}\left|\boldsymbol{v}\right|^2\right)\boldsymbol{v}\right)+\boldsymbol{\nabla}\cdot(p\boldsymbol{v})=-\boldsymbol{\nabla}\cdot\boldsymbol{q}+\boldsymbol{\nabla}\cdot(\underline{\boldsymbol{\tau}}\cdot\boldsymbol{v})+\dot{\vartheta}+\boldsymbol{f}\cdot\boldsymbol{v}+\dot{m}\left(e+\frac{1}{2}\left|\boldsymbol{v}\right|^2\right)$$

$$\rho\frac{\partial e}{\partial t}+e\frac{\partial\rho}{\partial t}+\rho\frac{\partial\left(\frac{1}{2}\left|\boldsymbol{v}\right|^2\right)}{\partial t}+\left(\frac{1}{2}\left|\boldsymbol{v}\right|^2\right)\frac{\partial\rho}{\partial t}+\rho\boldsymbol{v}\cdot\boldsymbol{\nabla}e+e\boldsymbol{\nabla}\cdot(\rho\boldsymbol{v})+\rho\boldsymbol{v}\cdot\boldsymbol{\nabla}\left(\frac{1}{2}\left|\boldsymbol{v}\right|^2\right)+\left(\frac{1}{2}\left|\boldsymbol{v}\right|^2\right)\boldsymbol{\nabla}\cdot(\rho\boldsymbol{v})=$$

$$-p\boldsymbol{\nabla}\cdot\boldsymbol{v}-\boldsymbol{v}\cdot\boldsymbol{\nabla}p-\boldsymbol{\nabla}\cdot\boldsymbol{q}+\boldsymbol{\nabla}\cdot(\underline{\boldsymbol{\tau}}\cdot\boldsymbol{v})+\dot{\vartheta}+\boldsymbol{f}\cdot\boldsymbol{v}+\dot{m}\left(e+\frac{1}{2}\left|\boldsymbol{v}\right|^2\right)$$

$$\Longrightarrow \rho\frac{\partial e}{\partial t}+\rho\boldsymbol{v}\cdot\boldsymbol{\nabla}e=-p\boldsymbol{\nabla}\cdot\boldsymbol{v}-\boldsymbol{\nabla}\cdot\boldsymbol{q}+\underline{\boldsymbol{\tau}}:\boldsymbol{\nabla}\boldsymbol{v}+\dot{\vartheta}$$

This yields a simplified system of equations for the NS-equations where the substantial derivative $\frac{D}{Dt}=\frac{\partial}{\partial t}+\boldsymbol{v}\cdot\boldsymbol{\nabla}$, the rate of change of density, velocity and specific internal energy of an fluid particle in motion along its pathline, is considered.

$$\frac{D\rho}{Dt} = -\rho \boldsymbol{\nabla} \cdot \boldsymbol{v} + \dot{m} \tag{A.15}$$

$$\rho \frac{D\boldsymbol{v}}{Dt} = -\boldsymbol{\nabla} p + \boldsymbol{\nabla} \cdot \underline{\boldsymbol{\tau}} + \boldsymbol{f} \tag{A.16}$$

$$\rho \frac{De}{Dt} = -p \boldsymbol{\nabla} \cdot \boldsymbol{v} + \underline{\boldsymbol{\tau}} : \boldsymbol{\nabla} \boldsymbol{v} - \boldsymbol{\nabla} \cdot q + \dot{\vartheta} \tag{A.17}$$

A.4. Derivation of linearized gas dynamics

$$\frac{\partial \rho}{\partial t} + \boldsymbol{v} \cdot \nabla \rho + \rho \boldsymbol{\nabla} \cdot \boldsymbol{v} = \dot{m}$$

$$\underbrace{\frac{\partial \left(\rho_0 + \epsilon \rho'\right)}{\partial t}}_{①} + \underbrace{\left(\boldsymbol{v}_0 + \epsilon \boldsymbol{v}'\right) \cdot \boldsymbol{\nabla} \left(\rho_0 + \epsilon \rho'\right)}_{②} + \underbrace{\left(\rho_0 + \epsilon \rho'\right) \boldsymbol{\nabla} \cdot \left(\boldsymbol{v}_0 + \epsilon \boldsymbol{v}'\right)}_{③} = \underbrace{\left(\dot{m}_0 + \epsilon \dot{m}'\right)}_{④}$$

$$① : \quad \underbrace{\frac{\partial \rho_0}{\partial t}}_{=0} + \epsilon \frac{\partial \rho'}{\partial t}$$

$$② : \quad \underbrace{\boldsymbol{v}_0 \cdot \boldsymbol{\nabla} \rho_0}_{-\rho_0 \boldsymbol{\nabla} \cdot \boldsymbol{v}_0} + \epsilon \boldsymbol{v}_0 \cdot \boldsymbol{\nabla} \rho' + \epsilon \boldsymbol{v}' \cdot \boldsymbol{\nabla} \rho_0 + \epsilon^2 \boldsymbol{v}' \cdot \boldsymbol{\nabla} \rho'$$

$$③ : \quad \rho_0 \boldsymbol{\nabla} \cdot \boldsymbol{v}_0 + \epsilon \rho' \boldsymbol{\nabla} \cdot \boldsymbol{v}_0 + \epsilon \rho_0 \boldsymbol{\nabla} \cdot \boldsymbol{v}' + \epsilon^2 \rho' \boldsymbol{\nabla} \cdot \boldsymbol{v}'$$

$$④ : \quad \underbrace{\dot{m}_0}_{=0} + \epsilon \dot{m}'$$

Presuming that the mean flow variables satisfy 2.81, 2.82, and 2.83 and with $\dot{m}_0 = \boldsymbol{f}_0 = \dot{\vartheta}_0 = 0$ it follows that

$$\begin{aligned} \boldsymbol{v}_0 \cdot \boldsymbol{\nabla} \rho_0 &= -\rho_0 \boldsymbol{\nabla} \cdot \boldsymbol{v}_0 \\ \rho_0 \boldsymbol{v}_0 \cdot \boldsymbol{\nabla} \boldsymbol{v}_0 &= -\boldsymbol{\nabla} p_0 \\ \frac{1}{c^2} \boldsymbol{v}_0 \cdot \boldsymbol{\nabla} p_0 &= -\rho_0 \boldsymbol{\nabla} \cdot \boldsymbol{v}_0 \end{aligned}$$

With $\lim_{\epsilon \to 0} \left\{ \frac{\partial}{\partial \epsilon} \left[① + ② + ③ + ... \right] \right\}$ one get the *linearized gas dynamics equations*

$$\underbrace{\frac{\partial \rho'}{\partial t} + \boldsymbol{v}_0 \cdot \boldsymbol{\nabla} \rho'}_{\frac{D_0 \rho'}{Dt}} + \rho_0 \boldsymbol{\nabla} \cdot \boldsymbol{v}' + \boldsymbol{v}' \cdot \boldsymbol{\nabla} \rho_0 + \rho' \boldsymbol{\nabla} \cdot \boldsymbol{v}_0 = \dot{m}'$$

$$\frac{D_0\rho'}{Dt} + \rho_0 \boldsymbol{\nabla}\cdot\boldsymbol{v}' + \boldsymbol{v}'\cdot\boldsymbol{\nabla}\rho_0 + \rho'\boldsymbol{\nabla}\cdot\boldsymbol{v}_0 = \dot{m}' \tag{A.18}$$

$$\rho_0\frac{D_0\boldsymbol{v}'}{Dt} + \boldsymbol{\nabla}p' + \rho_0\boldsymbol{v}'\cdot\boldsymbol{\nabla}\boldsymbol{v}_0 + \rho'\boldsymbol{v}_0\cdot\boldsymbol{\nabla}\boldsymbol{v}_0 = \boldsymbol{f}' \tag{A.19}$$

$$\underbrace{\frac{1}{(c^2)_0}}_{\left[\frac{\kappa p_0}{\rho_0}\right]_{pg}}\left(\frac{D_0p'}{Dt} + \left[\boldsymbol{v}' - \boldsymbol{v}_0\,\underbrace{(c^2)'/(c^2)_0}_{\left[\frac{p'}{p_0}+\frac{\rho'}{\rho_0}\right]_{pg}}\right]\cdot\boldsymbol{\nabla}p_0\right) + \rho_0\boldsymbol{\nabla}\cdot\boldsymbol{v}' + \rho'\boldsymbol{\nabla}\cdot\boldsymbol{v}_0 = \underbrace{\frac{\sigma_0}{T_0}\dot{\vartheta}' + \left(1 - \frac{\sigma_0}{T_0}\frac{p_0}{\rho_0}\right)\dot{m}'}_{\left[\frac{\kappa-1}{(c^2)_0}\dot{\vartheta}'+\frac{1}{\kappa}\dot{m}'\right]_{pg}=:\dot{\Theta}'} \tag{A.20}$$

B. Acoustic

B.1. Green's functions

A common way to solve the acoustic wave equation with respect to the acoustic pressure is to use *Green's functions*. Following *Green's theorem* an acoustic field is determined when the *G-function* to a problem is known.

$$p'(x,t) = \int_{V_\infty} \int_{-\infty}^{t} G\langle \boldsymbol{x}, t|\boldsymbol{y}, \tau\rangle \, Q_p(\boldsymbol{y}, \tau) \, d\tau dV_{\boldsymbol{y}} \tag{B.1}$$

The most simple example of such an G-function is derived for a situation where the surrounding fluid is at rest with constant mean density and no obstacles between sources and listener. This function is the so called *free field Green's function*.

$$G\langle \boldsymbol{x}, t|\boldsymbol{y}, \tau\rangle = \frac{\delta\left(t - \tau - \frac{|\boldsymbol{x}-\boldsymbol{y}|}{c_0}\right)}{4\pi \, |\boldsymbol{x} - \boldsymbol{y}|} \tag{B.2}$$

Inserting B.2 into B.1 gives 2.91.

In principle a Green's function is a pulse response to a certain scenario concerning the fluid and/or geometrical properties. For instance, when "firing" a needle pulse into an empty room the recorded response of a microphone will be different than when doing the same for a fully furnished room. Frankly, in acoustics there only exist a few Green's functions for conditions of very limited complexity. Therefore Green's function that characterizes free field conditions at zero mean flow are used for a wide variety of technical problems.

B.2. One-third octave A-weighting specifications

Table B.1.: One-third octave band center frequencies and A-weighting values

f_l	f_c	f_u	A-weighting	f_l	f_c	f_u	A-weighting
$[Hz]$	$[Hz]$	$[Hz]$	$[dB]$	$[Hz]$	$[Hz]$	$[Hz]$	$[dB]$
14.1	**16**	17.8	-56.2	562	**630**	708	-1.9
17.8	**20**	22.4	-50.5	708	**800**	891	-0.8
22.4	**25**	28.2	-44.7	891	**1000**	1122	0
28.2	**31.5**	35.5	-39.4	1122	**1250**	1413	+0.6
35.5	**40**	44.7	-34.6	1413	**1600**	1778	+1.0
44.7	**50**	56.2	-30.2	1778	**2000**	2239	+1.2
56.2	**63**	70.8	-26.2	2239	**2500**	2818	+1.3
70.8	**80**	89.1	-22.5	2818	**3150**	3548	+1.2
89.1	**100**	112	-19.1	3548	**4000**	4467	+1.0
112	**125**	141	-16.1	4467	**5000**	5623	+0.5
141	**160**	178	-13.4	5623	**6300**	7079	-0.1
178	**200**	224	-10.9	7079	**8000**	8913	-1.1
224	**250**	282	-8.6	8913	**10000**	11220	-2.5
282	**315**	355	-6.6	11220	**12500**	14130	-4.3
355	**400**	447	-4.8	14130	**16000**	17780	-6.6
447	**500**	562	-3.2	17780	**20000**	22390	-9.3

B.3. Common sound pressure levels

Table B.2.: Mapping between sound pressure and sound pressure level [25]

Sound pressure [Pa]	Sound pressure level [dB]	Equivalent
$2 \cdot 10^{-5}$	0	Threshold of hearing
$2 \cdot 10^{-4}$	20	Forest with modest wind
$2 \cdot 10^{-3}$	40	Library
$2 \cdot 10^{-2}$	60	Office
$2 \cdot 10^{-1}$	80	Highly frequented street
$2 \cdot 10^{0}$	100	Jackhammer, sirens
$2 \cdot 10^{1}$	120	Start of jet plane
$2 \cdot 10^{2}$	140	Threshold of pain

C. Further results

C.1. AOC 15/50

C.1.1. Non-weighted

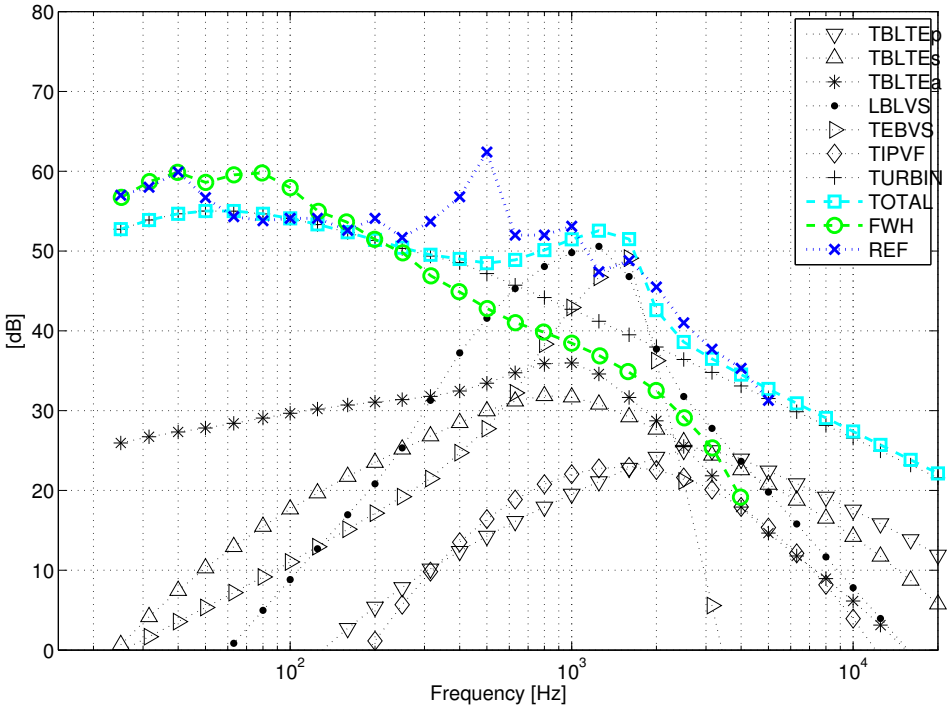

Figure C.1.: Observer position 1(1). Wind 8m/s at 10m height, $\Lambda = 24.5m$, $I = 11.53\%$.

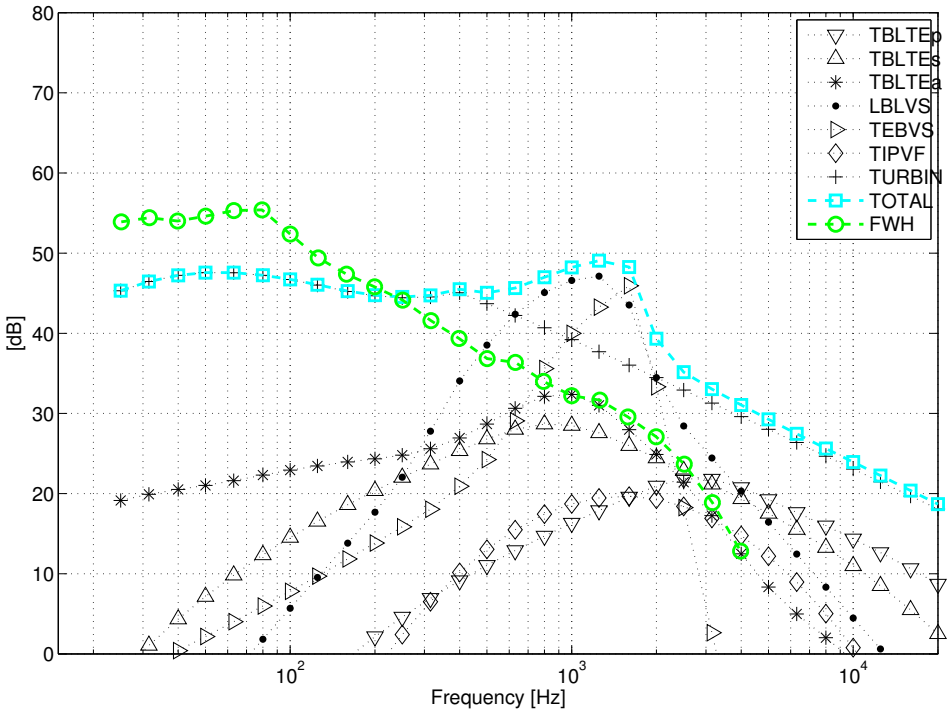

Figure C.2.: Observer position 2(5). Wind 8m/s at 10m height, $\Lambda = 24.5m$, $I = 11.53\%$.

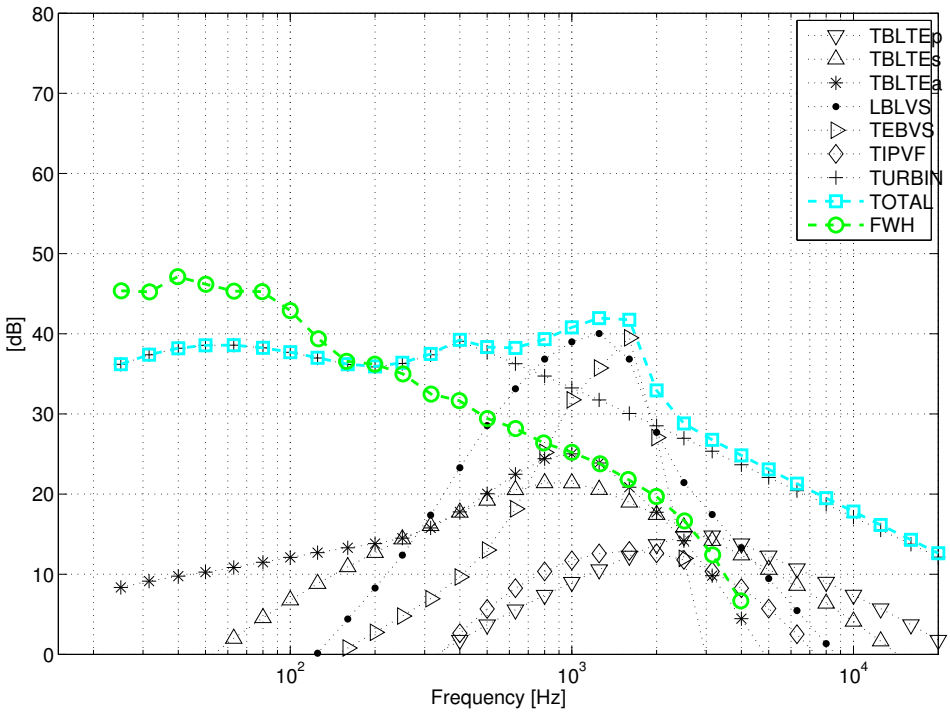

Figure C.3.: Observer position RP(7). Wind 8m/s at 10m height, $\Lambda = 24.5m$, $I = 11.53\%$.

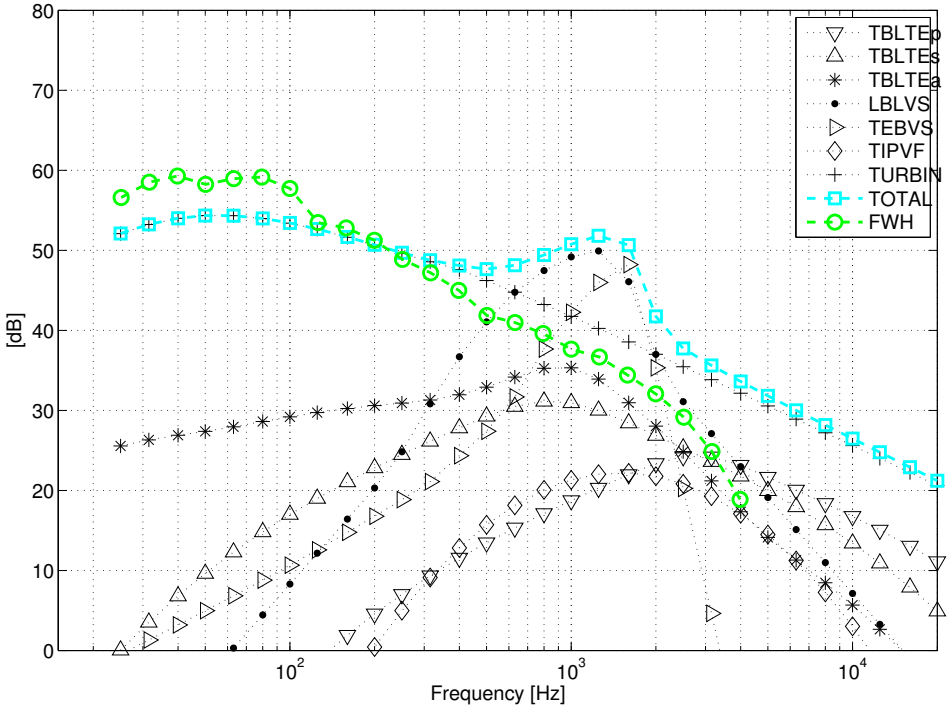

Figure C.4.: Observer position 3(13). Wind 8m/s at 10m height, $\Lambda = 24.5m$, $I = 11.53\%$.

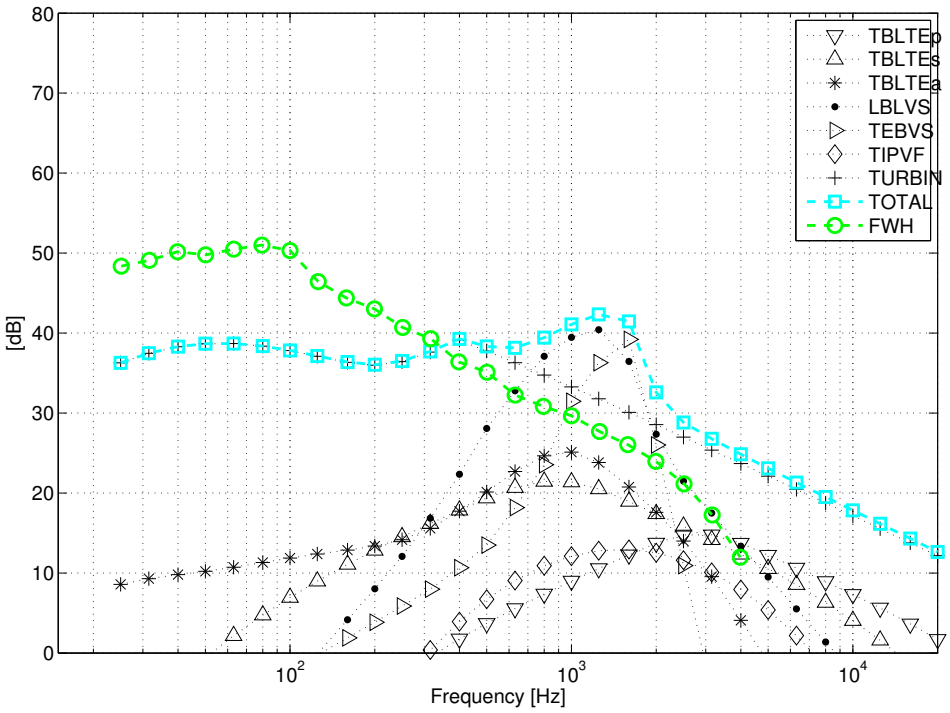

Figure C.5.: Observer position RP(19). Wind 8m/s at 10m height, $\Lambda = 24.5m$, $I = 11.53\%$.

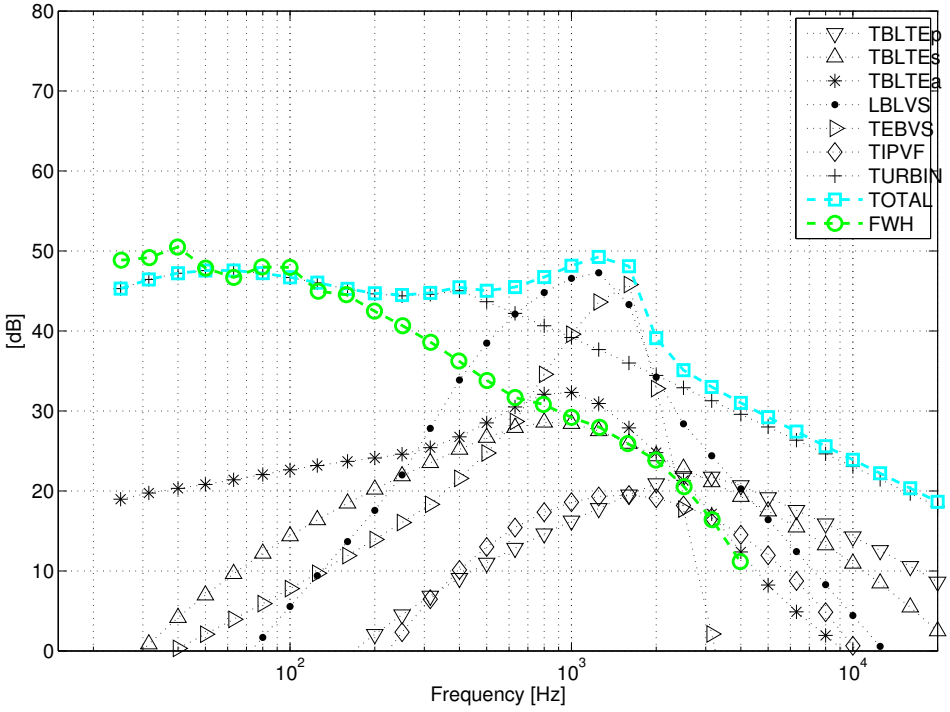

Figure C.6.: Observer position 4(21). Wind 8m/s at 10m height, $\Lambda = 24.5m$, $I = 11.53\%$.

C.1.2. A-weighted

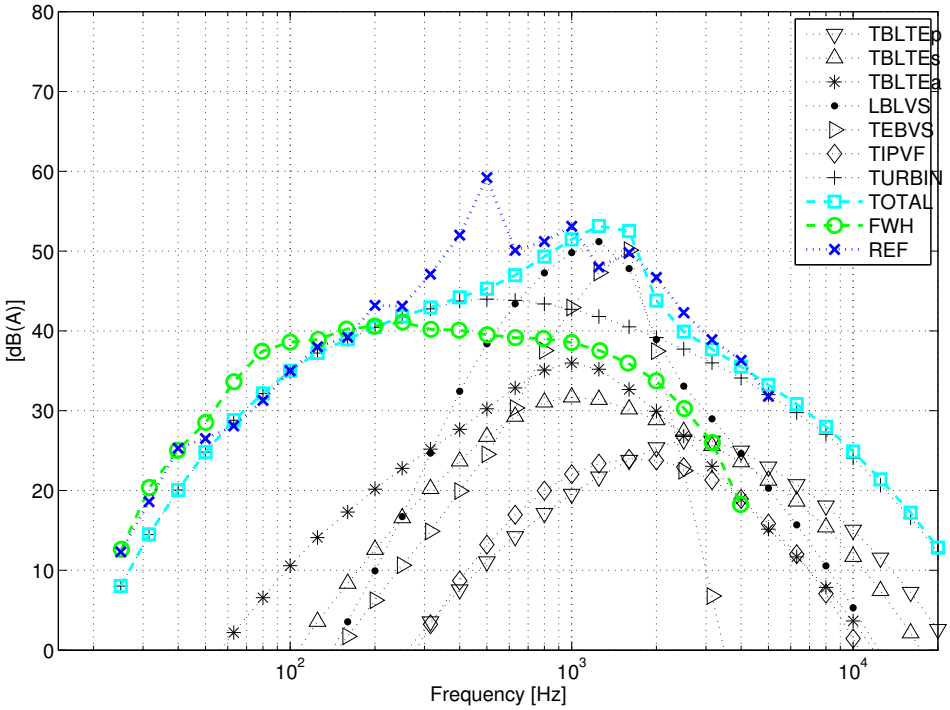

Figure C.7.: Observer position 1(1). Wind 8m/s at 10m height, $\Lambda = 24.5m$, $I = 11.53\%$.

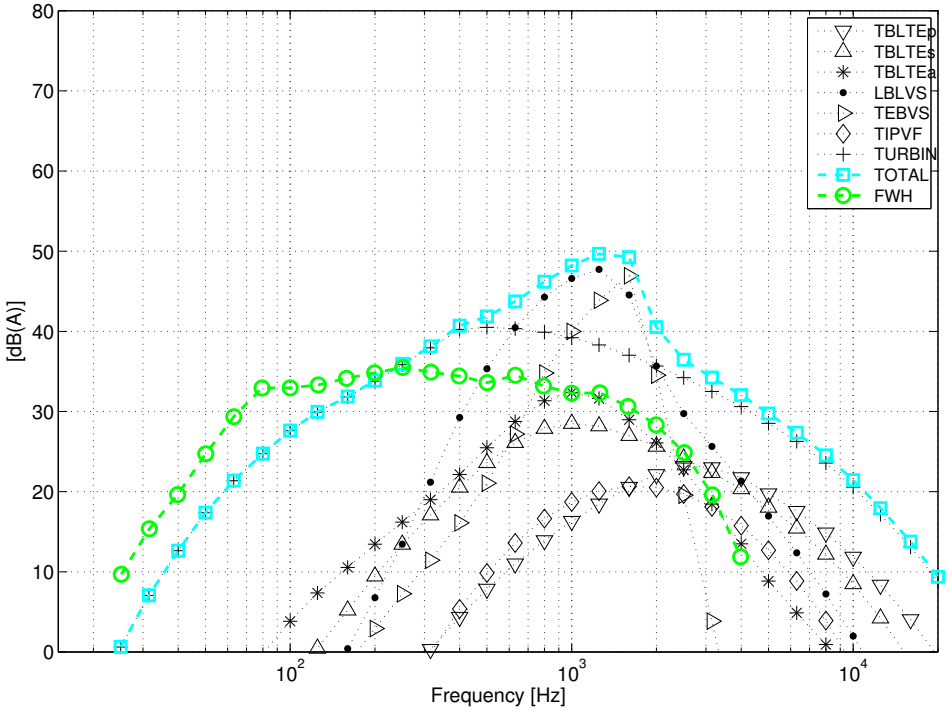

Figure C.8.: Observer position 2(5). Wind 8m/s at 10m height, $\Lambda = 24.5m$, $I = 11.53\%$.

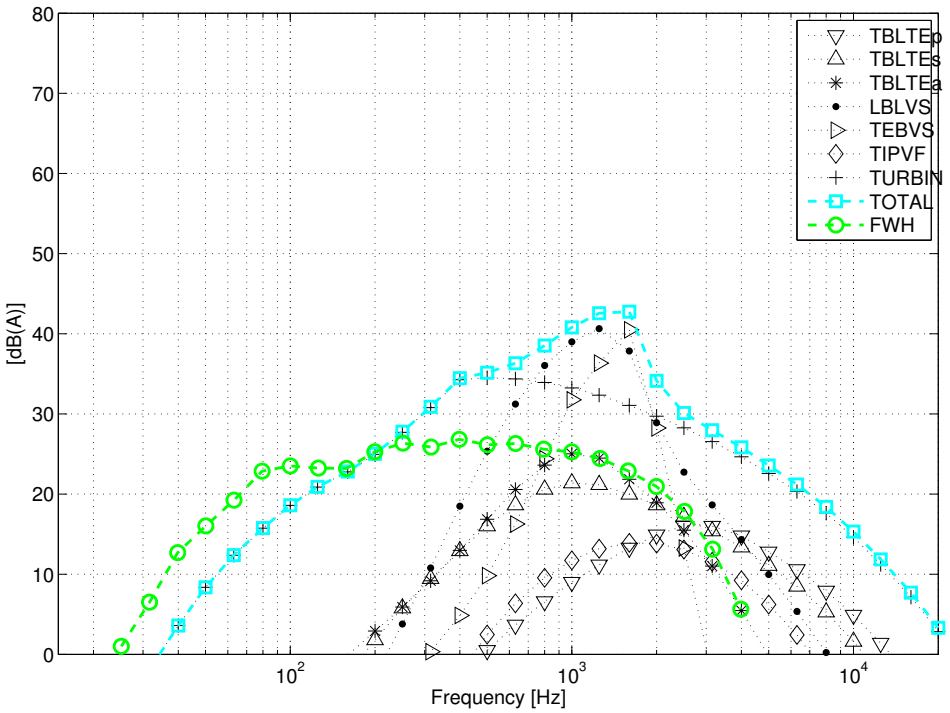

Figure C.9.: Observer position RP(7). Wind 8m/s at 10m height, $\Lambda = 24.5m$, $I = 11.53\%$.

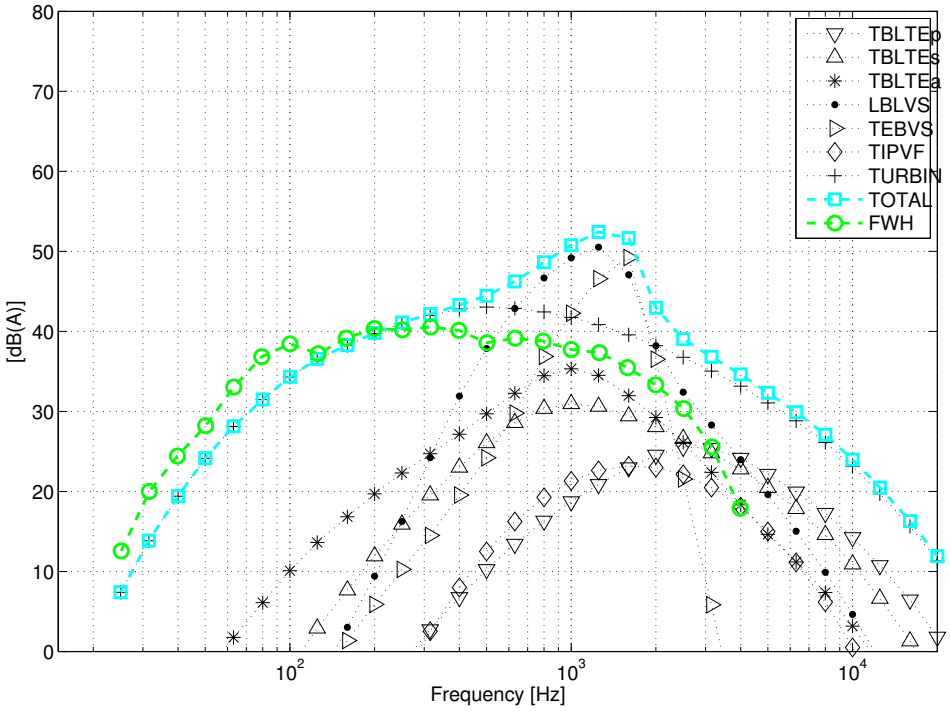

Figure C.10.: Observer position 3(13). Wind 8m/s at 10m height, $\Lambda = 24.5m$, $I = 11.53\%$.

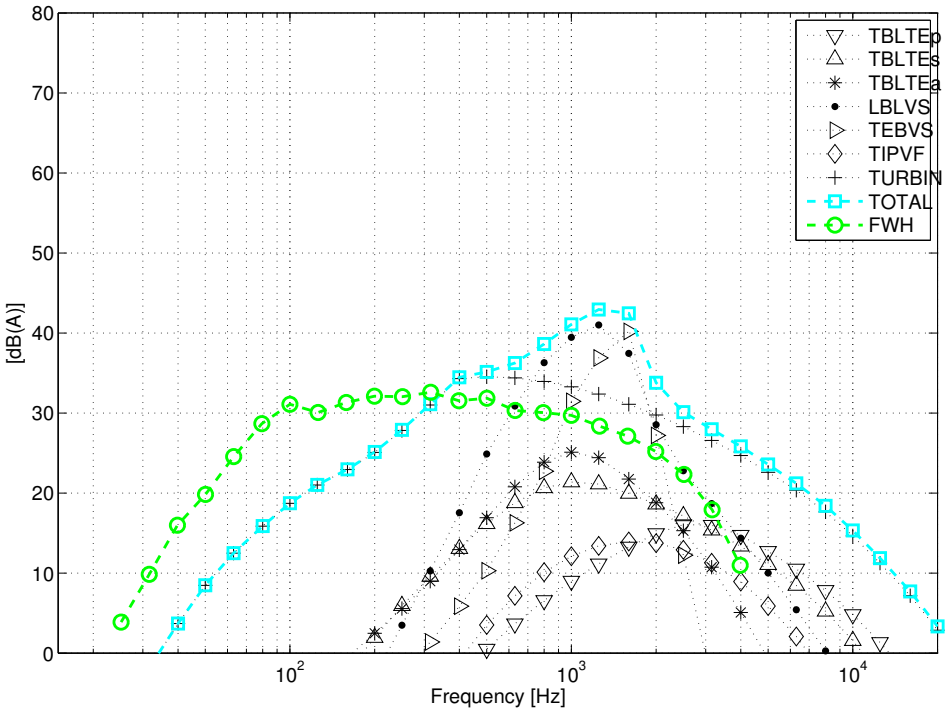

Figure C.11.: Observer position RP(19). Wind 8m/s at 10m height, $\Lambda = 24.5m$, $I = 11.53\%$.

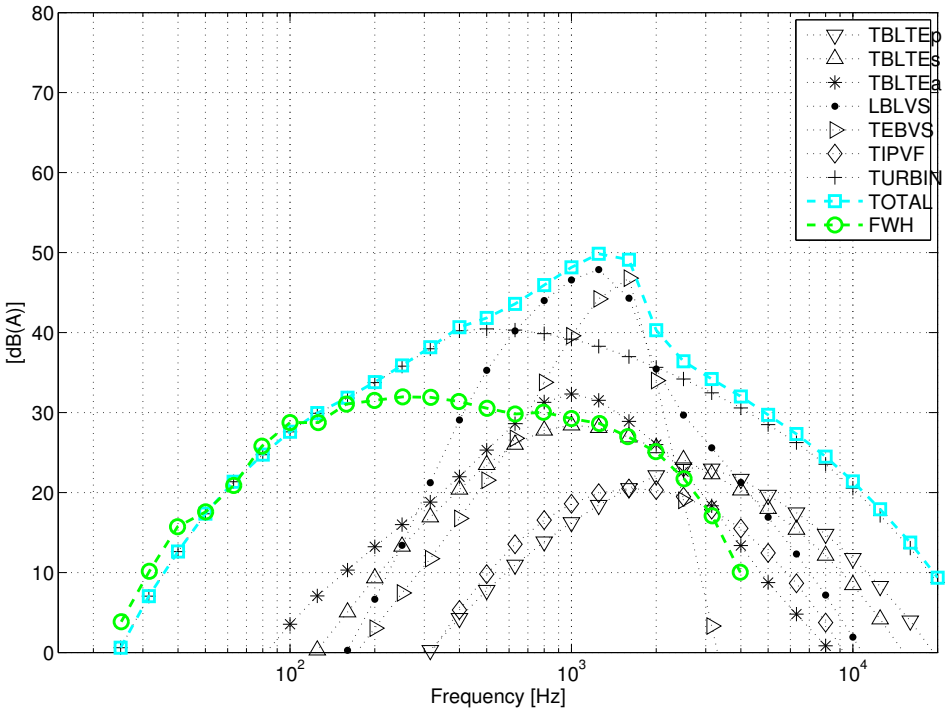

Figure C.12.: Observer position 4(21). Wind 8m/s at 10m height, $\Lambda = 24.5m$, $I = 11.53\%$.

C.2. NREL5M

C.2.1. Non-weighted

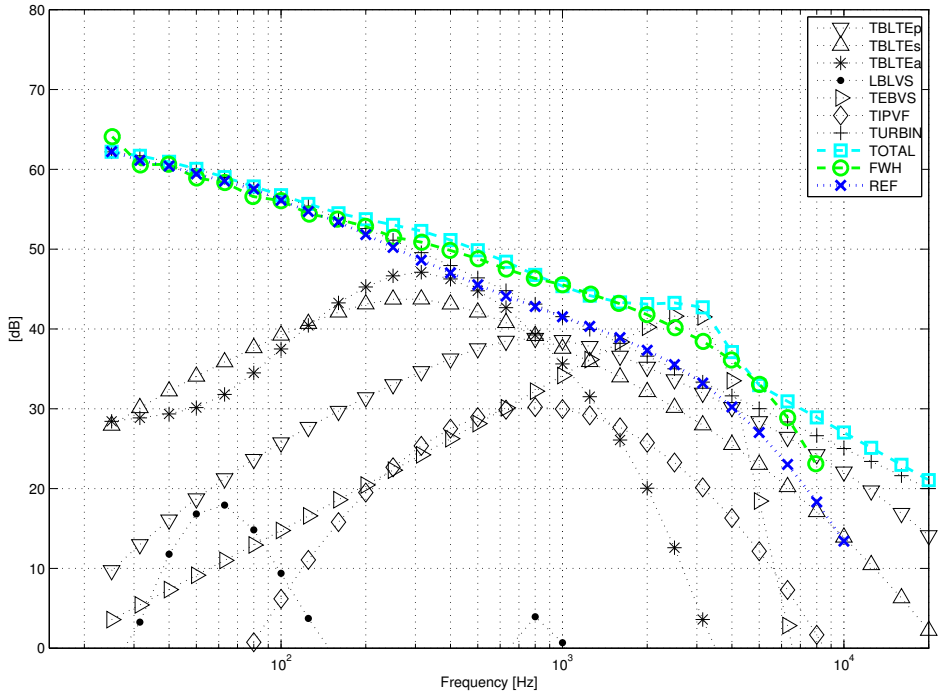

Figure C.13.: Observer position 1(1). Wind 8m/s at 10m height, $\Lambda = 29.4m$, $I = 8.75\%$.

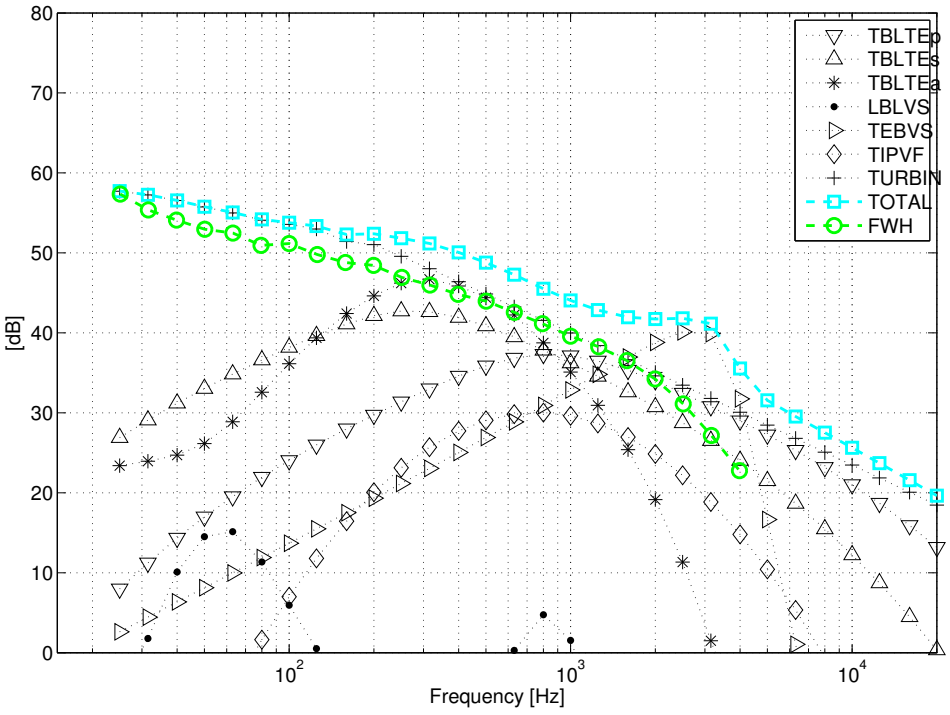

Figure C.14.: Observer position 2(5). Wind 8m/s at 10m height, $\Lambda = 29.4m$, $I = 8.75\%$.

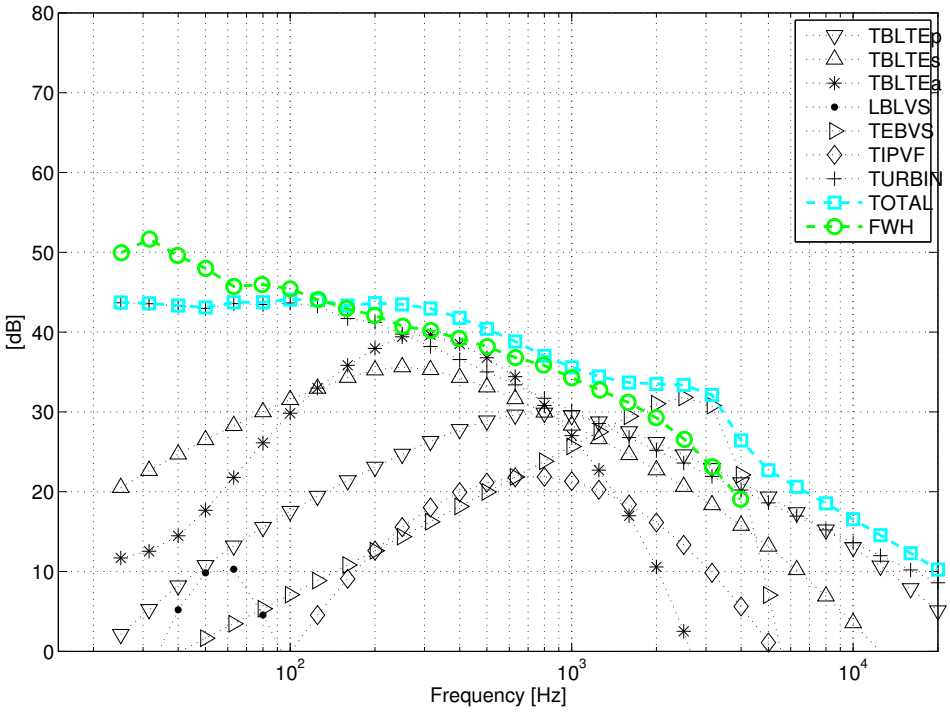

Figure C.15.: Observer position RP(7). Wind 8m/s at 10m height, $\Lambda = 29.4m$, $I = 8.75\%$.

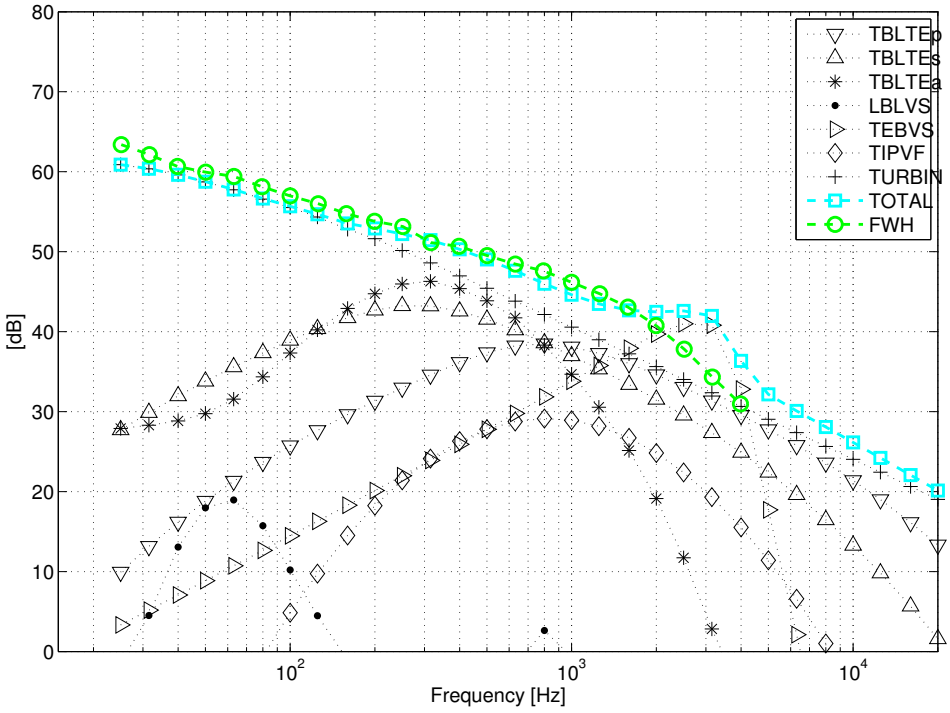

Figure C.16.: Observer position 3(13). Wind 8m/s at 10m height, $\Lambda = 29.4m$, $I = 8.75\%$.

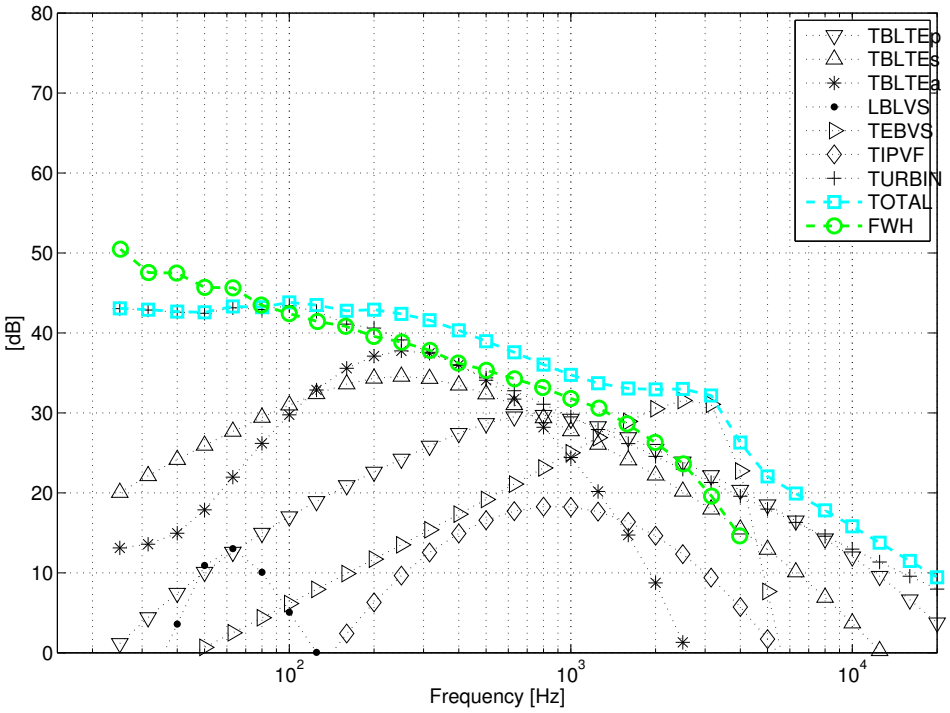

Figure C.17.: Observer position RP(19). Wind 8m/s at 10m height, $\Lambda = 29.4m$, $I = 8.75\%$.

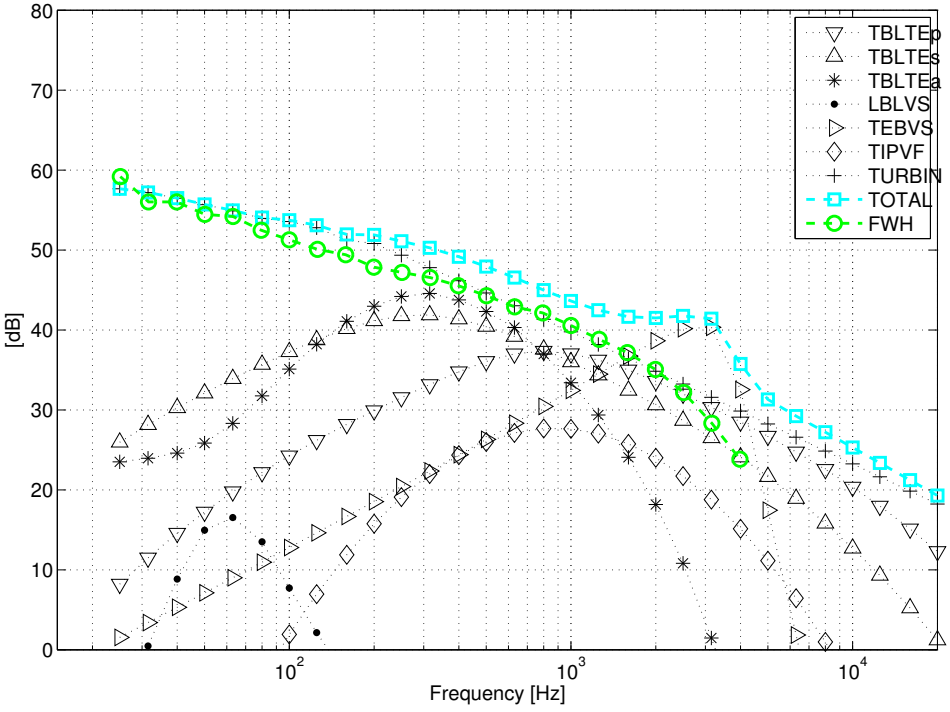

Figure C.18.: Observer position 4(21). Wind 8m/s at 10m height, $\Lambda = 29.4m$, $I = 8.75\%$.

C.2.2. A-weighted

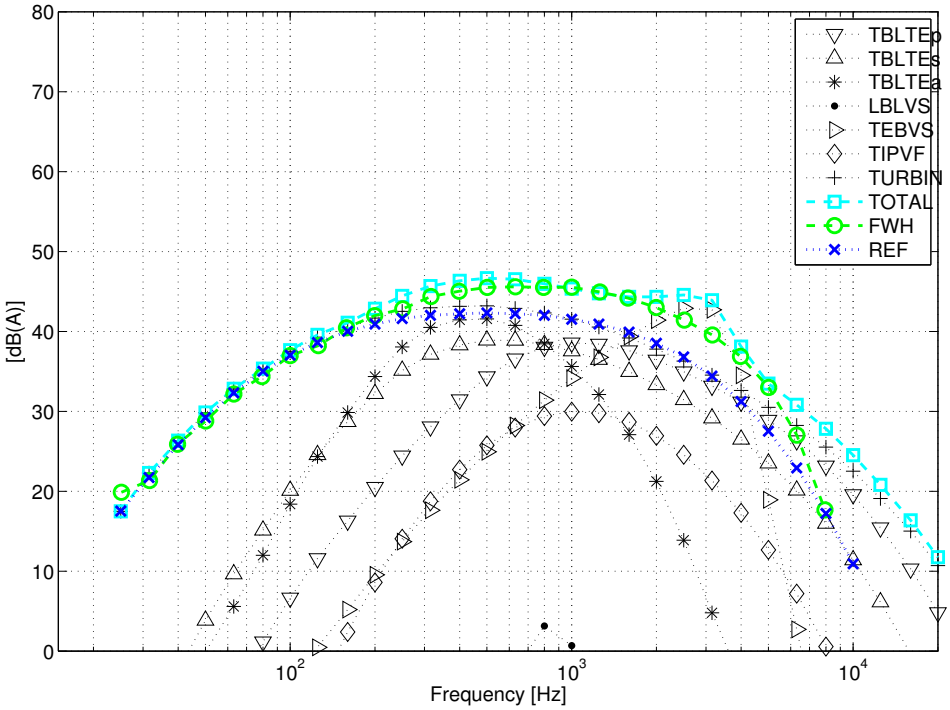

Figure C.19.: Observer position 1(1). Wind 8m/s at 10m height, $\Lambda = 29.4m$, $I = 8.75\%$.

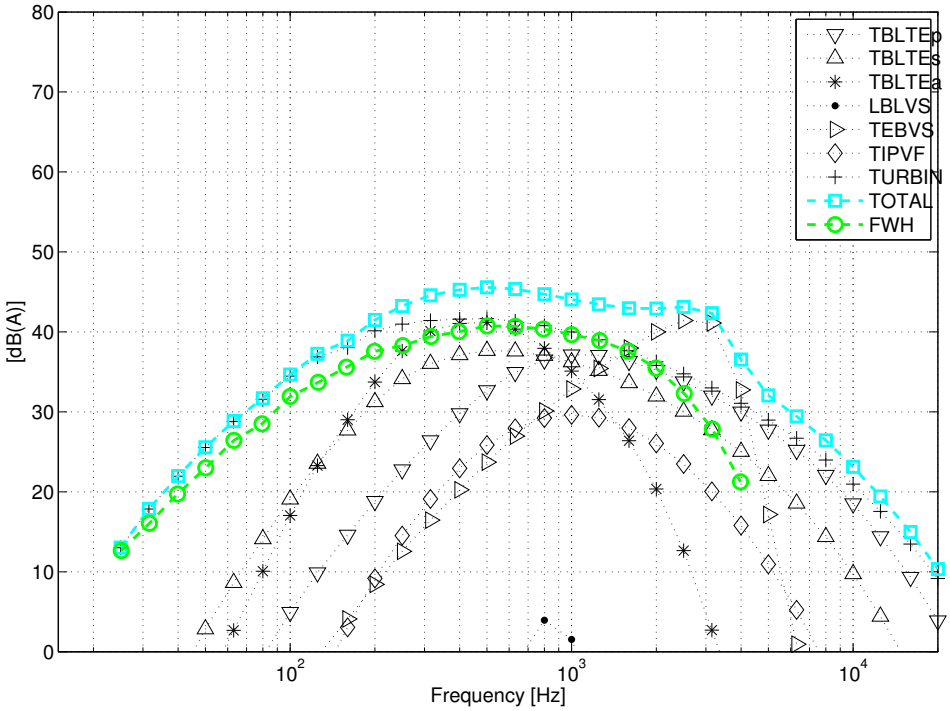

Figure C.20.: Observer position 2(5). Wind 8m/s at 10m height, $\Lambda = 29.4m$, $I = 8.75\%$.

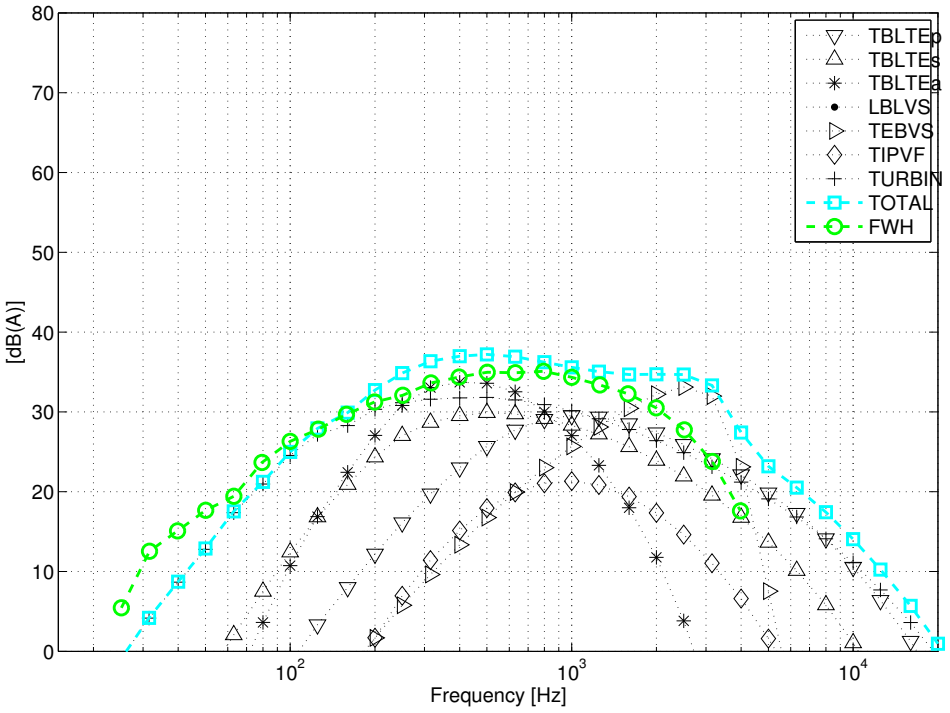

Figure C.21.: Observer position RP(7). Wind 8m/s at 10m height, $\Lambda = 29.4m$, $I = 8.75\%$.

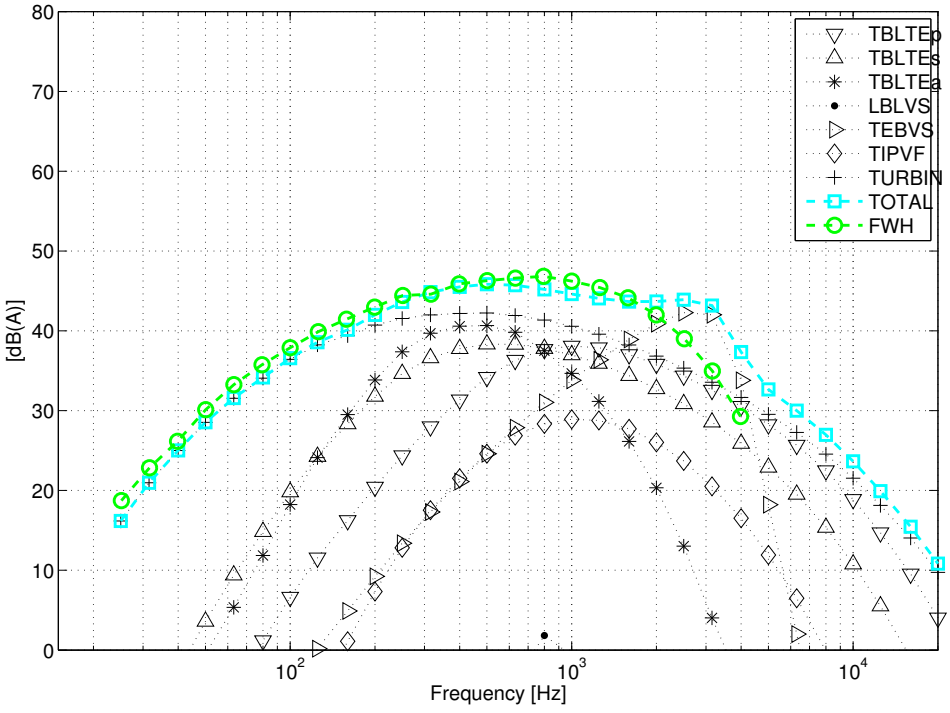

Figure C.22.: Observer position 3(13). Wind 8m/s at 10m height, $\Lambda = 29.4m$, $I = 8.75\%$.

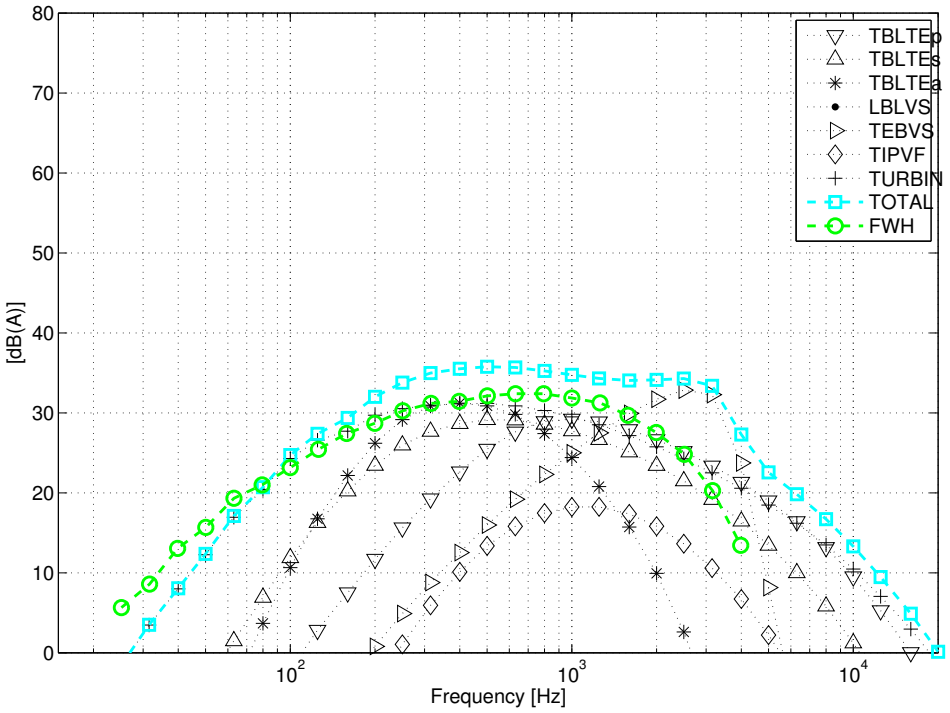

Figure C.23.: Observer position RP(19). Wind 8m/s at 10m height, $\Lambda = 29.4m$, $I = 8.75\%$.

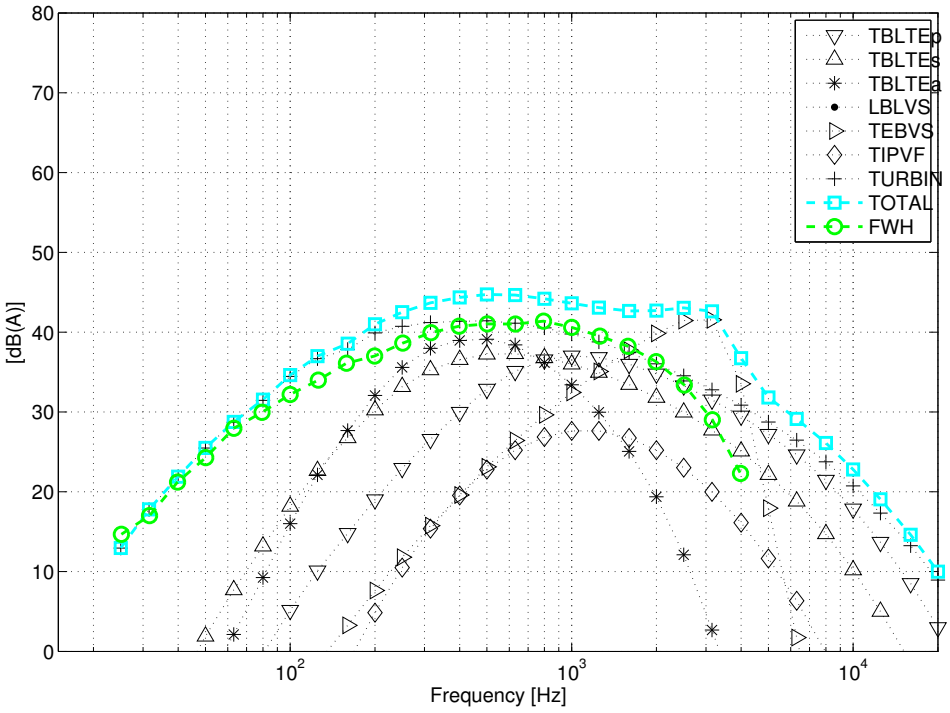

Figure C.24.: Observer position 4(21). Wind 8m/s at 10m height, $\Lambda = 29.4m$, $I = 8.75\%$.

List of Figures

List of Tables